TECHNISCHE UNIVERSITÄT MÜNCHEN

Fakultät für Medizin
Institut für diagnostische und interventionelle Radiologie

Morphological Magnetic Resonance Imaging and Diffusion Tensor Imaging of Peripheral Nerves

Barbara Cervantes Robles Martinez

Vollständiger Abdruck der von der Fakultät für Medizin der Technischen Universität München zur Erlangung des akademischen Grades eines

Doktor der Naturwissenschaften (Dr. rer. nat.)

genehmigten Dissertation.

Vorsitzender: Prof. Dr. Claus Zimmer
Prüfer der Dissertation:
1. Priv.-Doz. Dimitrios Karampinos, Ph.D.
2. Univ.-Prof. Dr. Axel Haase

Die Dissertation wurde am 02.03.2018 bei der Technische Universität München eingereicht und durch die Fakultät für Medizin am 04.07.2018 angenommen.

Abstract

The human nervous system in the body is formed by multiple nerves that originate from the spinal cord and that distally subdivide into fine nerve branches. Nerves in the body serve vital functions including breathing, heart rate, temperature regulation and movement of body parts. Neural pathology can impair essential physiological functionalities thus requiring diagnosis and treatment. Due to its superb soft-tissue contrast and the ability to reach sub-millimeter resolutions, magnetic resonance imaging (MRI) is a valuable tool for the noninvasive examination of nerves outside the spinal cord. Thanks to the advances in high-resolution MRI, this imaging modality is used in the diagnosis and treatment of peripheral neuropathy, muscle denervation, neurofibromatosis and nerve entrapment, among other applications, as well as to provide guidance for perineural injections. MRI of nerves outside the spinal cord requires high image quality as well as high resolutions in order to resolve these fine structures, while isotropic resolutions can be needed to visualize nerves with intricate geometries. Therefore, given the small sizes and complex geometries of nerves outside the spinal cord, as well as the presence of magnetic-field inhomogeneities in body imaging, MRI of this anatomy requires methods capable of achieving good signal quality at high resolutions while being robust to distortion artifacts.

Morphological MRI can be used to detect changes in nerve structure but is limited to the available contrast and can be insufficient in precisely identifying nerve injury, leading to the necessity of quantitative methods for a more accurate diagnosis of neuropathy. Diffusion tensor imaging (DTI), a quantitative MRI technique, has the ability to assess the microstructural functionality of nerves and thus serves as a powerful tool to probe structural information that morphological methods are incapable of detecting. DTI can therefore help identify neural anomalies more accurately than morphological methods. In body imaging, however, DTI methods are largely challenged by motion and magnetic-field inhomogeneities and require careful considerations in their design.

The present cumulative doctoral thesis assembles three journal publications with focus on the development of state-of-the-art morphological MRI and DTI techniques dedicated to solve the above-mentioned challenges using a 3D turbo spin echo (TSE) pulse sequence. The work in the presented publications addresses (i) refocusing angle design in 3D TSE imaging particular to the visualization of small nerves; (ii) vessel signal suppression in motion-sensitized diffusion-equilibrium 3D TSE imaging of nerves in the extremities; and (iii) isotropic-resolution 3D TSE diffusion tensor nerve imaging.

The work on refocusing angle design investigates the effects of blurring at the tissue interface produced by the 3D TSE sequence using tissue-specific refocusing angle modulation considering local geometric properties. A refocusing angle strategy is presented that generates the highest possible signal for the minimum achievable blurring of small embedded nerves. Signal response is evaluated quantitatively and qualitatively and is verified by in vivo measurements of small nerve branches. The proposed tissue- and geometry-specific refocusing scheme is shown to provide superior image quality compared to conventional tissue-specific approach. High-isotropic-resolution 3D in vivo imaging of small nerves is presented using the developed method in which fine nerve branches and their

substructures are well visualized and highly defined.

The work addressing vessel signal suppression in imaging of nerves in the extremities studies the distinct mechanisms available for suppressing the signal of slowly flowing blood in small vessels taking into account the direction of flow. A methodology is presented that combines motion and diffusion sensitization in specific directions for the maximum suppression of vessel signal with the minimum attenuation of nerve signal. The developed method is shown in vivo to provide superior vessel signal suppression in comparison to conventional motion- and diffusion-sensitized methods. High-isotropic-resolution 3D in vivo imaging with the developed technique is presented that clearly delineates nerves in the lower extremities with minimum vessel-signal contamination in multiple spatial reformats.

The work on DTI proposes TSE-based imaging for avoiding geometric distortions in isotropic-resolution 3D diffusion imaging. The work presents a modified 3D TSE sequence suitable for diffusion imaging in conjunction with a diffusion preparation developed for the 3D TSE sequence and designed particularly for robust body imaging. Phase navigation is incorporated into the 3D TSE sequence and a phase correction strategy is presented in the image reconstruction in order to address motion-induced intershot phase errors. A quantitative examination of motion-induced phase errors in diffusion-prepared 3D TSE is presented and distortion-free isotropic-resolution 3D TSE DTI of nerves is shown in vivo using the proposed method.

List of Included Journal Publications

The present doctoral thesis is based on the following three first-authored journal publications:

JP-I **Cervantes, Barbara**, J. S. Bauer, F. Zibold, H. Kooijman, M. Settles, A. Haase, E. J. Rummeny, K. Wörtler, and D. C. Karampinos, "Imaging of the lumbar plexus: Optimized refocusing flip angle train design for 3d tse", *Journal of Magnetic Resonance Imaging*, vol. 43, no. 4, pp. 789–799, 2016.

JP-II **Cervantes, Barbara**, J. S. Kirschke, E. Klupp, H. Kooijman, P. Börnert, A. Haase, E. J. Rummeny, and D. C. Karampinos, "Orthogonally combined motion-and diffusion-sensitized driven equilibrium (oc-mdsde) preparation for vessel signal suppression in 3d turbo spin echo imaging of peripheral nerves in the extremities", *Magnetic resonance in medicine*, vol. 79, no. 1, pp. 407–415, 2018.

JP-III **Cervantes, Barbara**, A. T. Van, D. Weidlich, H. Kooijman, A. Hock, E. J. Rummeny, A. Gersing, J. S. Kirschke, and D. C. Karampinos, "Isotropic resolution diffusion tensor imaging of lumbosacral and sciatic nerves using a phase-corrected diffusion-prepared 3d turbo spin echo", *Magnetic Resonance in Medicine*, n/a–n/a, ISSN: 1522-2594. DOI: 10.1002/mrm.27072. [Online]. Available: http://dx.doi.org/10.1002/mrm.27072.

The above publications can be found in Chapter 5.

List of Related Publications

Co-Authored Journal Publications

JP-1 N. Sollmann, D. Weidlich, **Cervantes, Barbara**, E. Klupp, C. Ganter, H. Kooijman, E. J. Rummeny, C. Zimmer, J. S. Kirschke, and D. C. Karampinos, "High isotropic resolution t2 mapping of the lumbosacral plexus with t2-prepared 3d turbo spin echo", *Clinical neuroradiology*, pp. 1–8, 2018.

JP-2 E. Klupp, D. Weidlich, S. Schlaeger, T. Baum, **Barbara Cervantes**, M. Deschauer, H. Kooijman, E. J. Rummeny, C. Zimmer, J. S. Kirschke, and D. C. Karampinos, "B1-insensitive t2 mapping of healthy thigh muscles using a t2-prepared 3d tse sequence", *PLOS ONE*, vol. 12, no. 2, e0171337, 2017. DOI: 10.1371/journal.pone.0171337.

JP-3 A. T. Van, **Cervantes, Barbara**, H. Kooijman, and D. C. Karampinos, "Analysis of phase error effects in multishot diffusion-prepared turbo spin echo imaging", *Quantitative imaging in medicine and surgery*, vol. 7, no. 2, p. 238, 2017. DOI: 10.21037/qims.2017.04.01.

JP-4 T. Lichtenstein, A. Sprenger, K. Weiss, K. Slebocki, **Cervantes, Barbara**, D. Karampinos, D. Maintz, G. R. Fink, T. D. Henning, and H. C. Lehmann, "Mri biomarkers of proximal nerve injury in cidp", *Annals of clinical and translational neurology*, vol. 5, no. 1, pp. 19–28, 2018.

First-Authored Conference Publications

CP-1 **B. Cervantes**, A. Gersing, B. Schwaiger, A. Hock, J. M. Peeters, C. Knebel, K. Wörtler, and D. Karampinos, "Robustness of diffusion-prepared 3d tse for isotropic-resolution large-fov coronal dwi of neurogenic tumors in cervical and pelvic regions", in *Proceedings of 26th Scientific Meeting of ISMRM*, 2018, p. 27 218.

CP-2 **B. Cervantes**, A. Van, D. Weidlich, H. Kooijman, A. Hock, E. Rummeny, A. Gersing, J. Kirschke, and D. Karampinos, "Isotropic resolution dti of lower back nerves using a phase-corrected diffusion-prepared 3d tse", in *Proceedings of 26th Scientific Meeting of ISMRM*, 2018, p. 1639.

CP-3 **B. Cervantes**, A. T. Van, H. Kooijman, K. van de Ven, A. Hock, E. J. Rummeny, J. S. Kirschke, and D. C. Karampinos, "One-dimensional phase navigation of diffusion-weighted 3d tse for high resolution musculoskeletal diffusion imaging", in *Proceedings of 25th Scientific Meeting of ISMRM*, 2017, p. 1108.

CP-4 **B. Cervantes**, A. L. Pokorney, J. S. Kirschke, P. Cornejo, J. H. Miller, D. C. Karampinos, and H. H. Hu, "Imaging of the brachial plexus using a 3d dixon-tse pulse sequence with blood vessel and csf signal suppression: Preliminary experience in children", in *Proceedings of 25th Scientific Meeting of ISMRM*, **ISMRM Summa Cum Laude Merit Award**, 2017, p. 3935.

CP-5 **B. Cervantes**, Q. Zhang, K. van de Ven, H. Kooijman, E. J. Rummeny, A. Haase, G. J. Strijkers, J. S. Kirschke, A. J. Nederveen, and D. C. Karampinos, "High-resolution dti of distal peripheral nerves using flow-compensated diffusion-prepared 3d tse", in *Proceedings of 24th Scientific Meeting of ISMRM*, 2016, p. 4530.

CP-6 **B. Cervantes**, D. Weidlich, H. Kooijman, E. J. Rummeny, A. Haase, J. S. Kirschke, and D. C. Karampinos, "High-resolution dwi of the lumbar plexus using b1-insensitive velocity-compensated diffusion-prepared 3d tse", in *Proceedings of 24th Scientific Meeting of ISMRM*, 2016, p. 4474.

CP-7 **B. Cervantes**, H. H. Hu, A. Pokorney, D. Weidlich, H. Kooijman, E. J. Rummeny, A. Haase, J. S. Kirschke, and D. C. Karampinos, "Csf-free imaging of the lumbar plexus using sub-millimeter resolutions with 3d tse", in *Proceedings of 24th Scientific Meeting of ISMRM*, **ISMRM Magna Cum Laude Award**, 2016, p. 2250.

CP-8 **B. Cervantes**, J. Wang, J. S. Bauer, H. Kooijman, P. Brnert, A. Haase, E. J. Rummeny, K. Wörtler, and D. C. Karampinos, "Orthogonally combined motion- and diffusion-sensitized driven equilibrium (oc-mdsde) preparation for improved vessel signal suppression in 3d tse imaging of peripheral nerves", in *Proceedings of 23rd Scientific Meeting of ISMRM*, **ISMRM Magna Cum Laude Award**, 2015, p. 101.

CP-9 **B. Cervantes**, J. S. Bauer, H. Kooijman, M. Settles, A. Haase, E. J. Rummeny, K. Wörtler, and D. C. Karampinos, "Optimized refocusing-flip-angle-train design for small peripheral nerve imaging with 3d tse", in *Proceedings of 23rd Scientific Meeting of ISMRM*, 2015, p. 4230.

Co-Authored Conference Publications

CP-10 E. Klupp, **B. Cervantes**, N. Sollmann, F. Treibel, D. Weidlich, T. Baum, E. J. Rummeny, C. Zimmer, J. S. Kirschke, and D. C. Karampinos, "Improved brachial plexus visualization using an adiabatic imsde-prepared stir 3d tse", in *Proceedings of 26th Scientific Meeting of ISMRM*, France, Paris, 2018, p. 4704.

CP-11 E. Klupp, **B. Cervantes**, S. Schlaeger, S. Inhuber, F. Kreuzpointer, M. Dieckmeyer, F. Freitag, E. J. Rummeny, C. Zimmer, J. S. Kirschke, D. C. Karampinos, and T. Baum, "Relationship of paraspinal muscle dti metrics to isometric strength measurements", in *Proceedings of 26th Scientific Meeting of ISMRM*, 2018, p. 4742.

CP-12 D. Weidlich, S. Ruschke, **B. Cervantes**, A. Hock, and D. C. Karampinos, "Adc quantification of lipids with high b-value stimulated echo-prepared diffusion-weighted 2d single shot tse", in *Proceedings of 26th Scientific Meeting of ISMRM*, 2018, p. 4985.

CP-13 A. T. Van, **B. Cervantes**, T. Ogino, H. Peeters, A. Hock, E. J. Rummeny, R. Braren, and D. C. Karampinos, "Partial velocity-compensated diffusion encoding for combined motion compensation and residual vessel signal suppression in liver dwi", in *Proceedings of 26th Scientific Meeting of ISMRM*, 2018, p. 1577.

CP-14 T. Baum, S. Schlaeger, S. Inhuber, F. Kreuzpointer, M. Dieckmeyer, F. Freitag, E. Klupp, **B. Cervantes**, A. Schwirtz, J. S. Kirschke, and D. C. Karampinos, "Association of thigh muscle fat infiltration with isometric strength measurements based on chemical shift encoding-based water-fat mri", in *Proceedings of 26th Scientific Meeting of ISMRM*, 2018, p. 465.

CP-15 A. T. Van, **B. Cervantes**, H. Kooijman, and D. C. Karampinos, "Compensating for eddy current effects in motion-compensated diffusion-prepared tse sequences", in *Proceedings of 25th Scientific Meeting of ISMRM*, 2017, p. 3924.

CP-16 S. Schlaeger, E. Klupp, D. Weidlich, **B. Cervantes**, M. Deschauer, B. Schoser, S. Bublitz, F. Montagnese, C. Katemann, H. Kooijman, E. J. Rummeny, C. Zimmer, J. S. Kirschke, and D. C. Karampinos, "T2-weighted dixon tse for accelerated simultaneous grading of whole body skeletal muscle fat infiltration and edema in patients with neuromuscular diseases", in *Proceedings of 25th Scientific Meeting of ISMRM*, 2017, p. 5011.

CP-17 Q. Zhang, **B. Cervantes**, D. C. Karampinos, B. F. Coolen, A. J. Nederveen, and G. J. Strijkers, "High resolution 3d diffusion imaging of carotid vessel wall using stimulated echo based diffusion prepared turbo spin echo sequence", in *Proceedings of 24th Scientific Meeting of ISMRM*, **ISMRM Summa Cum Laude Award**, 2016, p. 959.

CP-18 D. Weidlich, **B. Cervantes**, N. Sollmann, H. Kooijman, E. J. Rummeny, A. Haase, J. S. Kirschke, and D. C. Karampinos, "B1-insensitive high-resolution isotropic t2 mapping of the lumbar plexus with a t2-prepared 3d tse", in *Proceedings of 24th Scientific Meeting of ISMRM*, 2016, p. 4469.

CP-19 A. T. Van, **B. Cervantes**, E. J. Rummeny, A. Haase, and D. C. Karampinos, "How to minimize motion-induced phase and magnitude modulation in diffusion-prepared sequences", in *Proceedings of 24th Scientific Meeting of ISMRM*, 2016, p. 3289.

CP-20 E. Klupp, D. Weidlich, T. Baum, **B. Cervantes**, M. Deschauer, H. Kooijman, E. J. Rummeny, C. Zimmer, J. S. Kirschke, and D. C. Karampinos, "Comparison of t2-prepared 3d tse with multi-echo spin echo sequences for t2 mapping of the thigh musculature", in *Proceedings of 24th Scientific Meeting of ISMRM*, 2016, p. 4511.

CP-21 P. Cornejo, **B. Cervantes**, A. Pokorney, J. Miller, D. C. Karampinos, and H. H. Hu, "High resolution lumbar neurography with 3d turbo spin echo mri: Initial experience in children", in *Proceedings of 24th Annual Meeting of ASNR*, 2016.

CP-22 D. Weidlich, **B. Cervantes**, H. Kooijman, E. J. Rummeny, A. Haase, and D. C. Karampinos, "Diffusion sensitivity of high-resolution 3d tse in a clinical 3 t system: Implications for peripheral nerve imaging", in *2015 International Conference on Magnetic Resonance Microscopy*, 2015.

Co-Authored Patents

P-1 D. Karampinos, **Cervantes, B.**, A. T. Van, and H. E. H. Kooijman, "Correction of motion-induced phase errors in multi-shot diffusion-prepared turbo spin echo imaging", 2017ID03874, *in preparation*.

Contents

Introduction

1.1 Magnetic Resonance Neurography (MRN)

Magnetic Resonance Imaging (MRI) of proximal and distal nerves in the body, referred to as magnetic resonance neurography (MRN), is an imaging tool that currently serves as a non-invasive diagnostic alternative to electrophysiology in the evaluation of neuropathy and nerve generation [1]. Thanks to the excellent soft-tissue contrast characteristic of MRI and to recent advances in high-resolution two-dimensional (2D) and three-dimensional (3D) MR imaging, MRN is used in the diagnosis and treatment of peripheral neuropathy by exposing abnormalities caused by nerve lesions, muscle denervation, neurofibromatosis and nerve entrapment, among other applications, as well as to provide guidance for perineural injections [2–7].

MRN comprises an assortment of imaging methods that utilize various contrast-generating mechanisms and combine 2D and 3D imaging [8]. Among the contrast mechanisms available in MRI, morphological T_2-weighted imaging is used conventionally in MRN for the evaluation of neural pathologies such as changes in signal intensity, course, shape, size, fascicular pattern, and for the detection of fibrosis or mass lesions [5]. 2D techniques are conventionally used for inspecting the inner structure of nerve fibers using high in-plane resolution, while 3D methods are widely used for isotropic-resolution imaging of nerves with intricate geometries [9]. Given the small size of most nerves in the body and the prevalent presence of field inhomogeneity in diverse anatomical regions, MRI methods capable of achieving good signal quality at high resolutions while being robust to distortion artifacts are mostly preferred in MRN.

Morphological MRN requires high nerve contrast. Since nerves are embedded either in muscle or fat, muscle-signal attenuation and uniform fat suppression are techniques frequently encountered in MRN. Given the necessity of high nerve signal and the presence of field inhomogeneity in the body, careful considerations need to be taken when choosing a method for fat suppression. MRN also requires the suppression of signal from adjacent vessels that otherwise can obscure nerve visibility. Vessel suppression in MRN is conventionally achieved using motion-sensitizing methods. A major challenge that persists in using such methods, however, is the difficulty to address unwanted signal from small vessels without disrupting the signal of nerves [10], given the similar T_1 relaxation times between blood and nerves and the long T_2 relaxation times of the two tissues.

Morphological MRN alone can be insufficient in identifying nerve injury, which is why quantitative methods are needed for a more precise diagnosis of neuropathy [11–13]. Quantitative methods such as diffusion-weighted imaging (DWI) and diffusion tensor imaging (DTI) have the ability to probe the microstructural functionality of nerve fibers [14, 15] and are therefore used to obtain structural information that morphological MRN methods are incapable of providing [16–19].

1.2 Purpose of Thesis

As emphasized in Section 1.1, MRN is becoming a highly valuable tool in the clinical diagnosis and treatment of injury and disease of nerves in the body. Given the relative recent demand for MRN in clinical applications, however, the development of MR methods that fulfil the specific needs in nerve imaging continues to be a relatively novel field that requires major advancement. This doctoral thesis had the aim to address a number of the most relevant technical challenges that persist in MRN by means of the development and improvement of techniques ranging from advanced methods for state-of-the-art morphological imaging to an elaborate quantitative technique that overcomes major imaging difficulties and is able to assess nerve microstructure.

1.3 Structure of Thesis

The present cummulative doctoral thesis has as its foundation the three journal publications listed in Chapter and provided in Chapter 5. The methodology developed for the enclosed journal publications is introduced in Chapter 3, for which corresponding background is provided in Chapter 2. Lastly, the presented journal publications are discussed in past, current and future perspectives in Chapter 6.

Background

2.1 Rapid Acquisition with Relaxation Enhancement (RARE) Imaging

Rapid acquisition with relaxation enhancement (RARE), also known as fast spin echo (FSE) and turbo spin echo (TSE), is an accelerated spin-echo sequence consisting of an RF excitation pulse followed by a train of refocusing pulses [20, 21], in which a spin echo is generated for each refocusing pulse. Acceleration in RARE sequences is accomplished by means of the individual spatial encoding of each produced spin echo, this way allowing the acquisition of multiple k-space trajectories for a given excitation pulse. Although other encoding techniques such as echo planar imaging (EPI) are capable of faster imaging, RARE sequences have the advantage of being highly insensitive to off-resonance effects such as main B_0 field and (tissue) susceptibility inhomogeneities.

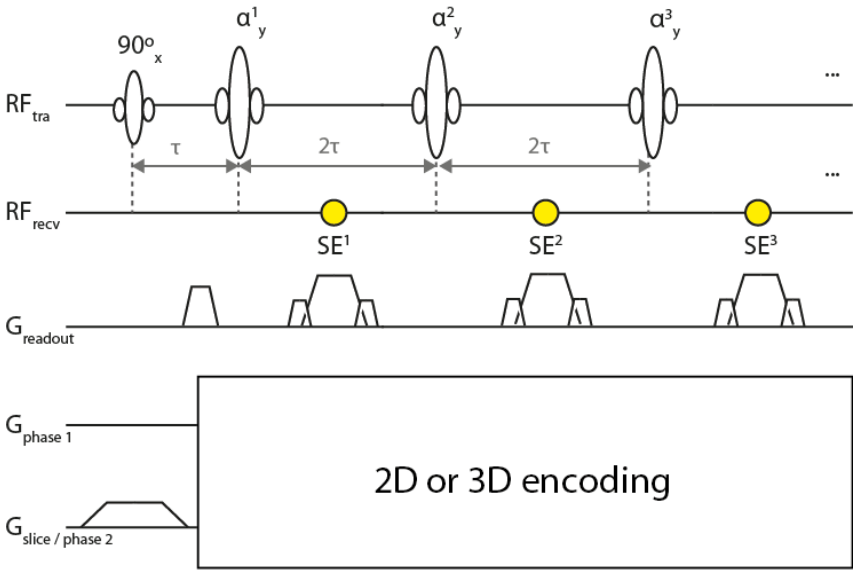

Figure 2.1: Rapid Acquisition with Relaxation Enhancement (RARE) Sequence. The sequence consists of selective 90° excitation followed by a train of refocusing pulses α^i (i = 1, ..., ETL). The phase of the refocusing pulses (y) is shifted by 90° with respect to the phase of the excitation pulse (x). Refocusing pulses are separated by twice the time between the excitation pulse and the first refocusing pulse, τ. A crusher gradient is commonly placed in the readout direction prior to the formation of each echo to eliminate undesired FID signals.

Figure 2.1 shows a RARE sequence. Excitation in RARE uses a flip angle of 90° while each refocusing pulse i in the train can have a different flip angle α^i of up to 180°. The total

number of spin echoes generated per TR is equivalent to the number of refocusing pulses following an excitation pulse and is referred to as the *echo train length (ETL)*. The readout of echoes in a RARE echo train employs identical gradient lobes to frequency-encode each echo while spatial encoding varies between 2D and 3D acquisitions as well as with the desired image contrast.

Single-Shot and Multishot RARE

RARE sequences are divided into single-shot and multishot sequences. Single-shot RARE acquires the entire k-space data necessary to reconstruct an image in a single echo train (or *shot*), while multishot RARE acquires a fraction of the k-space data in each shot and in the end combines the k-space data from all shots for image reconstruction. In order to achieve high resolutions, single-shot RARE needs to use long ETLs, which are frequently still insufficiently long to acquire the entire number of phase-encoding steps for full k-space coverage, thus requiring the reduction of acquired k-space lines in a shot (*e.g.,* with parallel imaging acceleration). Single-shot RARE is therefore compromised in SNR and in attainable spatial resolution and is limited to 2D imaging. Moreover, since blurring along the turbo phase-encoding direction in RARE imaging increases with echo spacing and echo train length, single-shot RARE is also characterized and limited by blurring. Multishot RARE, on the other hand, can use shorter ETLs and can therefore offer higher resolutions, higher SNR and decreased blurring, and is the method of choice for 3D imaging. Image quality in multishot RARE is further influenced by the scheme used to sample k-space, since T_2 decay along the echo train and the associated modulation of k-space data will result in different signal-intensity and blurring effects depending on the way k-space is sampled.

3D RARE

3D spatial encoding in RARE imaging enables higher SNR efficiency than 2D encoding as well as the acquisition of thin contiguous slices within reasonable times. 3D imaging is therefore preferred in many isotropic-resolution applications and whenever higher SNR is needed. 3D RARE can use selective or non-selective refocusing, but non-selective refocusing is normally preferred since it reduces the spacing between refocusing pulses and consequently increases the acquisition efficiency of the sequence. Phase encoding along the echo train in 3D RARE is applied in the primary (denoted *turbo*) direction G_{phase1} and phase encoding in the secondary direction G_{phase2} is carried out as in 2D encoding, one phase-encoding step per TR (shot).

Low-Flip-Angle Refocusing and Echo Formation

With the purpose of reducing RF energy deposition and consequently the specific absorption rate (SAR) in an object, RARE sequences are commonly implemented with refocusing pulses using flip angles smaller than 180°. The introduction of low flip angles into a RARE sequence, however, has additional intricate effects on the RARE signal, which need to be understood and taken into account for maintaining the proper performance of the sequence [21].

Low-flip-angle multi-pulse refocusing in RARE sequences effectively enables partial excitation, partial refocusing and partial restoration of signal in each refocusing pulse, depending on the type of magnetization being affected. Transverse magnetization that expe-

riences a phase reversal at every refocusing pulse produces a type of spin echo customarily denoted *primary spin echo*. Longitudinal magnetization that is partially excited by a refocusing pulse will produce an FID signal and, when further phase-reversed by following refocusing pulses, will also produce a type of spin echo called *secondary spin echo*. Further, whenever transverse magnetization is partially restored to the longitudinal axis by a refocusing pulse and then reexcited by a subsequent refocusing pulse, a *stimulated echo* will be formed. Therefore, three families of echoes are produced in a RARE sequence.

The CPMG Condition

The formation of three types of echoes in low-flip-angle refocusing introduces a complexity into RARE imaging that requires specific requirements to be met in the sequence design. Namely, the temporal positon of the refocusing pulses and their phases need to be adjusted so that echoes are formed at the desired time points and in phase, thus giving way to constructive signal interference. The specifications for assigning the timings and phases to the refocusing pulses in a RARE sequence are collectively referred to as the *Carr-Purcell-Meiboom-Gill (CPMG) condition* [22] and consist of the following two criteria:

1. The phase of the refocusing pulses (y) is shifted by 90° with respect to the phase of the excitation pulse (x); and consecutive refocusing pulses are separated by twice the time between the excitation and the first refocusing pulse (τ in Figure 2.1).

2. The phase gathered by a spin isochromat between any two consecutive refocusing pulses must be equal.

RARE sequences that satisfy the CPMG condition use the superposition of primary spin echoes and stimulated echoes (FID signals and secondary spin echoes are eliminated with crusher gradients). In terms of sequence design, the CPMG condition requires that all gradients incorporated into the sequence are balanced throughout the echo train so that they don't alter the relative phase among echoes. Further, the CPMG condition for the conventional RARE sequence (Figure 2.1) will be violated by spins carrying any additional inconsistent phase, such as moving spins.

Signal Modulation and Blurring

Given either pure T_2 decay (perfect 180° refocusing) or mixed T_1 and T_2 decay (low-flip-angle refocusing) throughout an echo train, a certain signal modulation in in the primary phase encoding direction will result, leading to blurring in that direction in the reconstructed image. Flip angle modulation in RARE sequence design [23, 24] is commonly used to balance relaxation-induced signal loss in an echo train, which can considerably reduce blurring in the primary phase-encoding direction. The ordering of echoes into k-space [25] will further influence how signal modulation is mapped and therefore the type of blurring that will result. Blurring is, therefore, an inevitable artifact in RARE imaging.

2.2 Motion Sensitized Driven Equilibrium Magnetization Preparation

MR methods that produce images with suppressed blood signal, commonly referred to as *black-blood* methods, are necessary in many MR imaging applications where the inten-

sity of blood signal contaminates the region of interest. Two methods typically used for black-blood imaging are double-inversion recovery (DIR) [26, 27] and spatial presaturation (SAT) [28, 29]. A requirement of the DIR and SAT methods for suppressing blood signal is that the complete inflow of tagged (inverted or saturated, respectively) blood spins into the imaged slice or slab takes place. DIR and SAT black-blood 2D imaging is feasible as long as the imaging slices are thin enough to contain the tagged spins, which for many applications is generally the case. 3D imaging with the DIR and SAT methods, however, is difficult to achieve since the complete inflow of tagged spins into the imaged slab might not be possible. A technique for overcoming the requirement of complete tagged inflow, originally called driven equilibrium Fourier transform (DEFT) diffusion preparation, was proposed by Koktzoglou et al. [30] for 3D black-blood imaging. Since the DEFT method is mainly used for motion sensitization opposed to diffusion sensitization, DEFT diffusion preparation is more frequently referred to as motion-sensitized driven-equilibrium (MSDE) [31].

Motion-Sensitized Driven-Equilibrium (MSDE)

Figure 2.2 shows an MSDE preparation sequence. MSDE preparation consists of a 90°_x – $180^\circ_y - 90^\circ_{-x}$ sequence of nonselective (hard) pulses and symmetric motion-sensitizing gradients that have empirically determined properties for dephasing moving blood spins [31–35]. A spoiler gradient is applied after the preparation period to spoil remaining transverse magnetization.

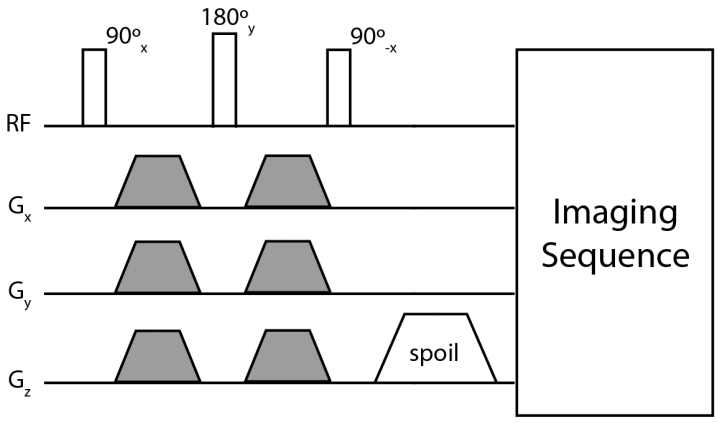

Figure 2.2: Motion-Sensitized Driven-Equilibrium (MSDE) Preparation. The driven-equilibrium RF configuration consists of 90°_x excitation, 180°_y refocusing and 90°_{-x} restoration (or tip-up) of signal. Motion-sensitizing gradients (gray) are placed symmetrically around the refocusing RF pulse and can be enabled in all three encoding axes. A spoiling gradient following signal restoration dephases remaining transverse magnetization.

Improved MSDE (iMSDE)

The MSDE sequence is mainly limited by signal loss [31] induced by T_2 relaxation, diffusion and field imperfections such as eddy currents and transmit B_1 inhomogeneity. Multiple efforts were made by Wang et al. to increase the robustness of MSDE to field imperfections by means of modifying the RF design of the sequence [36]. The improved motion-sensitized driven-equilibrium (iMSDE) (Figure 2.3) sequence uses double 180° MLEV-4 refocusing [37], where the type of refocusing pulse can vary.

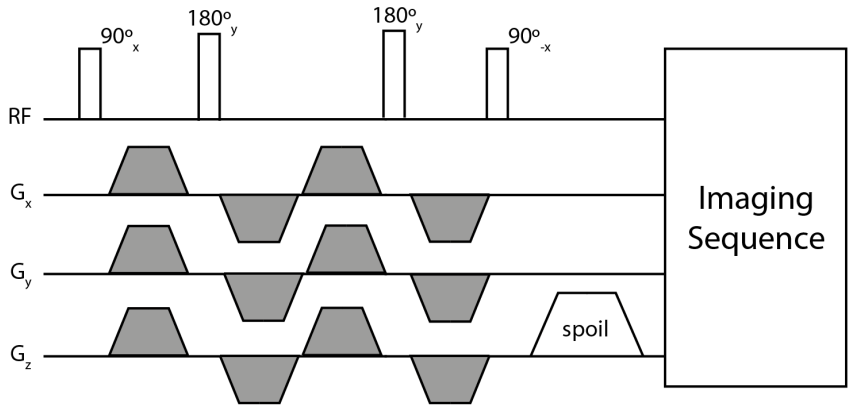

Figure 2.3: Improved Motion-Sensitized Driven-Equilibrium (iMSDE) Preparation. Two 180° refocusing pulses and alternating motion-sensitizing gradients (gray) are used to improve the sequence's performance in the presence of eddy currents and B_1 inhomogeneity.

Because of the nature of the motion-sensitizing gradients used in iMDSE sequences, signal quality is also dictated by the first-order gradient moment (m_1) and by the spin velocity distribution within a voxel. That is, applications that require high m_1 values, such as those needing suppression of slow-flowing blood, might need additional modifications of the sequence in order to avoid m_1-induced deterioration of image quality.

2.3 Diffusion Imaging

The concept of self diffusion was first introduced by Albert Einstein in 1905 in his studies of Brownian motion [38]. Diffusion is effectively defined as the microscopic flux of particles in a medium that results from a gradient in the particle concentration. Einstein proposed that self diffusion, unlike diffusion, also leads to the result of particle flux but originates purely in the presence of local concentration fluctuations by means of random particle motion, referred to as Brownian motion. Macroscopically, Brownian motion of a species of molecules can be observed and is described by a quantity specific to that molecular species, called the diffusion coefficient. Einstein described macroscopic diffusion statistically as

$$< X >^2 = 2DT_d, \tag{2.1}$$

where $< X >^2$ is the average mean-squared distance travelled by an ensemble of molecules by means of diffusion in a single direction in a given period of time T_d, referred to as the diffusion time, and D is the diffusion coefficient.

Nuclear magnetic resonance (NMR) is unique in that it is the only technique that can non-invasively detect molecular diffusion in a microscopic scale. The translation of diffusion NMR principles to magnetic resonance imaging (MRI), enabling the generation of quantitative maps containing information about the molecular dynamics and structural properties of biological systems, has thus led to an enormous interest in the medical sciences to develop the methodology necessary to achieve better and more precise diffusion measurements.

Diffusion Encoding

MRI pulse sequences can be diffusion sensitized by incorporating magnetic field gradients with amplitudes and durations large enough to be sensitive to diffusion processes. Diffusion gradients induce a change in the resonant frequency $\Delta\omega$ of the spin ensemble affected by Brownian motion that over a time t results in a phase accumulation ϕ:

$$\phi = \int_0^t \Delta\omega \mathrm{d}t' = \gamma \int_0^t \mathbf{G}(t') \cdot \mathbf{r}(t') \mathrm{d}t' \tag{2.2}$$

where γ is the gyromagnetic ratio, **G** is the applied gradient waveform and **r** is the spatial position of the affected spins. Molecules carrying a phase ϕ are effectively labeled according to their diffusion properties and will yield an MR signal that is diffusion encoded. Namely, the measured diffusion signal is exponentially related to the variance of the Gaussian distribution of the phase accumulated by the spin ensemble undergoing diffusion, $< \phi^2 >$, and is described as:

$$S = S_0 \exp(- < \phi^2 >), \tag{2.3}$$

where S_0 is the signal in the absence of diffusion.

Various MR schemes exist for diffusion encoding. Stejskal and Tanner introduced the pulsed field gradient (PFG) technique in 1965, most widely used since then in diffusion MRI. The signal measured with the pulsed field gradient spin echo (PFGSE) sequence employing trapezoidal diffusion gradients, shown in Figure 2.4, is described by [39]:

$$S = S_0 \exp\{-\gamma^2 G^2 \delta^2 [(\Delta - \delta/3) + \epsilon^3/30 - \delta\epsilon^2/6] D\}, \tag{2.4}$$

where G, δ, Δ and ϵ are the strength, duration, temporal separation and ramping duration of the trapezoidal diffusion-encoding gradients, respectively.

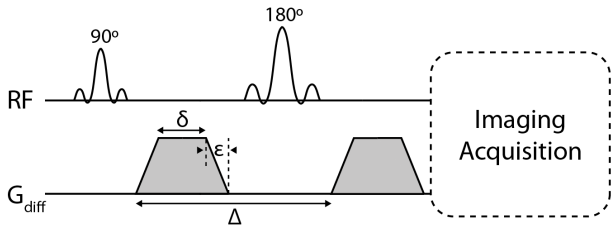

Figure 2.4: Pulsed Field Gradient Spin Echo (PFGSE) Sequence. Trapezoidal diffusion gradients (gray) are placed symmetrically around the refocusing RF pulse and occupy most of the available time to maximize diffusion sensitivity.

A disadvantage of the spin-echo based PFGSE method is that increasing the diffusion time, which is necessary for achieving higher diffusion sensitivity, results in signal loss induced by T_2 relaxation. This problem is partially alleviated by the stimulated-echo approach proposed by Tanner in 1970 [40], which offers relatively longer diffusion times without the penalty of signal loss from T_2 relaxation. Gradient echo diffusion sequences exist but are less frequently used due to their sensitivity to T_2^* relaxation effects and therefore to the associated short echo times required for maintaining acceptable SNR. Steady-state free precession (SSFP) diffusion sequences, which incorporate gradient-echo-based diffusion encoding, overcome T_2^*-relaxation related signal loss but are in general highly complex and susceptible to motion artifacts.

The b-Factor

Regardless of the method used for diffusion encoding, the description of the signal measured in a diffusion experiment can be simplified by means of the so called b-factor, which is a quantity that represents the diffusion sensitivity of the sequence. The b-factor encompasses the effective gradient waveform **G** of the diffusion sequence and is defined as [41, 42]:

$$b = \gamma^2 \int_0^{TE} \Big[\int_0^t \mathbf{G}(\mathbf{t}') \mathrm{d}t' \Big] \mathrm{d}t, \tag{2.5}$$

where TE is the echo time of the diffusion-sensitized sequence. It is important to note that the b-factor can only be used to describe free or isotropic diffusion. The assessment of anisotropic diffusion is described in Section 2.3.

Noting the relationship between the phase ϕ in Equation 2.2 and the definition of the b-factor in Equation 2.5, the Equation 2.3 can be written as:

$$S = S_0 \exp(-bD). \tag{2.6}$$

In words, molecules undergoing Brownian motion that are affected by diffusion gradients yield an MR signal that is exponentially attenuated in proportion to their diffusion coefficient as well as to the diffusion sensitivity of the MR diffusion encoding sequence.

Spatial Encoding in Diffusion Imaging

Spatial encoding in diffusion imaging requires careful considerations. Schemes that require multiple k-space segments for the formation of a single diffusion image, which consequently require individual diffusion encodings for each k-space segment, are highly prone to unwanted phase shifts that originate from coherent and incoherent motion occurring during the diffusion encoding period. The incorporation of k-space segments carrying different phase shifts into the reconstruction of the diffusion image results in imaging artifacts in the phase encoding direction, leading to incorrect and thus meaningless diffusion information. Such diffusion-sensitized multishot methods therefore require additional design modifications as well as dedicated handling of the diffusion-encoded signals in the image reconstruction, as discussed in detail in Section 2.3. Diffusion-sensitized single-shot techniques, where all echoes required to form a diffusion image are obtained in a single acquisition period, avoid motion-induced artifacts but are in general associated with spatial resolution limitations.

Diffusion Tensor Imaging

Molecular mobility in biological tissues is frequently restricted, preventing diffusion to take place uniformly in all spatial orientations. Since diffusion gradients can only encode motion in the same direction in which they are applied, the observed diffusion-encoded signal of molecules moving in a preferred orientation will be different for different gradient directions.

Anisotropic diffusion cannot be described by a single scalar diffusion coefficient and requires a dedicated formulation to describe the observed MR signal. The diffusion tensor was introduced in 1960 by Wilhelm Jost to describe diffusion along each orthogonal axis

as well as the correlation among all axes. The diffusion tensor **D** is defined as:

$$\mathbf{D} = \begin{bmatrix} D_{xx} & D_{xy} & D_{xz} \\ D_{xy} & D_{yy} & D_{yz} \\ D_{xz} & D_{yz} & D_{zz} \end{bmatrix}. \tag{2.7}$$

In the principal or main direction of diffusivity of the observed tissue, $[x', y', z']$, the diffusion tensor is reduced to only its diagonal terms $D_{x'x'}$, $D_{y'y'}$ and $D_{z'z'}$, which represent molecular mobility in the x', y' and z' directions, respectively. The measured diffusion-encoded signal of molecules experiencing anisotropic diffusion is expressed in the reference frame of the tissue as:

$$S = S_0 \exp(-\mathrm{b}_{x'x'} - \mathrm{b}_{y'y'} - \mathrm{b}_{z'z'}), \tag{2.8}$$

where b_{ii} are now the elements of the b-matrix, which replaces the b-factor described by Equation 2.5. Experimental diffusion measurements are made in the reference frame of the gradients [x, y, z] and not in that of the tissue. In the gradient reference frame, where the nondiagonal elements of the b-matrix and of the diffusion tensor couple with one another, the measured signal becomes:

$$S = S_0 \exp(\sum_{i=x,y,z} \sum_{j=x,y,z} \mathbf{b}_{ij}\mathbf{D}_{ij}). \tag{2.9}$$

The estimation of the diffusion tensor is necessary to measure anisotropic diffusion. Once the diffusion tensor is obtained, multiple metrics can be derived that describe the microscopic structure of the measured tissue. The root mean squared (rms) dispalcement of particles diffusing in a medium is commonly described by the *diffusion ellipsoid*. Diffusion taking place in an isotropic medium is associated with a spherical diffusion ellipsoid. For the case of diffusion in anisotropic media, the diffusion ellipsoid is either prolate or oblate and its three principal directions coincide with the eigenvectors of **D**.

The *eigenvalues* of the diffusion tensor, denoted λ_1, λ_2 and λ_3, are rotationally invariant scalars that quantify the length of the main axes of the diffusion ellipsoid and collectively describe its shape. The *axial diffusivity* $\mathrm{AD} = \lambda_1$ describes diffusion along the main axis of the diffusion ellipsoid. Conversely, the *radial diffusivity* $\mathrm{RD} = (\lambda_2 + \lambda_3)/2$ describes diffusion in the plane of least diffusivity. Moreover, the *mean diffusivity* $\mathrm{MD} = (\lambda_1 + \lambda_2 + \lambda_3)/3$ describes the orientation-averaged diffusion. Lastly, a parameter used to characterize the effective shape of the diffusion ellipsoid, or the degree of anisotropy in a medium, is the *fractional anisotropy*:

$$FA = \sqrt{\frac{1}{2}\frac{(\lambda_1 - \lambda_2)^2 + (\lambda_1 - \lambda_3)^2 + (\lambda_2 - \lambda_3)^2}{\lambda_1^2 + \lambda_2^2 + \lambda_3^2}}. \tag{2.10}$$

Phase Errors in Diffusion Imaging

The sensitivity of diffusion MRI for detecting microscropic motion has the unavoidable disadvantage of also being susceptive to all kinds of motion of larger scales. Macroscopic motion in in vivo imaging can originate from multiple sources, ranging from subject motion to cardiac-produced pulsations, breathing and involuntary organ movement. In most cases, however, macroscopic motion occurs in an unpredictable, unreproducible manner. Therefore, since non-diffusion motion occurring during the diffusion-encoding period of a

diffusion acquisition affects the diffusion-encoded phase in an unaccountable manner, the resulting phase effects will interfere with subsequent spatial encoding and consequently with image reconstruction.

Motion taking place during a diffusion acquisition leads to the accumulation of an additional phase on the diffusion-encoded signal that is proportional to the speed of motion [43]. Depending on the type of non-diffusion motion, the distributions in k-space and in image space of the resulting accumulated phase will take on different characteristics. It can be shown that translational motion in the direction of the applied diffusion-encoding gradient produces a uniform phase shift both in k-space and in image space, while rotational motion about an axis perpendicular to the applied gradient generates a shift of the center of k-space and consequently, according to the Fourier shift theorem, a linear phase in image space. Rigid body motion, which is a combination of translational and rotational motion, therefore results in a phase distribution with offsets in k-space and with constant and linear variations in image space. In practice, however, motion disrupting a diffusion acquisition will not be purely rigid and will accumulate a nonlinear phase on the diffusion-encoded signal in the image domain.

Methodology

3.1 Flip Angle Optimization of the 3D Turbo Spin Echo Sequence

Need for Isotropic High-Resolution 3D Imaging

Magnetic resonance imaging of the nervous system in the body has become an increasingly used diagnostic tool in the assessment of nerve lesions [1]. Isotropic, high-resolution 3D MR imaging particularly provides high accuracy in the evaluation of nerves with high obliqueness. Due to its robustness to off-resonance and susceptibility effects, 3D spin echo imaging based on rapid acquisition with relaxation enhancement (RARE), also known as 3D fast spin echo (FSE) and 3D turbo spin echo (TSE), has become a reliable technique for realizing isotropic, high-resolution T_2-weighted imaging of nerves with complex geometries [44, 45]. These sequences are, however, inevitably affected by blurring artifacts as well as by the compromise between achieving the spatial resolution needed to delineate small nerves and the requirement of sufficient signal needed to visualize fine nerve structures.

Characterization of the TSE Signal

Section 2.1 described the principles of TSE sequences. Figure 3.1 shows a 3D TSE sequence employing variable flip angles. For a material with a known relaxation time T_2, the observed magnitude of the nth echo in a TSE train employing perfect 180° refocusing pulses is expressed as

$$s_n = s_0 \exp(-TE_n / T_2) \tag{3.1}$$

where s_0 is the echo magnitude prior to dephasing and relaxation and $TE_n = n\,2\tau$ is the time of the corresponding echo formation with respect to the first refocusing pulse. In the case where the refocusing pulses employ low flip angles (*i.e.,* $\alpha < 180°$), the amplitude of the nth echo will depend on T_2, T_1 and on the flip angles of all preceding refocusing pulses. Therefore, finding an analytical expression of the signal observed throughout the echo train of a TSE sequence employing low-flip-angle refocusing becomes highly complex and unpractical. Extended phase graphs (EPGs) [21, 46–55] are a numerical tool that computes the Fourier decomposition of the magnetization in evolving dephasing states along an echo train. EPGs can quantize the magnetization along all spin-echo and stimulated-echo pathways [55] and are therefore a popular alternative for assesing the signal response of pulse sequences with long flip angle trains.

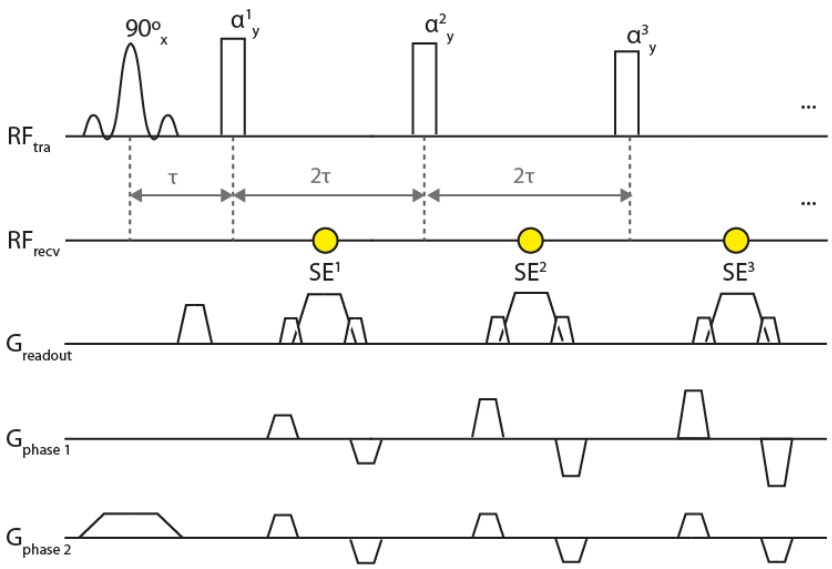

Figure 3.1: 3D Turbo Spin Echo (TSE) Sequence. A train of refocusing pulses with flip angles α^i (i = 1, ..., ETL) follows 90° excitation. The timing and phases of all RF pulses is set according to the CPMG condition.

3.1.1 Tissue-Specific Flip Angle Design

Numerical tools such as EPGs further allow the computation of flip angles for the refocusing pulses in a TSE train in order to meet user-defined signal requirements [23]. Tissue-specific flip angle modulation consists of specifying objective intensities for the echoes in the TSE train and calculating the flip angles that produce these intensities given known T_1 and T_2 values and sequence parameters. For a given imaging application, the signal response of a tissue of interest can therefore be tailored to have specific properties by means of designing an appropriate flip angle scheme.

Tissue-specific flip angle trains generated with EPGs in this work were obtained from desired k-space signals along the TSE echo train, namely consisting of a signal plateau with high intensities for most of the echoes in the train. The generated flip angles had an initial stage of quickly decreasing flip angles in order to reach a temporary steady state, referred to as pseudo steady state (PSS), that is necessary for reducing signal oscillations [56–58] and maintaining a steady signal throughout the echo train. Flip angle modulation followed the PSS stage in a free fashion and finalized in an increasing linear manner, a common flip angle design that slows the effective rate of T_2 relaxation and at the end uses the resulting reservoir of longitudinal magnetization to maximize signal generation steadily throughout the echo train and to reduce blurring. Figure 3.2 shows an example of a tissue-specific flip angle design for a TSE sequence and the corresponding signal responses simulated with EPGs for two tissues.

3.1.2 Geometry-Specific Optimization

In multi-tissue imaging, the interaction between the blurring mechanisms of two neighboring tissues determines the appearance at their interface. The geometry of the imaged tissues also influences the effective blurring mechanisms, since blurring in imaging of large embedded objects results in a loss of edge sharpness and in imaging of small embedded

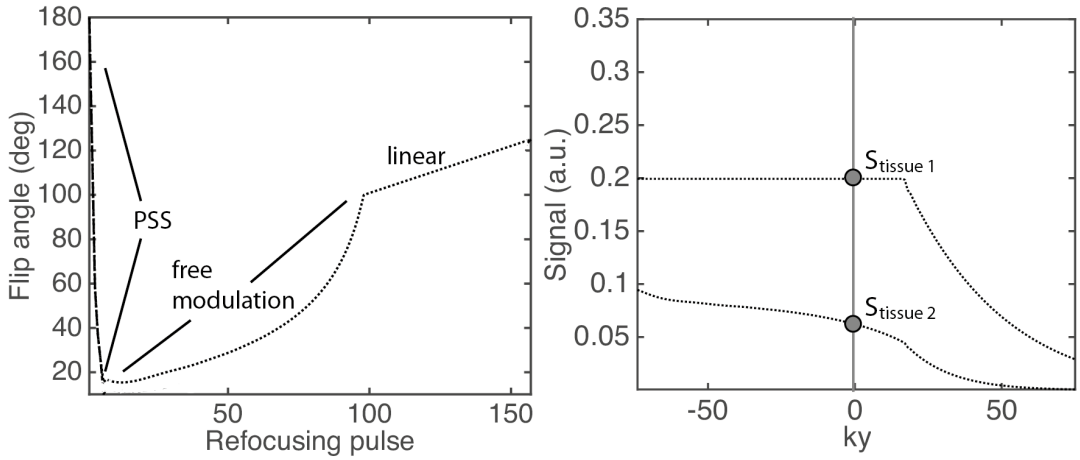

Figure 3.2: Flip Angle Modulation and Signal Response. The flip angle design (left) consists of a rapid pseudo steady state (PSS) decrease followed by free modulation and ending in a linear increase. The corresponding signal response simulated with EPGs (right) for the tissue of interest (tissue 1) consists of a signal plateau followed by T_2 decay. Flip angle modulation yields less steady signal and more pronounced T_2 decay for a second affected tissue (tissue 2). Signal decay at high ky values leads to k-space filtering of high frequencies and thus to blurring after image reconstruction. ETL = 150.

objects additionally can result in a loss of signal intensity [59, 60]. In the present work, the effects of flip angle design in 3D TSE on signal loss and blurring of small embedded objects were assessed and used for the development of an optimization scheme for flip angles that balances signal intensity and sharpness.

The trade-off between signal intensity and width broadening for small embedded objects was evaluated by means of simulating, within a constrained sequence-parameter space, the k-space signal response of an embedded object with specific relaxation properties in different geometric settings. Signal intensities were obtained directly from the echo amplitudes at the k=0 positions in all echo trains while width broadening was measured from the spatial blurring of the simulated geometric profiles induced by each image-space signal response. The optimized configuration of sequence parameters was then defined as the point in the user-defined sequence-parameter space at which maximum signal is reached with a minimum width broadening.

3.2 Motion- and Diffusion-Sensitized Magnetization Preparation

The improved motion-sensitized driven-equilibrium (iMSDE) sequence was described in Section 2.2. The iMSDE sequence including modifications for body imaging that was used in this work is illustrated in Figure 3.3.

The signal of spins moving with constant velocity dx/dt observed after motion encoding in the y direction and before the 90°_{-x} (tip-up) pulse is described as

$$M_{xy}^{-} = M_0\, e^{-\mathrm{b}D} \int_{\Delta y} e^{i\phi(y)}\, dy \tag{3.2}$$

where M_0 is the magnetization prior to any dephasing, b is the b-factor associated with the

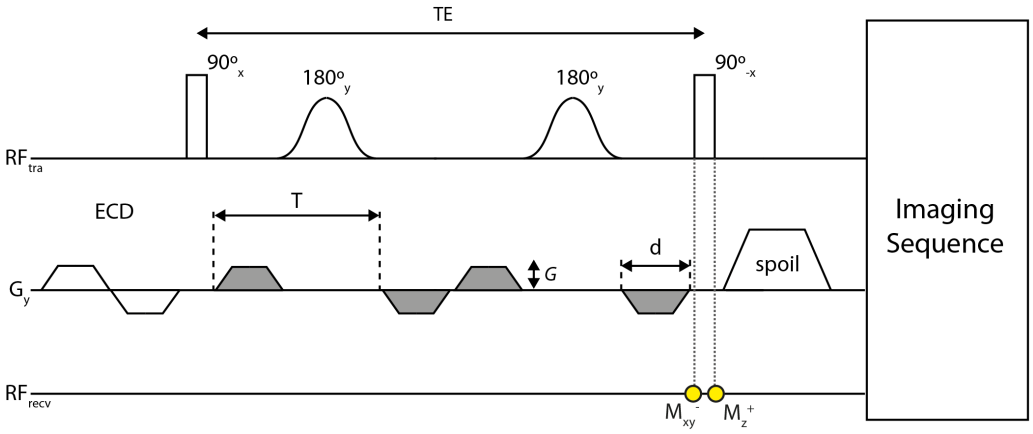

Figure 3.3: Improved Motion-Sensitized Driven-Equilibrium (iMSDE) Preparation Sequence. For the RF component, a DRHS design is used to improve robustness against B_0 and B_1 inhomogeneities. Motion-sensitizing gradients (gray) applied in the y direction have strength G, duration d and separation T. A pair of bipolar gradients precedes excitation for the minimization of eddy currents.

effective waveform of the motion-sensitizing gradients, D is the diffusion attenuation coefficient of the imaged material, Δy is the dimension of the imaged voxel in the y-direction and $\phi(y)$ is the phase accumulated by the moving spins at position y within the voxel. The signal of moving spins is therefore affected both by diffusion effects as well as by dephasing due to coherent motion.

Dephasing Induced by Coherent Motion

The phase accumulated by coherently moving spins within a voxel after motion encoding in the y direction can be described as having two contributions, ϕ_0 and $\phi_{\text{intra}}(y)$

$$\phi(y) = \phi_0 + \phi_{\text{intra}}(y). \tag{3.3}$$

The term ϕ_0 is the induced phase at the center of the voxel conveying the average velocity, acceleration and higher-order terms of the contained spins. The term $\phi_{\text{intra}}(y)$ represents the phase accumulation at position y in the voxel and scales with the intravoxel velocity dispersion at that position. These two dephasing mechanisms are described as

$$\begin{aligned} \phi_0 &= \gamma \int_0^t G(t') \cdot \overline{x}_{\Delta y} dt' \\ &= \gamma \left[m_0 \left(\overline{\frac{d^0 x}{dt^0}} \right)_{\Delta y} + m_1 \left(\overline{\frac{dx}{dt}} \right)_{\Delta y} + \text{higher orders} \right] \end{aligned} \tag{3.4}$$

and

$$\phi_{\text{intra}}(y) = \gamma \left[m_0 \frac{d^0 x(y)}{dt^0} + m_1 \frac{dx(y)}{dt} + \text{higher orders} \right] \tag{3.5}$$

where G is the amplitude of the motion-sensitizing gradients, $\overline{x}_{\Delta y}$ is the position of the center of the voxel and m_0 and m_1 are the gradient zeroth and first moments, respectively,

defined as

$$m_0 = \int_0^{TE} G(t)\,dt = 2Gd$$
$$\text{and} \tag{3.6}$$
$$m_1 = \int_0^{TE} G(t)\,t\,dt = 2Gd(d+T).$$

Therefore, m_1-induced attenuation of the iMSDE signal scales with strength, duration and separation of the motion-sensitizing gradients.

Diffusion Attenuation

The b-factor for the gradient waveform in Figure 3.3 is given by

$$\begin{aligned} \mathrm{b} &= (2\pi)^2 \int_0^{TE} k^2(t)\,dt \\ &= 2(GdT)^2\left(T + \frac{2}{3}d\right) \end{aligned} \tag{3.7}$$

where $k(t)$ is the k-space position achieved by the gradient waveform at time t. The diffusion attenuation of the iMSDE signal therefore scales with the strength, duration and separation of the motion-sensitizing gradients.

The iMSDE Signal

Given equations 3.2 through 3.7, the prepared signal for spins encoded with a gradient applied in the y direction observed after the 90°_{-x} tip-up pulse can described as

$$M_z^+ = M_0\, e^{-\mathrm{b}D} \cos\left(\gamma \sum_{n=0}^{\infty} m_n \alpha_0^n\right) \prod_{n=0}^{\infty} \int_{\Delta y} e^{i\gamma m_n \alpha^n(y)}\,dy \tag{3.8}$$

where n denotes the order of motion and α is defined as $\alpha \equiv d^n x/dt^n$. Therefore, the iMSDE signal is dependent on the effects of the gradient waveform contained in the b-factor and in the gradient moments as well as on the voxel size, the imaged material's diffusion coefficient and the order of motion experienced by the imaged spins.

3.2.1 Orthogonally Combined Motion- and Diffusion-Sensitized Driven Equilibrium (OC-MDSDE)

The iMSDE sequence has been shown to suppress the signal of fast-flowing blood [31, 61–63]. The problem of suppressing the signal from slow-flowing blood, however, requires that the first gradient moment m_1 be substantially increased, which in turn increases the sensitivity to motion and can lead to artifacts. Velocity compensation, namely m_1-nulling, will lead to a preparative sequence that is less sensitive to motion effects. The resulting diffusion-sensitized driven-equilibrium (DSDE) sequence is also capable of attenuating blood signal due to the significantly higher diffusion coefficient of blood compared to other tissues. In the particular case when the tissue of interest is anisotropic (*i.e.*, it has a preferential diffusion direction), diffusion-sensitizing gradients can be applied perpendicular to its principal diffusion axis in order to minimize its signal attenuation.

The orthogonally combined motion- and diffusion-sensitized driven equilibrium (OC-MDSDE) sequence developed in this work (Figure 3.4) was specifically designed for an anisotropic tissue of interest that has a preferential orientation perpendicular to the orientation of nearby blood flow.

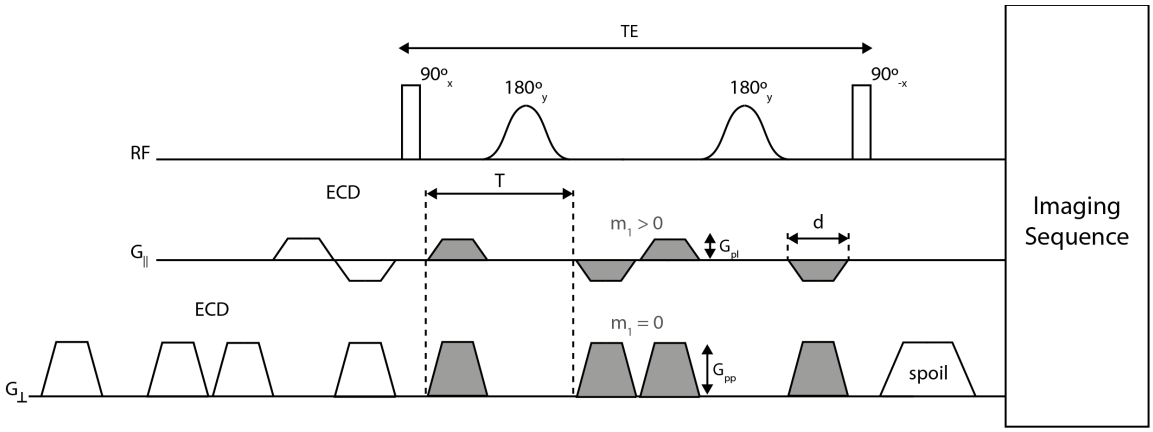

Figure 3.4: Orthogonally Combined Motion- and Diffusion-Sensitized Driven Equilibrium (OC-MDSDE) Preparation Sequence. The motion-sensitized ($m_1 > 0$) component uses low gradient strengths G_{pl} in the direction parallel to the preferential orientation of the tissue of interest. The diffusion-sensitized ($m_1 = 0$) component uses high gradient strengths G_{pp} perpendicular to the principal diffusion axis of the tissue of interest. Double-bipolar and quadruple-monopolar gradient pulses are used, respectively, before excitation for minimizing eddy currents.

3.3 Phase-Corrected Diffusion-Prepared 3D Turbo Spin Echo Imaging

3.3.1 Overview of Acquisition Methods for Diffusion Imaging in the Body

EPI Apporoach

Single-shot echo planar imaging (ss-EPI) has been the conventional imaging technique in diffusion MRI due to its encoding speed and its unmatched insensitivity to motion effects. A major problem in ss-EPI imaging is the low bandwidth in the phase encoding direction characteristic of the sequence's k-space sampling. The slow traversal of k-space in ss-EPI phase encoding leads to geometric distortions when imaging in the presence of B_0 inhomogeneities (*e.g.*, near air-tissue interfaces), which are prevalent in the body. Geometric distortions result in distorted anatomies as well as in signal-intensity modulations, or signal pile-ups, which interfere with the correct assessment of an anatomical feature as well as with diffusion quantification. For a given amount of B_0 inhomogeneity, geometric distortions in ss-EPI worsen with both echo spacing and with the FOV in the phase-encoding direction, making this method unsuitable in isotropic-resolution and large-FOV diffusion imaging. Moreover, low phase bandwidth in ss-EPI also leads to severe chemical shift artifacts in that direction. Quantitative diffusion imaging with ss-EPI in the body is therefore

particularly vulnerable to quantification errors in the presence of B_0 inhomogeneities and incomplete fat suppression.

Multishot acquisition in EPI can increase the bandwidth in the phase-encoding direction, alleviating –but not totally reducing, the chemical shift and susceptibility problems associated with ss-EPI. An overview of the development of EPI acquisition methods in context of diffusion imaging is presented below in Table 3.1.

Table 3.1: Overview of EPI-Based Acquisition in Context of DWI

Acquisition	Progress	Properties
Single-shot DW EPI	✔	Fast in low-resolution imaging
	✔	Insensitive to motion
	✖	Sensitive to gradient-induced distortions
	✖	Sensitive to ΔB_0-induced distortions
	✖	Sensitive to chemical-shift water/fat pixel displacements
2D Multishot DW EPI (*e.g.*, segmented EPI, segmented-readout EPI (sr-EPI), reduced-FOV (rFOV) EPI, simultaneous multislice (SMS) EPI, PROPELLER-EPI)	✔	Less sensitive to ΔB_0-induced distortions than single-shot
	✔	Corrects for motion using 2D navigation
	✔	*SMS and PROPELLER*: can achieve high isotropic resolutions rapidly and with increased SNR efficiency
	✖	Still sensitive to ΔB_0-induced distortions
	✖	Sensitive to gradient-induced distortions
	✖	Slower than single-shot
3D Multishot DW EPI (*e.g.*, 3D multislab EPI)	✔	Higher SNR efficiency than 2D
	✔	Improved through-plane resolution compared to 2D
	✔	Corrects for motion using 2D navigation
	✔	*Multislab*: similar acquisition time as single-shot
	✖	Still sensitive to ΔB_0-induced distortions
	✖	Sensitive to gradient-induced distortions

✔= Advantage/Improvement; ✖= Remaining problem

TSE Approach

Spin-echo-based imaging methods such as fast spin echo (FSE) or turbo spin echo (TSE) circumvent the susceptibility and chemical shift problems encountered in EPI-based imaging. In TSE imaging, the employment of multiple refocusing RF pulses during readout leads to lower SNR and longer scan times than EPI sequences. Particularly in TSE-based diffusion imaging, the usage of refocusing pulses imposes additional constraints on the magnetization used to generate a diffusion-weighted spin-echo signal, which need to be taken into account when designing the diffusion-weighted TSE sequence. Namely, TSE sequences require that the phase of the refocusing pulses used in each echo train matches the phase of the rotating spins creating magnetization (the Carr-Purcell-Meiboom-Gill (CPMG) condition [22]), which in general will not be met in the presence of any unknown phase accumulated during a preceding diffusion encoding module. TSE sequences used for diffusion imaging therefore require careful sequence modifications.

Multishot TSE has the advantage of achieving higher spatial resolutions than single-shot TSE. 3D TSE, always employing multishot spatial encoding, has the further advantage of achieving isotropic resolutions, providing an additional diagnostic perspective in certain applications of DWI and DTI in body imaging. Employing a multishot readout in TSE diffusion imaging, however, leads to the occurrence of intershot phase inconsistencies produced by random motion during diffusion encoding. As explained in Section 2.3, phase variations originating from motion will have additional unwanted effects on the diffusion-weighted TSE signal that require further modifications of the diffusion-sensitized multishot TSE sequence. Phase navigation directly measures any phase accrued during the diffusion-encoding period and is the only alternative in Cartesian diffusion imaging for the correction of motion-induced phase inconsistencies.

Various methods are available for adapting a TSE sequence for DWI, each of them posing advantages and disadvantages (see overview in Table 3.2 below). A method for adapting any TSE readout (single-shot, 2D/3D multishot) for diffusion imaging (with focus in body applications) was developed in this work and is described next in Sections 3.3.2 and 3.3.3.

Table 3.2: Overview of TSE-Based Acquisition in Context of DWI

Acquisition	Progress	Properties
Single-shot DW TSE (*e.g.*, displaced U-FLARE, SPLICE, phase-insensitive TSE, ss-MGOT, PROPELLER TSE)	✔	Fast in low-resolution imaging
	✔	Highly robust to ΔB_0-induced distortions
	✔	*PROPELLER TSE*: increased SNR, insensitive to in-plane motion, robust to through-plane motion, averages remaining phase inconsistencies
	✖	Cartesian sampling: in the presence of motion requires strict RF tailoring and the removal of non-CPMG echoes (various methods)
	✖	Removal of non-CPMG echoes results in signal loss and possibly in long echo spacings (*displaced U-FLARE, SPLICE*)
2D Multishot DW TSE (*e.g.*, multishot PROPELLER, multishot SPLICE PROPELLER, multishot TSE with POCMUSE reconstruction)	✔	Higher SNR compared to single-shot
	✔	Higher achievable resolution than single-shot
	✖	Slower than single-shot
	✖	Requires 2D navigation for the correction of motion-induced intershot phase inconsistencies
	✖	*POCMUSE*: Alleviation of motion-induced artifacts without navigation requires iterative phase correction reconstruction
3D Multishot DW TSE (*e.g.*, DPsti-TSE)	✔	Higher SNR efficiency compared to 2D
	✔	Improved through-plane resolution compared to 2D
	✖	Requires 2D or 3D navigation for the correction of intershot phase inconsistencies
	✖	*DPsti-TSE*: No phase correction leaves method sensitive to motion-induced intershot phase inconsistencies
	☑	*Phase-Corrected Diffusion-Prepared 3D TSE (present work)*: Uses 2D phase navigation at no additional SNR- or scan-time-cost to correct for motion-induced phase errors in thin-, single-slab isotropic-resolution 3D imaging

✔= Advantage/Improvement; ✖= Remaining problem; ☑= Presently implemented

3.3.2 Diffusion-Prepared 3D TSE

Diffusion sensitization in 3D TSE sequences can be attained by means of diffusion-sensitized driven equilibrium (DSDE) placed before the 3D TSE imaging acquisition. The PFGSE-based DSDE preparation used in the present work, which was adapted to specific needs of body DW 3D TSE imaging, is shown in Figure 3.3.2. DSDE RF consists on signal excitation, refocusing and restoration and, in the absence of gradients, results in a purely T_2-weighted signal. A modified four-segment B_1-insensitive rotation (BIR-4) RF configuration is used for improved robustness to B_0 and B_1 inhomogeneities commonly encountered in body imaging [64–66]. Diffusion encoding in the present DSDE sequence uses a PFGSE design to minimize the preparation duration TE_{prep}. Driven-equilibrium-based diffusion encoding is used to satisfy the CPMG condition in TSE imaging, which, owing to the restoration RF pulse, will be satisfied even in the presence of additional phase terms in the prepared signal.

Phase terms additional to the desired diffusion-encoding phase can arise from eddy currents caused by switching diffusion gradients and from motion of the imaged object. Eddy-current- and motion-induced phase terms lead to signal magnitude modulations and need to be accounted for.

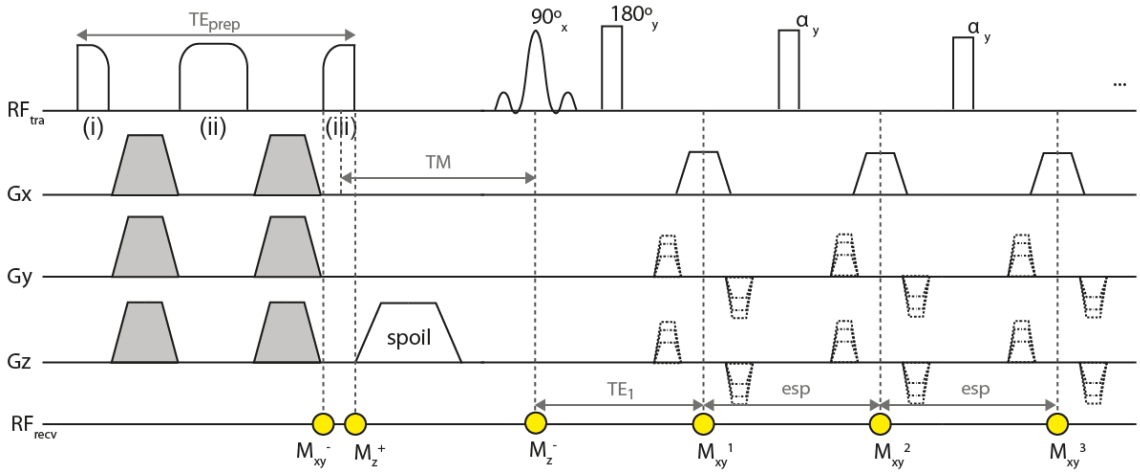

Figure 3.5: Diffusion-Prepared 3D TSE. The adiabatic diffusion-sensitized driven equilibrium (DSDE) preparation consists of a modified BIR-4 pulse for minimizing transmit B_1 effects, where (i) indicates excitation, (ii) refocusing and (iii) restoration of signal. Diffusion-sensitizing gradients (gray) arranged in a PFGSE configuration are placed symmetrically around the refocusing RF segment for minimizing the preparation duration TE_{prep}. Restoration of prepared signal satisfies the CPMG condition of the TSE imaging sequence. A spoiling gradient after signal restoration removes residual transverse magnetization before the 3D TSE imaging acquisition.

3.3.3 Correction of Phase Errors in Diffusion-Prepared 3D TSE

Signal Magnitude Modulation

Van et al. [67] showed that the magnetization of a single voxel after diffusion encoding before (M_{xy}^{-}) and after (M_{xy}^{+}) signal restoration, or signal tip-up, (see Figure 3.5) is given

by

$$\begin{aligned} M_{xy}^{-} &= M_{prep}\, \mathrm{e}^{i\pi/2} \mathrm{e}^{i\phi}, \\ M_{z}^{+} &= M_{prep} \cos(\phi), \end{aligned} \tag{3.9}$$

where M_{prep} is the magnitude of the prepared magnetization including T_2 decay and diffusion attenuation. The constant phase term of $\pi/2$ is a consequence of TSE excitation along the x-axis and refocusing along the y-axis and the phase term ϕ is any eddy-current and/or motion-induced phase generated during the diffusion encoding period.

After T_1 relaxation in the time between the restoration RF pulse of the diffusion preparation and the excitation pulse of the TSE imaging acquisition, denoted TM, the prepared (longitudinal) magnetization is expressed as

$$M_{z}^{-} = M_{prep} \cos(\phi)\, \mathrm{e}^{-TM/T_1} + M_0\, (1 - \mathrm{e}^{TM/T_1}), \tag{3.10}$$

where M_0 is the equilibrium magnetization of the spins in the voxel. For any flip angle of the refocusing RF pulses, the transverse magnetization at the first TSE echo, M_{xy}^{1}, and at subsequent echoes, M_{xy}^{n}, can be expressed as

$$\begin{aligned} M_{xy}^{1} &= \mathrm{e}^{-TE_1/T_2}\, M_{z}^{-}\, \mathrm{e}^{i\pi/2} \\ M_{xy}^{n} &= r_n\, M_{z}^{-}\, \mathrm{e}^{i\pi/2}, \end{aligned} \tag{3.11}$$

where TE_1 is the first echo time and the prefactor r_n encompasses the mixed T_1 and T_2 relaxation at the time $T_1 + n\,\mathrm{esp}$ of the n*th* echo. In the special case when T_1 relaxation is negligible during the time TM, that is, when $TM << T_1$, the magnetization of the n*th* echo takes on the following form:

$$\begin{aligned} M_{xy}^{n} &= r_n\, \mathrm{e}^{u\pi/2}\, M_{prep} \cos(\phi)\, \mathrm{e}^{-TM/T_1} \\ &= \begin{cases} r_n\, M_{prep}\, \mathrm{e}^{-TM/T_1}\, |cos(\phi)|\, \mathrm{e}^{i\pi/2}, & \text{if } -\frac{\pi}{2} < \phi < \frac{\pi}{2} \\ r_n\, M_{prep}\, \mathrm{e}^{-TM/T_1}\, |cos(\phi)|\, \mathrm{e}^{i3\pi/2}, & \text{otherwise.} \end{cases} \end{aligned} \tag{3.12}$$

Equation 3.12 implies that, in the case of negligible T_1 relaxation between signal tip-up and TSE excitation, the presence of any phase error ϕ in the diffusion-weighted signal will cause the magnitude of the DW TSE signal in a voxel to modulate as a function of the phase error and the signal phase to toggle between $\pi/2$ and $3\pi/2$ depending on the value taken by ϕ.

Signal Magnitude Stabilization

Magnitude modulation induced by phase errors in DW single- and multishot TSE can be lessened with the method proposed by Alsop in 1997 [68] consisting of the application of dephasing and rephasing gradients, referred to here as *magnitude stabilizers*, at the time of echo formation in the diffusion preparation as well as around all echoes formed in the TSE acquisition (Figure 3.6). The magnitude stabilizer placed before the restoration of the diffusion-weighted signal creates a uniform phase distribution within each voxel, regardless of the signal phase, but at the cost of 50% of the signal. The magnitude stabilizer pairs in the TSE acquisition are necessary for re-establishing correct echo formation. With the addition of magnitude stabilizers, the prepared magnetization before and after signal

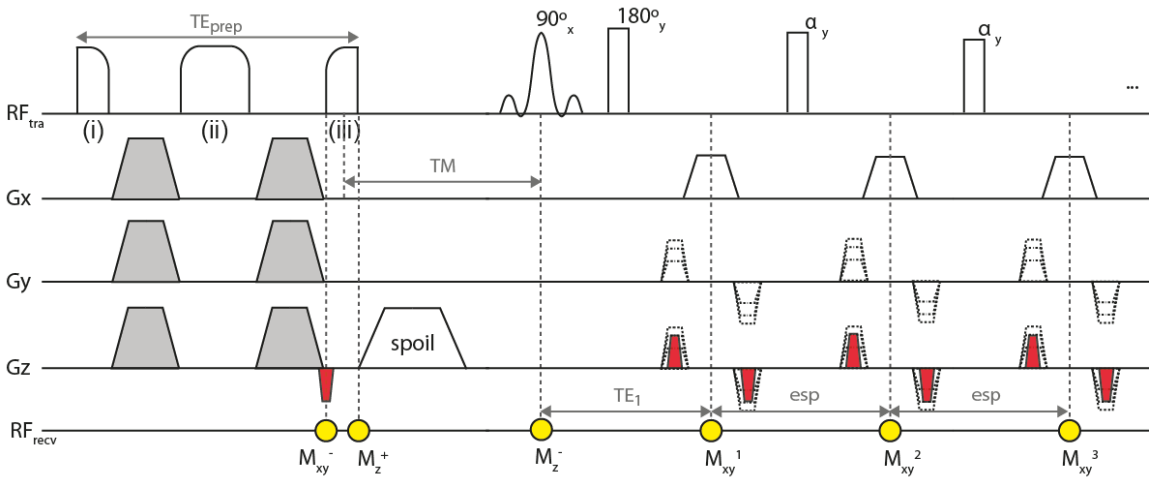

Figure 3.6: Diffusion-Prepared 3D TSE with Magnitude Stabilizers. A magnitude stabilizing gradient (red) is placed before signal restoration and magnitude stabilizing gradient pairs are placed around each TSE echo in the TSE imaging acquisition.

restoration, M_{xy}^{-} and M_{xy}^{+} respectively, given without magnitude stabilizers in Equation 3.9, now becomes

$$\begin{aligned} M_{xy}^{-} &= M_{prep}\, e^{i\pi/2} e^{i\phi} \frac{1}{N} \sum_{v \in \text{voxel}} e^{-i\Theta_v}, \\ M_{z}^{+} &= M_{prep} \frac{1}{N} \sum_{v \in \text{voxel}} \cos(\phi - \Theta_v), \end{aligned} \tag{3.13}$$

where Θ_v is the phase added by the magnitude stabilizer to the v*th* spin within the voxel and N is the total number of spins in the voxel. The prepared magnetization immediately before TSE excitation, described in Equation 3.10 without magnitude stabilizers, now becomes

$$M_{z}^{-} = M_0 (1 - e^{TM/T_1}) + M_{prep}\, e^{-TM/T_1} \frac{1}{N} \sum_{v \in \text{voxel}} \cos(\phi - \Theta_v). \tag{3.14}$$

Thus, if the magnitude stabilizers are designed so that they produce complete dephasing within a voxel (i.e., $\sum_{v \in \text{voxel}} e^{i\Theta_v} = 0$), the transverse magnetization of the first and subsequent TSE echoes, for refocusing pulses with any flip angle, will be given by

$$\begin{aligned} M_{xy}^{1} &= \frac{1}{2} M_{prep}\, e^{-TM/T_1}\, e^{-TE_1/T_2}\, e^{i(\phi+\pi/2)} \\ M_{xy}^{n} &= r_n \left[\frac{1}{2} M_{prep}\, e^{-TM/T_1}\, e^{[TE_1 + (n-1)\, esp]/T_2}\, e^{i(\phi+\pi/2)} \right]. \end{aligned} \tag{3.15}$$

Equation 3.15 implies that, for a given phase error ϕ with intra-voxel uniformity that is added to the prepared signal during the diffusion encoding period, the inclusion of magnitude stabilizers in the presented diffusion-prepared TSE sequence will result in: 1) a DW TSE signal *magnitude* that does not vary with ϕ and 2) a DW TSE signal *phase* that varies linearly with ϕ.

Phase Correction

Given that DW 3D TSE always uses a multishot acquisition, the remaining variation of the signal phase with phase errors requires phase correction and therefore phase navigation.

The phase navigation technique implemented for the presented diffusion-prepared 3D TSE sequence is illustrated in Figure 3.7. Navigator echoes, acquired prior to the imaging echoes and phase-encoded in the k_y direction, capture motion-induced phase introduced during the preceding diffusion preparation for each acquired shot. Since the presented method effectively measures a 2D navigator per shot, the method requires that phase errors in the second phase encoding direction (k_z) are negligible.

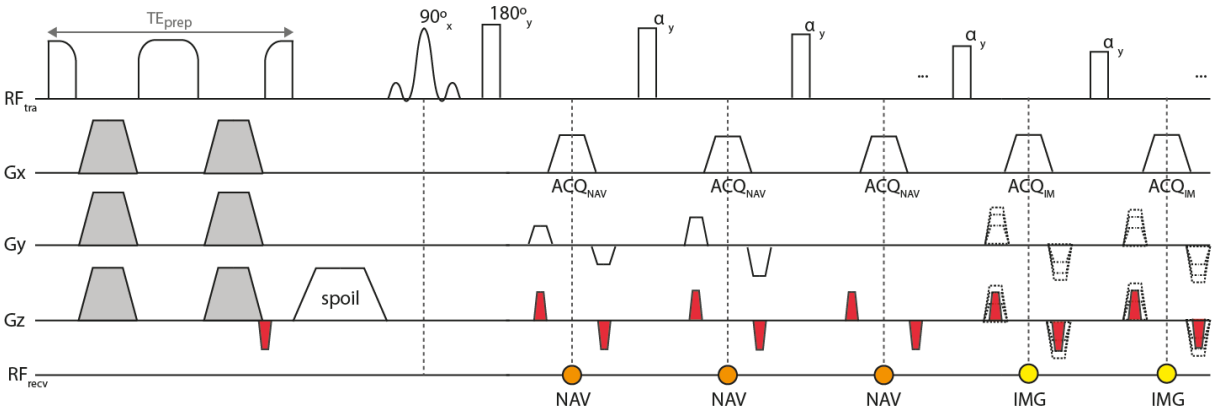

Figure 3.7: Phase Navigated Diffusion-Prepared 3D TSE. Navigator echoes are acquired during the pseudo steady state (PSS) stage of 3D TSE and are phase-encoded along the k_y direction only. The imaging sequence acquires one full k_z plane in each shot.

Phase correction of DW 3D TSE data using navigator data is carried out during image reconstruction. For each shot n and diffusion acquisition j, 2D-reconstructed low-resolution T_2-weighted navigator k-space data $\mathrm{ref}^{n}_{lr}(x, y, kz = 0)$ and 2D-reconstructed low-resolution diffusion-weighted navigator k-space data $\mathrm{nav}^{j,n}_{lr}(x, y, kz = 0)$ are used to estimate the 2D phase error $\phi^{j,n}(x, y)$ as

$$\phi^{j,n}(x, y) = \angle[\mathrm{nav}^{j,n}_{lr}(x, y, kz = 0)/\mathrm{ref}^{n}_{lr}(x, y, kz = 0)]. \tag{3.16}$$

Phase correction of 2D-reconstructed imaging data $\mathrm{im}^{j,n}(x, y, kz)$ is then carried out using the estimated phase error as

$$\mathrm{im}^{j,n}_{\mathrm{corr}}(x, y, kz) = \mathrm{im}^{j,n}(x, y, kz)\, \mathrm{e}^{-i\phi^{j,n}(x,y)}. \tag{3.17}$$

1D reconstruction along kz, equivalently across all shots, results in the final phase-corrected imaging data $\mathrm{im}_{\mathrm{corr}}(x, y, z)$.

Compliance with Ethical Standards

All investigations performed in studies involving human participants were in accordance with the ethical standards of the institutional and/or national research committee and with the 1964 Helsinki declaration and its later amendments or comparable ethical standards. Informed consent was obtained from all individual participants included in the studies.

Journal Publications

5.1 Journal Publication I: Imaging of the Lumbar Plexus: Optimized Refocusing Flip Angle Train Design for 3D TSE

The publication entitled *Imaging of the Lumbar Plexus: Optimized Refocusing Flip Angle Train Design for 3D TSE* was published in the Journal of Magnetic Resonance in Medicine (ISSN: 1522-2586). The manuscript was authored by Barbara Cervantes, Jan S. Bauer, Felix Zibold, Hendrik Kooijman, Marcus Settles, Axel Haase, Ernst J. Rummeny, Klaus Wörtler, and Dimitrios C. Karampinos.

Abstract

Purpose

To study the effects of refocusing angle modulation with 3D turbo spin echo (TSE) on signal and sharpness ofsmall oblique nerves embedded in muscle and suppressed fat in the lumbar plexus.

Materials and Methods

Flip angle trains were generated with extended phase graphs (EPG) for a sequence parameter subspace. Signal loss and width broadening were simulated for a single-pixel nerve embedded in muscle and suppressed fat to prescribe a flip angle modulation that gives the best compromise between signal and sharpness of small nerves. Two flip angle trains were defined based on the simulations of small embedded nerves: design denoted A, predicting maximum global signal, and design denoted B, predicting maximum signal for minimum width broadening. In vivo data of the lumbar plexus in 10 healthy volunteers was acquired at 3.0T with 3D TSE employing flip angle trains A and B. Quantitative and qualitative analyses of the acquired data were made to assess changes in width and signal intensity.

Results

Changing flip angle modulation from A to B resulted in: 1) average signal losses of 23% in (larger) L5 nerves and 9% in (smaller) L3 nerves; 2) average width reductions of 4% in L5 nerves and of 16% in L3 nerves; and 3) statistically significant sharpness improvement (P = 0.005) in L3 nerves.

Conclusion

An optimized flip angle train in 3D TSE imaging of the lumbar plexus considering geometry-specific blurring effects from both the nerve and the surrounding tissue can improve the delineation of small nerves.

Author Contributions

(i) The first author alone: implemented the library of tools used to perform all numerical simulations (MATLAB and Statistics Toolbox Release 2014b, The MathWorks, Inc., Natick, Massachusetts, United States); performed all numerical simulations; performed all experiments (in vivo magnetic resonance measurements); and performed the quantitative data analysis. (ii) With the help and consultation of the coauthors, the first author: designed the experiment; performed the statistical data analysis; and wrote the manuscript.

Imaging of the Lumbar Plexus: Optimized Refocusing Flip Angle Train Design for 3D TSE

Barbara Cervantes, MS,[1]* Jan S. Bauer, MD,[2] Felix Zibold, MD,[2]
Hendrik Kooijman, PhD,[3] Marcus Settles, PhD,[1] Axel Haase, PhD,[4]
Ernst J. Rummeny, MD,[1] Klaus Wörtler, MD,[1] and Dimitrios C. Karampinos, PhD[1]

Purpose: To study the effects of refocusing angle modulation with 3D turbo spin echo (TSE) on signal and sharpness of small oblique nerves embedded in muscle and suppressed fat in the lumbar plexus.
Materials and Methods: Flip angle trains were generated with extended phase graphs (EPG) for a sequence parameter subspace. Signal loss and width broadening were simulated for a single-pixel nerve embedded in muscle and suppressed fat to prescribe a flip angle modulation that gives the best compromise between signal and sharpness of small nerves. Two flip angle trains were defined based on the simulations of small embedded nerves: design denoted A, predicting maximum global signal, and design denoted B, predicting maximum signal for minimum width broadening. In vivo data of the lumbar plexus in 10 healthy volunteers was acquired at 3.0T with 3D TSE employing flip angle trains A and B. Quantitative and qualitative analyses of the acquired data were made to assess changes in width and signal intensity.
Results: Changing flip angle modulation from A to B resulted in: 1) average signal losses of 23% in (larger) L5 nerves and 9% in (smaller) L3 nerves; 2) average width reductions of 4% in L5 nerves and of 16% in L3 nerves; and 3) statistically significant sharpness improvement ($P = 0.005$) in L3 nerves.
Conclusion: An optimized flip angle train in 3D TSE imaging of the lumbar plexus considering geometry-specific blurring effects from both the nerve and the surrounding tissue can improve the delineation of small nerves.
J. MAGN. RESON. IMAGING 2016;43:789–799.

Magnetic Resonance Imaging (MRI) of proximal and distal nerves in the body, often referred to as magnetic resonance neurography (MRN), has become an increasingly used diagnostic tool in the assessment of nerve lesions.[1] Isotropic, high-resolution 3D imaging has been shown to provide high accuracy in the evaluation of nerves with high obliqueness due to the feasibility of curved and multiplanar reconstructions and volume reformatting.[2] Specifically, 3D spin echo imaging based on rapid acquisition with relaxation enhancement (RARE), also known as 3D turbo spin echo (TSE) or 3D fast spin echo (FSE),[3] has been emerging as a reliable and robust method for achieving isotropic, high-resolution T_2-weighted imaging of nerves and is particularly advantageous in regions with high obliqueness, such as the lumbar and brachial plexuses.[4,5] This method, however, is limited by the trade-off between the spatial resolution necessary to delineate small nerves and the need for sufficient signal needed to visualize fine nerve branches.

3D TSE sequences rely on the design of a refocusing flip angle train that balances relaxation-induced signal loss and blurring effects for a specific tissue.[6–9] The flip angles assigned to a refocusing train determine the signal evolution along the echo train and therefore the signal intensities and blurring observed for all the imaged tissues.[10] The extended phase graph (EPG) formalism is a tool commonly used to

View this article online at wileyonlinelibrary.com. DOI: 10.1002/jmri.25076

Received Apr 24, 2015, and in revised form Sep 28, 2015. Accepted for publication Sep 29, 2015.

*Address reprint requests to: B.C., Department of Diagnostic and Interventional Radiology, Klinikum rechts der Isar, Technische Universität München, Ismaninger Str. 22, 81675 Munich, Germany. E-mail: b.cervantes@tum.de

From the [1]Department of Diagnostic and Interventional Radiology, Technische Universität München, Munich, Germany; [2]Department of Neuroradiology, Klinikum rechts der Isar, Technische Universität München, Munich, Germany; [3]Philips Healthcare, Hamburg, Germany; and [4]Zentralinstitut für Medizintechnik, Technische Universität München, Garching, Germany

assess the signal response of pulse sequences with long flip angle trains due to its capability to quantize the magnetization along all spin echo and stimulated echo pathways.[11] Further, if relaxation parameters are taken into account, a tissue-specific characterization of the signal is possible using the EPG method. Beyond the assessment of the echo intensities resulting from a given sequence, flip angles for all refocusing pulses along the train can be computed in order to meet user-defined signal requirements by means of finding the inverse solution to the EPG problem.[6] Therefore, EPG has been extensively used in 3D TSE imaging to design tissue-specific flip angle trains that maintain a signal plateau for long echo trains and thus attain optimal signal characteristics for a particular tissue.[10] Flip angle modulation has been used to shape the signal response in TSE (or FSE) sequences with long refocusing trains in a wide range of applications using different imaging systems.[12–15] Particularly in nerve imaging, flip angle modulation in 3D TSE has been shown to yield satisfactory results in various anatomical regions.[16,17] 3D TSE imaging of nerves, however, has been based on the traditional design of flip angle trains balancing the relaxation-induced signal loss and blurring effects without any geometry considerations and taking into account signal contributions from only one reference tissue.

A given flip angle train will generate distinct signal responses for distinct tissues, depending on the tissues' relaxation parameters as well as on their local geometry. Particularly at the interface between two tissues, the blurring mechanisms of both tissues will interact and, depending on the local geometry, will determine the effective appearance at the interface. While the effect of blurring in imaging of large objects is a loss of edge sharpness, the effect of blurring in imaging of small objects is an additional loss of signal intensity, which can jeopardize the ability to detect such small structures.[18]

Most nerves are small objects embedded most frequently within fat or skeletal muscle. While most nerves are directly surrounded by fat, the smaller nerve branches, which are the most difficult to delineate, tend to penetrate muscle. The nerve signal intensity can therefore be sensitive to the blurring effects of the enveloping tissue. The loss of small objects embedded in another tissue has been addressed in 2D TSE imaging of the human brain,[19] but no experimental evaluation in nerve imaging is known to have been performed. Moreover, blurring at the nerve–muscle interface can reduce the nerve signal and limit the ability to detect fine nerve structures. Therefore, proper assessment of blurring effects in nerve imaging requires additional consideration of the nerve geometry and of the enveloping muscle.

The purpose of the present study was to investigate the effects of refocusing flip angle modulation on signal loss and blurring of small nerves embedded in muscle with 3D TSE in a region with high obliqueness (ie, the lumbar plexus) and to develop an optimized flip angle train that balances the needs of signal and sharpness necessary for the adequate delineation of thin nerve branches.

MATERIALS AND METHODS

Numerical Simulations

FLIP ANGLE TRAIN ESTIMATION USING EXTENDED PHASE GRAPHS. Flip angle trains were produced using the EPG formulation considering the T_1 and T_2 relaxation parameters of nerve in order to obtain an optimized signal response for that tissue. In order to avoid the occurrence of signal oscillations from echo to echo,[20–22] a temporary steady state (referred to as a pseudosteady-state [PSS]) for the signal was reached by means of a specific selection of flip angles for the initial refocusing pulses. PSS resulted in the signal approaching a certain intensity level after the same number of initial echoes and remaining at that level for subsequent echoes. The duration for which the signal remained constant is referred to as the signal plateau length. Flip angles after the PSS were allowed to vary freely from an internally calculated minimum value to two user-defined maximum values. After reaching the first maximum flip angle, flip angles were increased at a constant rate until the second maximum flip angle value at the end of the train.

The parameters input into the flip angle train estimation algorithm were: a number of start-up echoes that are not acquired, the total number of acquired echoes (echo train length), the two maximum flip angles, the echo spacing, and the signal plateau length. The calculation of the flip angles along the train relied on the estimation of the internally computed minimum flip angle. The minimum flip angle was determined iteratively to satisfy the given conditions of reaching PSS and maintaining a constant signal for the signal plateau length. Once this minimum flip angle was determined, the PSS flip angles were computed by means of an asymptotic transition from an initial flip angle of 180° to the minimum flip angle, as described in the literature.[6,10] Once the PSS flip angles were established, the corresponding PSS signal and signal plateau were computed using the forward EPG formulation. The computed PSS signal and signal plateau were then inserted as an input into the inverse EPG algorithm[6] in order to determine the entire flip angle train. The resulting tissue-specific flip angle train thus consisted of a rapidly decreasing PSS sweep followed by a free modulation and by a final linear increase. Finally, the resulting flip angle train was inserted into the forward EPG formulation to compute the complete modulation transfer function (MTF) for the employed reference tissue.

FLIP ANGLE TRAIN OPTIMIZATION. Flip angle trains were computed for nerve tissue and corresponding MTFs were simulated for both nerve and muscle tissues for a parameter subspace of varying echo spacing and signal plateau length. The signal plateau length was normalized to the full echo train length (this normalized value, from this point on, will be referred to as the relative plateau length). The following parameters remained constant in the simulations: maximum flip angles (defining the range of flip angles within which modulation at the end of the echo train was kept linear) = [100°, 125°], six start-up echoes, echo train length = 150, relaxation times T_1 = 1010 msec and T_2 = 90 msec for nerve tissue

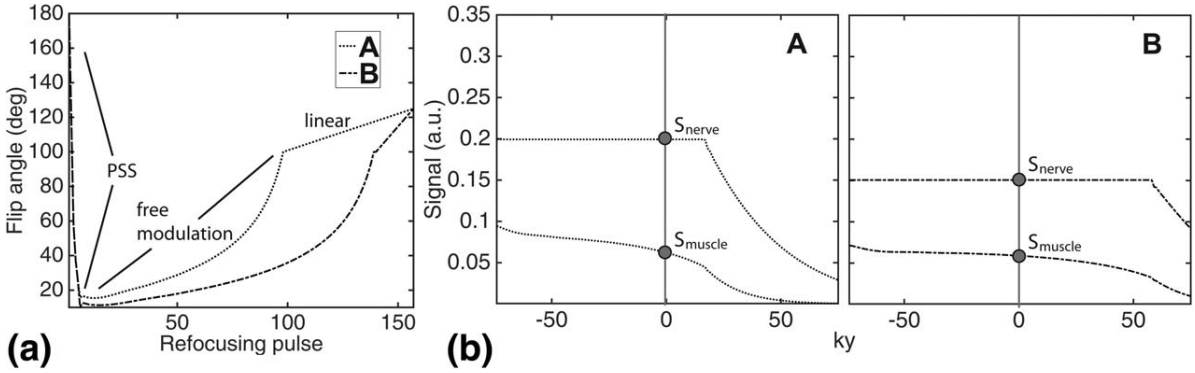

FIGURE 1: (a) Flip angle trains A and B and (b) corresponding modulation transfer functions (MTFs) of nerve and muscle, generated using extended phase graphs (EPG). Both flip angle trains were designed according to the relaxation properties of nerve, yielding a constant signal plateau for that tissue but not for muscle or other nonreference tissues. Decaying signal leads to *k*-space filtering of high frequencies, resulting in blurring. Flip angle train A corresponds to quickly varying flip angles yielding higher signal but larger blurring of both tissues. Flip angle train B illustrates a more slowly varying modulation resulting in a compromise between signal loss and blurring. In (b), echo intensities before establishing pseudosteady state (PSS) are not shown.

and $T_1 = 1420$ msec and $T_2 = 39$ msec for muscle. Given the limitation on T_1 relaxometry literature in nerve imaging in humans, the T_1 value used for nerve tissue was adapted from reported values corresponding to white matter[23,24] and the T_2 relaxation time for this tissue was derived from recent relaxometry studies of human nerves.[25–27] The relaxation times of muscle employed in the numerical simulations were chosen based on previously reported relaxometry results considering T_2 dependencies on subject age, body type, and health status.[28–30]

Figure 1a shows flip angle trains designed for two specified signal responses of nerve (denoted A and B), where the above description of flip angle train estimation using extended phase graphs is illustrated. Figure 1b shows the desired signal response of nerve as well as the signal response of muscle predicted for each flip angle train design A and B. MTFs A and B describe the signal responses of nerve and muscle simulated for the 3D TSE sequence with a constant echo spacing of 4 msec and the sequence parameters listed above. The MTF of nerve in A was designed to have a signal plateau length of 60% of the total echo train length and that in B of 85%. Signal decay at high ky values corresponds to *k*-space filtering of high frequencies and results in blurring of the image.

In order to assess the effect of tissue geometry on signal response, in the case of nerve embedded in muscle, the signal intensity of nerve was evaluated with the following simulations: a) nerve of infinite width; b) nerve of finite width embedded in muscle; and c) nerve of unit width embedded in muscle (top diagrams in Fig. 2, shown in respective order). Signal values for infinitely

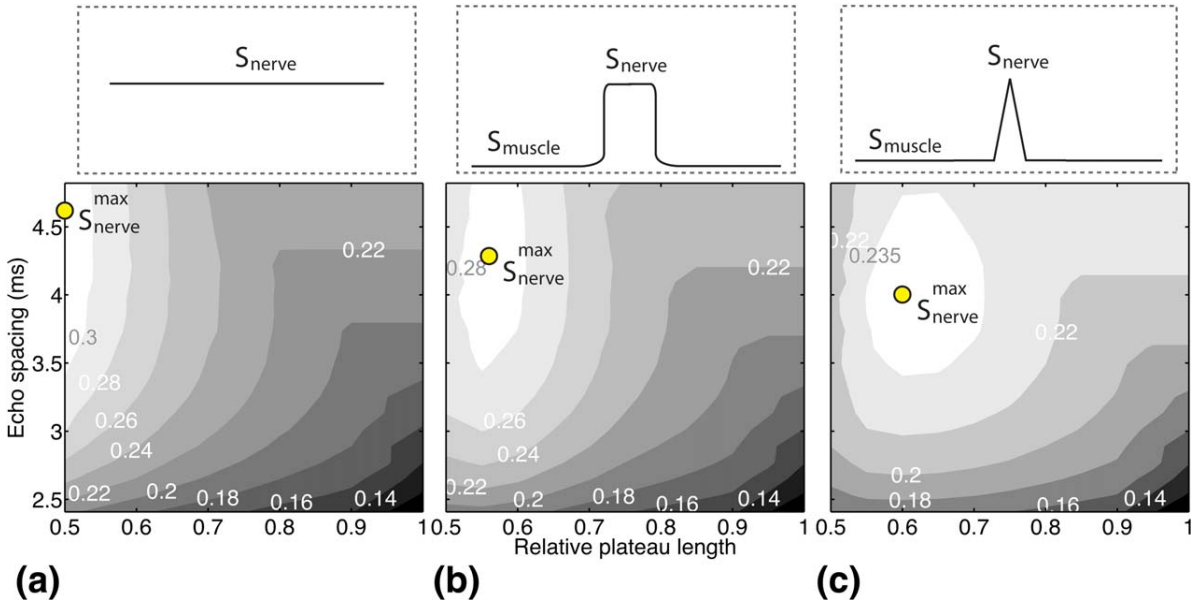

FIGURE 2: Effect of tissue geometry on signal response simulated for (a) the standard case of nerve as a single reference tissue, (b) a finite nerve feature embedded in muscle, and (c) a single-pixel nerve feature embedded in muscle. The nerve signal contour is plotted as a function of the echo spacing and the relative plateau length and the maximum nerve signal is shown for the three geometry cases. A different flip angle train design is necessary to achieve maximum signal of nerve depending on the specific geometry.

wide nerve (case a) were obtained directly from the MTFs associated with the flip angle trains computed in the given parameter subspace. For the other two cases (b and c), normalized profiles of nerves having finite and unit widths embedded in a large region of muscle were simulated. Effectively blurred nerve profiles were obtained by 1) Fourier-transforming the spatial profile for each tissue (muscle and nerve); 2) separately filtering the tissue *k*-space profile with the corresponding MTF; 3) inverse Fourier-transforming the two filtered tissue *k*-space profiles; and 4) adding the blurred spatial profiles from the two tissues. Signal intensities of the effectively blurred nerve profiles were measured and compared for the three geometries.

In order to evaluate the trade-off between signal intensity and width broadening for small nerves, full-width at half-maximum (FWHM) values of nerve profiles simulated having initially unit width were measured and the deviations from unit width $|b_{min}\text{-}b|/b_{min}$ and from maximum signal intensity $|S_{max}\text{-}S|/S_{max}$ were calculated for all flip angle trains within the given parameter space. In order to address the combined and coupled effect of nerve signal loss and width broadening, the joint deviation $|S_{max}\text{-}S|/S_{max} + |b_{min}\text{-}b|/b_{min}$ was computed for the given parameter space. For the case of nerve embedded in muscle, the flip angle train that generates the minimum deviation from the maximum signal $[|S_{max}\text{-}S|/S_{max}]_{min}$, denoted as flip angle train A, was determined. The flip angle train that generates the minimum joint deviation from the maximum signal and the minimum width $[|S_{max}\text{-}S|/S_{max} + |b_{min}\text{-}b|/b_{min}]_{min}$, denoted as flip angle train B, was also determined.

To address the case of nerve embedded in fat with suppressed signal, signal intensity and width broadening effects were inspected for a simulated unit-width nerve surrounded by tissue with zero signal (all presented 3D TSE sequences used fat suppression). Flip angle trains that minimize $|S_{max}\text{-}S|/S_{max}$ and $|S_{max}\text{-}S|/S_{max} + |b_{min}\text{-}b|/b_{min}$ in this case, denoted A* and B*, respectively, were calculated and compared to the case of nerve surrounded by muscle.

Subjects

Ten healthy volunteers (mean age 28.6 ± 4.0 years; eight males, two females) participated in the study. The study was approved by the local Institutional Review Board and conducted in accordance with the Committee for Human Research. All subjects gave written informed consent prior to their participation in the study.

In Vivo *Measurements*

Coronal images of the lumbar plexus of the subjects were acquired using a 3T whole-body Philips scanner (Philips Ingenia, Best, the Netherlands) with a 16-channel torso coil and the built-in-table 12-channel posterior coil. The subjects were positioned supine and the coil was centered at the pelvis in order to fully cover the lumbar spine. Surveys were acquired in all coronal, sagittal, and transversal planes and the imaging volume was further aligned to the spinal cord and to the axis of the nerves on the transversal plane. T_2-weighted 3D TSE was carried out using two different flip angle train configurations corresponding to MTFs having relative plateau lengths equal to 0.6 and 0.85 (corresponding to flip angle trains A and B). Echo spacing = 4 msec, maximum flip angles = [100°, 125°], six start-up echoes, field of view (FOV) = 400 × 400 × 80 mm^3, acquisition voxel = 1.25 × 1.25 × 1.4 mm^3, reconstruction voxel = 0.63 × 0.63 × 0.7 mm^3, TR/TE = 2000/330 msec, echo train length = 150, duration of each 3D TSE scan = 4 minutes 26 seconds, reference tissue relaxation times T_1 = 1010 msec and T_2 = 90 msec, parallel imaging with reduction factor R = 2.5, no partial Fourier, fat suppression using spectral inversion recovery. Similar to current work in MR neurography with 3D TSE,[16,31] a T_2 preparation module with two refocusing pulses and with four bipolar velocity encoding gradients was placed before readout to increase nerve–muscle contrast and to reduce vessel signal. The module was employed with TE_{prep} = 29 msec and encoding velocities = 1 cm/s along all three gradient axes.

Data Analysis

To address the different scaling of the acquired images for the different experimental settings, signal intensities were normalized to the measured signal from a reference muscle region next to the femoral head (region less prone to motion artifacts). The signal intensities of muscle used for normalization were concurrently normalized to the EPG-computed muscle signal, to account for the overall muscle signal variations expected between flip angle trains. Intensity profiles from five adjacent locations along each of the L5 and L3 lumbar nerves were obtained from selected source images of each dataset corresponding to each subject. Signal intensity and width, derived from the amplitude and FWHM of each intensity profile, respectively, were measured for all five locations along each nerve and mean and standard deviation values were computed. All experimental intensity profiles were first linearly interpolated to give a 9-fold number of data points and thus increase accuracy, and subsequently smoothed using a digital filter with a window size of five points to reduce the effect of noise in the measurements. Normalized deviations of signal intensity and width broadening between flip angle trains A and B were calculated to evaluate the trade-off between the two designs.

Qualitative Assessments

Image quality was evaluated by means of a five-point visual grading of the source images acquired using flip angle trains A and B by two board certified radiologists with 14 (J.S.B.) and 5 (F.Z.) years of experience. Evaluations from each reader were performed blindly and independently from one another in order to assess interreader reproducibility. Additionally, the first reader had two separate evaluations in order to assess intrareader reproducibility. The evaluated criteria consisted of 1) the sharpness of the L3 femoral nerve within the quadratus lumborum muscle; 2) the ability to resolve the fascicles within the L3 nerve root immediately after the ganglion; and 3) the ability to resolve the fascicles within the L5 nerve root. In the five-point grading scale, a grade of 1 corresponded to perfect delineation, 2 to good delineation but with noticeable blurring, 3 to delineation acceptable for clinical evaluation, 4 to delineation insufficient for clinical evaluation, and 5 to no distinction from the background tissue.

Statistical Testing

The average grades corresponding to flip angle trains A and B were statistically compared for each criterion using a paired *t*-test with a significance level of 5%. Inter- and intrareader agreement was

determined by measuring the intraclass correlation (ICC) coefficients for the two flip angle train designs for each criterion. The ICC model was based on a two-way random comparison of absolute agreement type and the coefficients were computed with a significance level of 5%.

RESULTS

Numerical Simulations

Flip angle trains and the corresponding MTFs of nerve and muscle in Fig. 1 illustrate the relationship between the tissue-specific flip angle modulation designs A and B and the expected signal response of both tissues in each case. Flip angle train A exhibits a faster modulation of refocusing angles, sweeping from the minimum angle (reached after PSS stabilization) to the first maximum angle of 100° within the first hundred refocusing pulses. Flip angle train B, in contrast, reaches the same first maximum angle later on in the pulse train, translating to a slower flip angle modulation. For the given relaxation parameters of nerve, the quicker modulation in design A results in a higher signal level and more severe *k*-space filtering (decaying tail of the MTF) for this tissue. The slower modulation employed in train B results in a more effective reduction of T_2 decay and consequently in reduced *k*-space filtering in the associated MTF of nerve.

Simulations shown in Fig. 2 illustrate how the expected response of nerve signal is different for different nerve geometries when identical flip angle trains are employed in the acquisition with 3D TSE. The shown signal response of nerve, derived from the selected subspace of EPG-generated MTFs, expresses that the maximum signal of nerve is reached with different flip angle trains depending on the defined tissue geometry. In the case considering nerve as a single reference tissue and in which no geometry is defined (Fig. 2a), maximum nerve signal is achieved with a refocusing angle train employing an echo spacing of 4.6 msec and with the corresponding MTF having the minimum possible relative signal plateau length, equal to 50% of the total echo train length. Once surrounding muscle is introduced and the nerve structure has a finite width (Fig. 2b), the maximum nerve signal requires an experimental setting including an echo spacing of 4.2 msec and a relative signal plateau length of 55%. Moreover, when the width of the nerve feature is reduced to unit length (Fig. 2c), a flip angle train with an echo spacing of 4.0 msec and an associated relative signal plateau length of 60% is necessary to achieve maximum nerve signal. Signal of nerve is predicted to decrease as the size of the nerve decreases and becomes equal to 75% of the maximum EPG signal in the case of a single-pixel nerve embedded in muscle.

The selection of the optimal flip angle train was based on the simulations of a single-pixel nerve embedded in muscle by means of the minimization of the coupled deviation from maximum signal and from minimum width broadening. Figure 3a illustrates the deviation from minimum width broadening $|b_{min}\text{-}b|/b_{min}$ for a single-pixel nerve embedded in muscle: width broadening decreases with increasing relative signal plateau length and is restored to the case of no blurring at echo spacing values smaller than 4.0 msec and plateau lengths larger than 85% of the total echo train length. Figure 3b plots the deviation from the maximum signal intensity $|S_{max}\text{-}S|/S_{max}$ for a single-pixel nerve embedded in muscle: the deviation from the maximum signal intensity is reduced to less than 1% with echo spacing values between 3.6 and 4.5 msec and relative signal plateau lengths ranging between 60% and 70% of the total echo train length. The deviation from the maximum nerve signal intensity is zero for an echo spacing of 4.0 msec and a relative plateau length of 60% (defining flip angle train A). Figure 3c plots the combined deviation from maximum signal and minimum blurring $|S_{max}\text{-}S|/S_{max} + |b_{min}\text{-}b|/b_{min}$. The combined metric is reduced to less than 12%, with echo spacing values between 3.5 and 4.1 msec and with relative plateau lengths greater than 83%. The combined metric reaches a minimum value of 10% at an echo spacing of 4.0 msec and relative plateau length of 85% (defining flip angle train B). Figure 3d–f show similar plots for the case of nerve embedded in suppressed fat. In this case, width broadening is restored to the case of no blurring at echo spacing values smaller than 3.7 msec and plateau lengths larger than 90% of the total echo train length. The deviation from maximum signal intensity is reduced to less than 1%, with echo spacing values between 3.5 and 4.3 msec and with relative signal plateaus ranging between 50% and 70% of the total echo train length. The deviation from the maximum nerve signal intensity is in this case zero for an echo spacing of 3.9 msec and a relative plateau length of 60% (defining flip angle train A*). The combined deviation from maximum signal and minimum blurring is reduced to less than 10% with echo spacing values between 3.4 and 4. 2 msec and with relative plateau lengths larger than 78%. The combined metric reaches a minimum value of 8% at an echo spacing of 3.7 msec and relative plateau length of 85% (defining flip angle train B*).

The effects of flip angle trains A and B on signal loss and width broadening on a single-pixel nerve embedded both in muscle and in suppressed fat are illustrated in Fig. 4. The simulated profiles show that, although flip angle trains A and B were computed for nerve embedded in muscle, similar effects are expected when nerve is embedded within a region with zero signal (ie, suppressed fat).

In Vivo Measurements

Tables 1 and 2 list the measured normalized signal intensities and widths of the L5 and L3 lumbar nerves, respectively. In both cases, the measure $(S_B\text{-}S_A)/S_A$ in the fourth

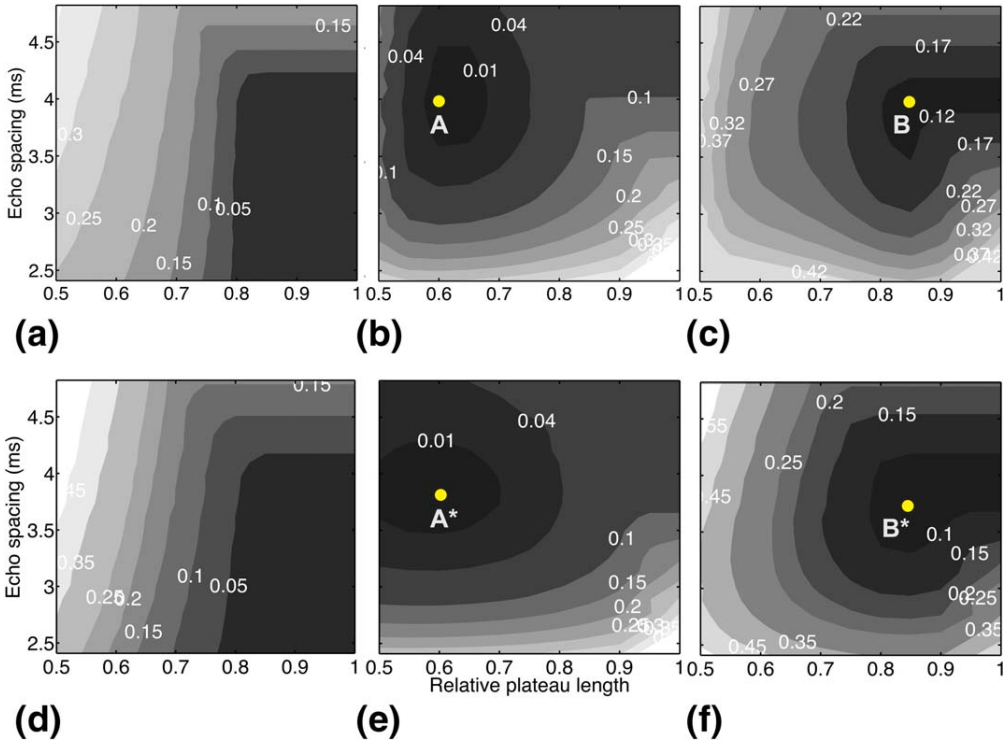

FIGURE 3: Deviation of signal response from optimal values simulated for single-pixel nerves, considering blurring effects from both nerve and the enveloping tissue: muscle (top), suppressed fat (bottom). The deviation of width broadening of nerve $|b_{min}-b|/b_{min}$ shown in (a) for nerve in muscle and in (d) for nerve in suppressed fat is minimized at longer plateau lengths. The deviation of nerve signal $|S_{max}-S|/S_{max}$ in (b) for nerve in muscle and in (e) for nerve in suppressed fat is minimized at a relative signal plateau length of 0.6 and echo spacing of 4 msec when nerve is surrounded by muscle and with a slightly smaller echo spacing of 3.9 msec when nerve is surrounded by suppressed fat (points A and A*, respectively). As a result of the two mechanisms, the joint deviation of signal and width broadening $|S_{max}-S|/S_{max} + |b_{min}-b|/b_{min}$ shown in (c) for nerve in muscle and in (f) for nerve in suppressed fat reaches a distinct minimum with a flip angle train associated with a relative signal plateau length of 0.85 and an echo spacing of 4 msec when nerve is surrounded by muscle and with an echo spacing of 3.7 msec when nerve is surrounded by suppressed fat (points B and B*, respectively).

column indicates signal *loss* implied by using the optimized flip angle train B, expected to give the best compromise between signal and sharpness of small nerves, instead of flip angle train A, expected to yield maximum nerve signal. Similarly, the quantity $(b_A-b_B)/b_A$ in the last column represents an *improvement* in width broadening expected when using flip angle train B instead of A.

In the case of L5 nerves, having in general a larger diameter than L3 nerves, an average signal loss of 23% was observed when using flip angle train B instead of A.

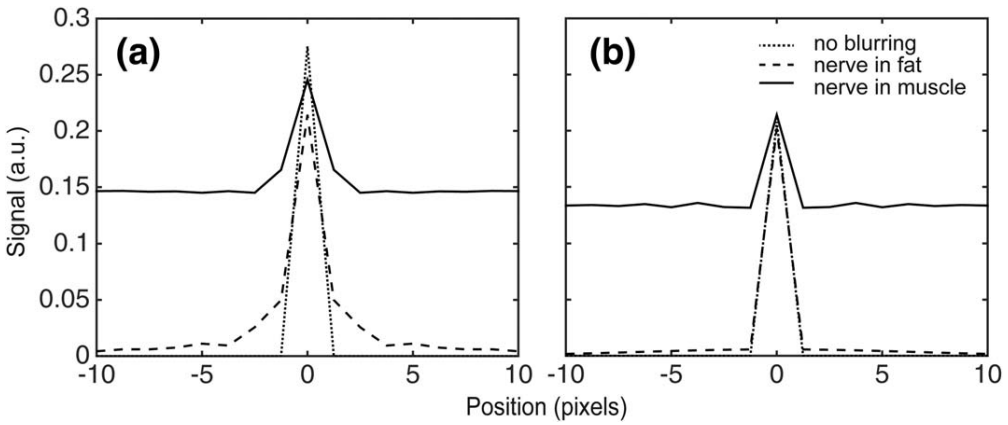

FIGURE 4: Simulated intensity profiles of a single-pixel nerve illustrating for flip angle trains A (left) and B (right) the effect on the signal response of the combined blurring mechanisms of nerve and the enveloping tissue. In the two cases of nerve embedded in muscle and of nerve embedded in suppressed fat, flip angle train B yields lower signal but restores blurring to its minimum value. a.u. = arbitrary units.

TABLE 1. Signal Variation and Width Broadening of L5 Lumbar Nerves Between Flip Angle Trains A and B Measured in 10 Healthy Subjects

	Measured signal (a.u.) Mean (SD)			Measured width broadening (pixels) Mean (SD)		
Subject	S_A	S_B	$(S_B-S_A)/S_A$	b_A	b_B	$(b_A-b_B)/b_A$
1	0.55 (0.02)	0.40 (0.01)	−0.28 (0.05)	6.87 (0.12)	6.14 (0.10)	0.04 (0.02)
2	0.51 (0.02)	0.37 (0.01)	−0.28 (0.04)	10.05 (0.33)	9.81 (0.21)	0.02 (0.02)
3	0.49 (0.02)	0.42 (0.01)	−0.15 (0.05)	7.85 (0.10)	7.86 (0.14)	0.00 (0.01)
4	0.40 (0.03)	0.33 (0.00)	−0.17 (0.06)	9.40 (0.88)	8.55 (0.31)	0.08 (0.08)
5	0.50 (0.03)	0.41 (0.02)	−0.17 (0.01)	5.19 (0.35)	4.93 (0.34)	0.05 (0.02)
6	0.54 (0.01)	0.55 (0.01)	0.01 (0.02)	8.05 (0.24)	7.92 (0.27)	0.02 (0.02)
7	0.40 (0.01)	0.37 (0.01)	−0.09 (0.03)	6.81 (0.47)	6.58 (0.38)	0.03 (0.04)
8	0.39 (0.01)	0.24 (0.00)	−0.39 (0.03)	6.14 (0.11)	5.54 (0.14)	0.10 (0.02)
9	0.77 (0.03)	0.49 (0.02)	−0.36 (0.05)	7.17 (0.55)	7.73 (0.43)	−0.08 (0.06)
10	0.45 (0.00)	0.34 (0.01)	−0.25 (0.03)	6.90 (0.22)	6.30 (0.26)	0.09 (0.06)
Mean (SD)	0.50 (0.11)	0.39 (0.08)	−0.23 (0.12)	n.r.	n.r.	0.04 (0.05)

a.u. = arbitrary units, SD = standard deviation, n.r. = not relevant.

Accompanying this effect, an average improvement in width broadening of 4% was observed for this type of nerve. For L3 nerves, an average signal loss of 9% and an average improvement in width broadening of 16% were observed with design B compared to A. In addition, flip angle train A resulted in normalized signal intensities for nerves L5 and L3 nerves equal to 0.50 ± 0.11 and 0.40 ± 0.11, respectively. In contrast, the optimized flip angle train B was found to give average signal intensities of 0.39 ± 0.08 for L5 nerves and 0.35 ± 0.07 for L3 nerves.

The thinner L3 nerves were therefore observed to experience a smaller signal loss and a larger reduction in

TABLE 2. Signal Variation and Width Broadening of L3 Lumbar Nerves Between Flip Angle Trains A and B Measured in 10 Healthy Subjects

	Measured signal (a.u.) Mean (SD)			Measured width broadening (pixels) Mean (SD)		
Subject	S_A	S_B	$(S_B-S_A)/S_A$	b_A	b_B	$(b_A-b_B)/b_A$
1	0.44 (0.02)	0.38 (0.01)	−0.14 (0.05)	3.02 (0.11)	2.74 (0.11)	0.09 (0.04)
2	0.28 (0.01)	0.32 (0.00)	0.14 (0.05)	4.35 (0.45)	3.51 (0.15)	0.19 (0.07)
3	0.31 (0.01)	0.32 (0.01)	0.01 (0.03)	5.31 (0.47)	4.10 (0.30)	0.22 (0.07)
4	0.31 (0.03)	0.36 (0.02)	0.18 (0.15)	3.96 (0.40)	3.49 (0.19)	0.11 (0.05)
5	0.44 (0.02)	0.42 (0.02)	−0.05 (0.02)	4.11 (0.19)	3.45 (0.27)	0.16 (0.06)
6	0.41 (0.03)	0.39 (0.03)	−0.05 (0.03)	4.78 (0.47)	3.67 (0.42)	0.23 (0.10)
7	0.26 (0.03)	0.18 (0.02)	−0.29 (0.14)	4.25 (0.24)	3.35 (0.37)	0.21 (0.06)
8	0.41 (0.02)	0.33 (0.01)	−0.21 (0.02)	5.11 (0.67)	4.18 (0.51)	0.17 (0.09)
9	0.63 (0.04)	0.45 (0.04)	−0.27 (0.02)	4.27 (0.73)	3.68 (0.50)	0.13 (0.05)
10	0.50 (0.02)	0.37 (0.01)	−0.26 (0.02)	4.00 (0.09)	3.63 (0.14)	0.09 (0.02)
Mean (SD)	0.40 (0.11)	0.35 (0.07)	**−0.09 (0.16)**	n.r.	n.r.	**0.16 (0.05)**

a.u. = arbitrary units, SD = standard deviation, n.r. = not relevant.

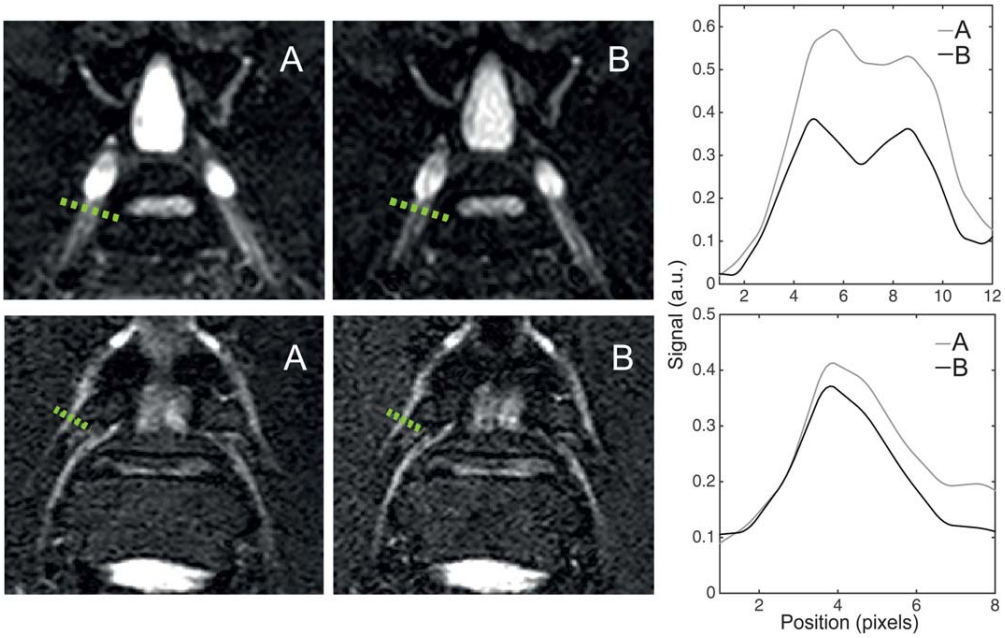

FIGURE 5: Source images and corresponding intensity profiles, shown for a single location of a single subject, illustrating the effect on the observed signal response for the L5 (top) and L3 (bottom) nerve roots with the two flip angle train designs denoted as A and B in Fig. 3. The optimized design B yields in both cases lower signal but improved blurring and delineation, while also giving smaller variation of signal intensity with nerve size. With respect to design A, expected to give maximum signal intensities, design B yields a decrease in signal of 35% and no effective change in width broadening in L5 nerves and a decrease in signal of 10% and an improved width blurring of 13% in L3 nerves. In Tables 1 and 2 multiple adjacent locations were averaged for each subject, which is why these values are not explicitly listed therein. a.u. = arbitrary units.

width when employing the optimized refocusing angle design B. These measurements are in agreement with the presented simulations, which predict a signal loss of 25% in thick nerves and of 10% in thin nerves and an improvement of 20% when changing from flip angle design A to B.

Intensity profiles of the L5 and L3 nerves measured from the source images of a single location of a single subject are shown in Fig. 5. The signal loss observed with flip angle train B relative to flip angle train A is larger for the thicker L5 nerve than it is for the thinner L3 nerve. Moreover, the change of flip angle train induces larger changes in width for L3 nerves than L5 nerves.

Figure 6 displays maximum intensity projection (MIP) maps of the lumbar plexus of two subjects. The images obtained using the optimized flip angle train B show an overall reduction in signal and an improvement in sharpness.

Visual grading of image quality observed with flip angle trains A and B resulted in a statistically significant improvement in the sharpness of the L3 femoral nerve within the quadratus lumborum muscle when using flip angle train B ($P = 0.005$). The ability to resolve fascicles within the L3 nerve immediately after the ganglion significantly improved in the images acquired with flip angle train B compared to the images acquired with flip angle train A ($P = 0.019$). Similarly, the ability to resolve fascicles within the L5 nerve root significantly improved in the images acquired with flip angle train B compared to the images acquired with flip angle train A ($P = 0.009$). The average ICC for interreader agreement of flip angle train A was 0.77. For flip angle train B, the average ICC for interreader agreement was 0.975. In the intrareader evaluation, the average ICC values were 0.803 and 0.845 for flip angle trains A and B, respectively.

Since the focus of this study was to evaluate the particular case of thin nerve branches, which are most strongly affected by blurring effects and which tend to be embedded in muscle, in vivo data were not acquired for the optimal flip angles trains calculated for nerve embedded in suppressed fat. However, the presented signal simulations show that the optimized flip angle train B also improves the delineation of thin nerves when embedded in fat with suppressed signal.

DISCUSSION

The present study shows the need to consider geometry-specific blurring effects resulting from refocusing flip angle modulation in 3D TSE when imaging small nerves embedded in another tissue. The provided theoretical framework describes the coupling between the signal of nerves of different shapes and the blurring of the interfacing muscle and is used to generate a flip angle train that gives an optimum signal and sharpness compromise. The experimental validation of the supporting theory shows an agreement between the observed and the simulated signal response of nerves of

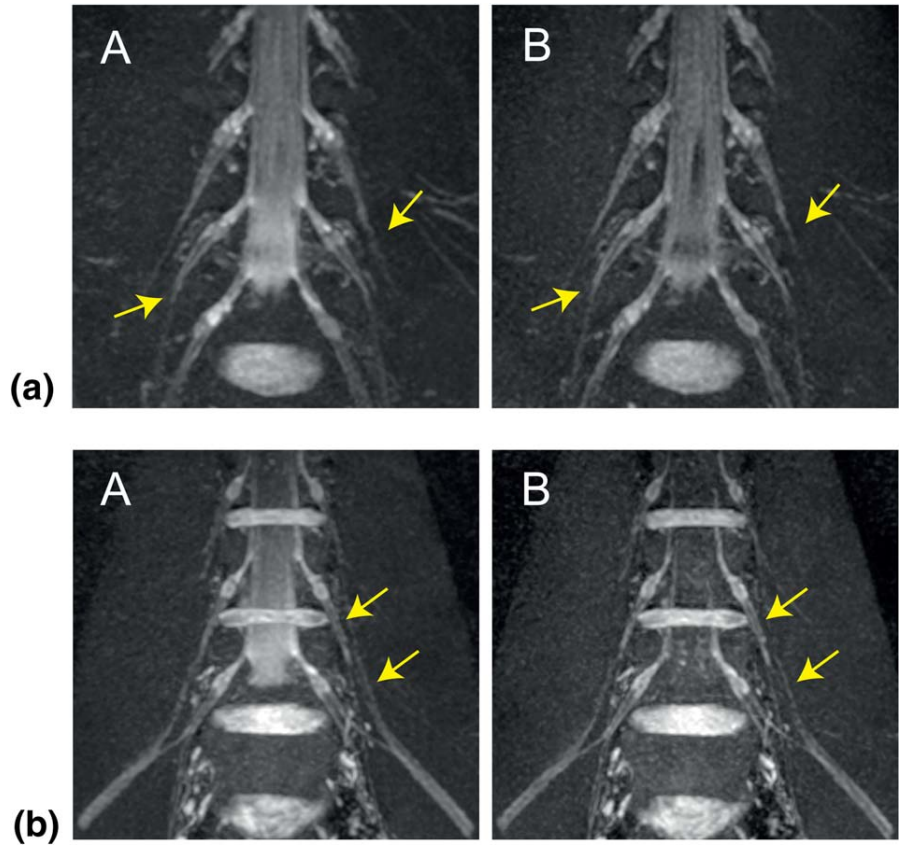

FIGURE 6: Maximum intensity maps (MIPs) of two subjects obtained with flip angle train designs A and B. The optimized design B yields lower overall signal but improved delineation of small nerves. Yellow arrows indicate regions where small nerves are particularly better delineated when using design B.

different sizes and thus verifies the validity of the proposed flip angle train optimization technique.

Tissue-specific refocusing angle modulation in 3D TSE has been shown to give satisfactory results in nerve imaging[17] and is continuously being implemented.[4,5,16] Given the frequent use of 3D TSE in nerve imaging and the existing need for isotropic, high-resolution 3D images in regions with high obliquities and where nerves have reduced sizes, it is meaningful to improve the capability of the imaging sequence to provide more accurate morphological images. The present work shows that an improvement in image quality can be achieved by putting careful thought into the modulation of refocusing angles in 3D TSE.

In comparison to known studies that have similarly noted the dependence of the final signal response of an embedded tissue to its sequence-dependent MTF and to its spatial setting,[18,19] this work presents a complete methodology that, for nerve embedded in muscle, describes the individual contributions of flip-angle-modulation effects on the embedded and the surrounding tissues and of the specific geometry. Also in contrast with this related literature, the present work carries out a thorough quantitative evaluation of signal loss and width broadening effects in order to objectively explain the results observed qualitatively.

In the context of optimization strategies carried out for 3D TSE and similar imaging sequences in various anatomical regions,[12,13,19] this work provides a geometry-specific flip angle modulation strategy for small nerves, which was demonstrated for lumbar nerves but can be readily transferred to peripheral nerves in general, with minor modifications of geometry and relaxation specifications. Not presented in this study, similar flip angle modulation strategies tested on nerves in the extremities yielded satisfactory results.

Particularly in imaging of structures that have requirements on both signal intensity and sharpness, numerical simulations herein demonstrated that it is advantageous to use a metric to simultaneously assess signal loss and width broadening of a tissue and that with such an approach it is possible to determine a flip angle train that best meets these requirements (train B). Moreover, as shown in these results, the proposed methodology can be used to find flip angle trains that alternatively optimize a different set of properties (such as maximum signal intensity with train A).

Simulation results were found to be in good agreement with experimental measurements. Although the proposed flip angle train B resulted in an inevitable loss of signal in both L5 and L3 nerves, in comparison to flip angle train A,

expected to yield maximum signal, the major signal reduction was observed to take place for the thicker L5 nerves, while the signal of the thinner L3 nerves was only slightly disturbed. Also of relevance, flip angle train B led to a significant reduction of blurring-induced nerve width broadening in the case of the thinner L3 nerves.

In addition to improving the delineation of the thin L3 nerves at the interface with muscle, the improved sharpness delivered by flip angle train B was observed to generate enhanced delineation of structures *within* both thin and thick nerves. Namely, the inner fascicles of the L3 and L5 nerves were in general better resolved with the optimized flip angle train. Both of these effects were confirmed across subjects by the visual grading and statistical results. The delineation of the fascicles within the nerves was not further interpreted in this work and requires supplemental investigation. As another additional effect, the signal of the pulsating cerebrospinal fluid (CSF) was reduced when using flip angle train B, which is likely a result of the flow sensitivity of the 3D TSE sequence. Similarly, this result was not further assessed and requires additional investigation.

The present study has some limitations. First, the optimization presented in the present work was carried out for a selected parameter space and the resulting optimization of flip angle modulation is therefore specific to this subselection of 3D TSE sequences. The selection of sequence parameters, for both numerical simulations and in vivo measurements, was based on desired image quality and scan duration and was further constrained by software limits as well as by additional imaging parameters related to acquisition strategy and acceleration. However, the theoretical framework presented in this study should also hold if other sequences parameters are to be used. Second, it is in the nature of 3D TSE employing tissue-specific flip angle modulation that the relaxation times of the reference tissue contribute to the generation of specific refocusing trains. As relaxation times of nerve can vary between anatomical locations and between subjects, it is important to note that the exact optimal flip angle train might be altered in different scenarios. In the current study of lumbar nerves, variations in relaxation parameters are expected even along individual nerves between the dorsal root ganglia and the more distal regions.[25] Therefore, the presented results comparing the observed signal response from different nerves with different geometries might also be affected by varying relaxation parameters within and across nerve types. Separate simulations were performed with a range of T_2 values found in the literature corresponding to variable regions of lumbar nerves and the resulting optimized flip angle trains were not found to vary majorly. Nonetheless, the present results are likely to reflect a combined influence of nerve geometry and of variations in nerve relaxation properties. Third, the small signal loss associated with the optimized flip angle train B compared to flip angle train A might be undesired in scans with a very low signal-to-noise ratio (SNR). In very low SNR scans, the signal from the small nerve structures would be comparable to the noise floor with either flip angle train A or B. Scans with very low SNR should therefore aim to maximize the overall nerve signal using flip angle train A.

In conclusion, optimization of the flip angle train used in high-, isotropic-resolution 3D TSE imaging of small oblique nerves should consider geometry-specific blurring effects from both the nerve and the surrounding tissue. An optimized flip angle train was designed providing a compromise between signal and blurring effects. In vivo results from the lumbar plexus of healthy volunteers demonstrated the superior capability of the optimized flip angle train in visualizing small nerve structures in oblique configurations using 3D TSE imaging with high isotropic resolution. The proposed refocusing angle design is therefore recommended for 3D TSE imaging of small nerves with high obliqueness in cases when it is a major concern to improve the sharpness of thin nerves and when a minor loss of signal can be tolerated.

ACKNOWLEDGMENTS

Contract grant sponsor: Philips Healthcare.
The authors thank Dr. Kim van de Ven and Dr. Tobias Henning for useful discussions.

REFERENCES

1. Thawait SK, Chaudhry V, Thawait GK, et al. High-resolution MR neurography of diffuse peripheral nerve lesions. AJNR Am J Neuroradiol 2011;32:1365–1372.
2. Chhabra A, Andreisek G, Soldatos T, et al. MR neurography: past, present, and future. AJR Am J Roentgenol 2011;197:583–591.
3. Hennig J, Nauerth A, Friedburg H. RARE imaging: a fast imaging method for clinical MR. Magn Reson Med 1986;3:823–833.
4. Soldatos H, Andreisek G, Thawait GK, et al. High-resolution 3-T MR neurography of the lumbosacral plexus. RadioGraphics 2013;33:967–987.
5. Chhabra A, Thawait GK, Soldatos T, et al. High-resolution 3T MR neurography of the brachial plexus and its branches, with emphasis on 3D imaging. AJNR Am J Neuroradiol 2013;34:486–497.
6. Busse RF, Hariharan H, Vu A, Brittain JH. Fast spin echo sequences with very long echo trains: design of variable refocusing flip angle schedules and generation of clinical T2 contrast. Magn Reson Med 2006;55:1030–1037.
7. Mugler JP. Practical implementaion of optimized tissue-specific prescribed signal evolutions for improved turbo-spin-echo imaging. In: Proc 11th Annual Meeting ISMRM, Toronto; 2003. p 203.
8. Mugler JP 3rd. Optimized three-dimensional fast-spin-echo MRI. J Magn Reson Imaging 2014;39:745–767.
9. Mugler JP, Kiefer B, Brookeman JR. Three-dimensional T2-weighted imaging of the brain using very long spin-echo trains. In: Proc 8th Annual Meeting ISMRM, Denver; 2000. p 687.

10. Busse RF, Brau AC, Vu A, et al. Effects of refocusing flip angle modulation and view ordering in 3D fast spin echo. Magn Reson Med 2008;60:640–649.

11. Weigel M, Schwenk S, Kiselev VG, Scheffler K, Hennig J. Extended phase graphs with anisotropic diffusion. J Magn Reson 2010;205:276–285.

12. Chen W, Granlund K, Huo D, Gold GE. A systematic approach to design flip angle modulation in pseudo-steady-state 3D fast spin echo acquisition. In: Proc 21st Annual Meeting ISMRM, Salt Lake City; 2013. p 3716.

13. Lee H, Kim EY, Yang KS, Park J. Susceptibility-resistant variable-flip-angle turbo spin echo imaging for reliable estimation of cortical thickness: a feasibility study. Neuroimage 2012;59:377–388.

14. Mugler JP, Wald LL, Brookeman JR. T2-weighted 3D spin-echo train imaging of the brain at 3 Tesla: reduced power deposition using low flip-angle refocusing RF pulses. In: Proc 9th Annual Meeting ISMRM, Glasgow; 2001. p 438.

15. Park J, Mugler JP 3rd, Horger W, Kiefer B. Optimized T1-weighted contrast for single-slab 3D turbo spin-echo imaging with long echo trains: application to whole-brain imaging. Magn Reson Med 2007;58: 982–992.

16. Kasper JM, Wadhwa V, Scott KM, Rozen S, Xi Y, Chhabra A. SHINKEI-a novel 3D isotropic MR neurography technique: technical advantages over 3DIRTSE-based imaging. Eur Radiol 2015;25:1672–1677.

17. Yoneyama M, Nakamura M, Okuaki T, et al. High-resolution 3D volumetric nerve-sheath weighted RARE imaging (3D SHINKEI). In: Proc 19th Annual Meeting ISMRM, Montreal; 2011. p 2721.

18. Constable RT, Gore JC. The loss of small objects in variable TE imaging: implications for FSE, RARE, and EPI. Magn Reson Med 1992;28: 9–24.

19. Deichmann R, Good CD, Josephs O, Ashburner J, Turner R. Optimization of 3-D MP-RAGE sequences for structural brain imaging. Neuroimage 2000;12:112–127.

20. Hennig J, Scheffler K. Hyperechoes. Magn Reson Med 2001;46:6–12.

21. Hennig J, Weigel M, Scheffler K. Multiecho sequences with variable refocusing flip angles: optimization of signal behavior using smooth transitions between pseudo steady states (TRAPS). Magn Reson Med 2003;49:527–535.

22. Mugler JP, Epstein FH, Brookeman J. Shaping the signal response during the approach to steady state in three-dimensional magnetization-prepared rapid gradient-echo imaging using variable flip angles. Magn Reson Med 1992;28:165–185.

23. Ethofer T, Mader I, Seeger U, et al. Comparison of longitudinal metabolite relaxation times in different regions of the human brain at 1.5 and 3 Tesla. Magn Reson Med 2003;50:1296–1301.

24. Stanisz GJ, Odrobina EE, Pun J, et al. T1, T2 relaxation and magnetization transfer in tissue at 3T. Magn Reson Med 2005;54:507–512.

25. Karampinos DC, Melkus G, Shepherd TM, et al. Diffusion tensor imaging and T2 relaxometry of bilateral lumbar nerve roots: feasibility of in-plane imaging. NMR Biomed 2013;26:630–637.

26. Kollmer J, Hund E, Hornung B, et al. In vivo detection of nerve injury in familial amyloid polyneuropathy by magnetic resonance neurography. Brain 2015;138:549–562.

27. Gambarota G, Mekle R, Mlynarik V, Krueger G. NMR properties of human median nerve at 3T: proton density, T1, T2, and magnetization transfer. J Magn Reson Imaging 2009;29:982–986.

28. Gold GE, Han E, Stainsby J, Wright G, Brittain J, Beaulieu C. Musculoskeletal MRI at 3.0T: relaxation times and image contrast. AJR Am J Roentgenol 2004;183:343–351.

29. Morrow JM, Sinclair CD, Fischmann A, et al. Reproducibility, and age, body-weight and gender dependency of candidate skeletal muscle MRI outcome measures in healthy volunteers. Eur Radiol 2014;24:1610–1620.

30. Schwenzer NF, Martirosian P, Machann J, et al. Aging effects on human calf muscle properties assessed by MRI at 3 Tesla. J Magn Reson Imaging 2009;29:1346–1354.

31. Yoneyama M, Takahara T, Kwee TC, Nakamura M, Tabuchi T. Rapid high resolution MR neurography with a diffusion-weighted pre-pulse. Magn Reson Med Sci 2013;12:111–119.

5.2 Journal Publication II: Orthogonally Combined Motion- and Diffusion-Sensitized Driven Equilibrium (OC-MDSDE) Preparation for Vessel Signal Suppression in 3D Turbo Spin Echo Imaging of Peripheral Nerves in the Extremities

The publication entitled *Orthogonally Combined Motion- and Diffusion-Sensitized Driven Equilibrium (OC-MDSDE) Preparation for Vessel Signal Suppression in 3D Turbo Spin Echo Imaging of Peripheral Nerves in the Extremities* was published in Magnetic Resonance in Medicine (ISSN: 1522-2594). The manuscript was authored by Barbara Cervantes, Jan S. Kirschke, Elizabeth Klupp, Hendrik Kooijman, Peter Börnert, Axel Haase, Ernst J. Rummeny, and Dimitrios C. Karampinos.

Abstract

Purpose

To design a preparation module for vessel signalsuppression in MR neurography of the extremities, which causes minimal attenuation of nerve signal and is highly insensitive to eddy currents and motion.

Methods

The orthogonally combined motion- and diffusion-sensitized driven equilibrium (OC-MDSDE) preparation was proposed, based on the improved motion- and diffusion-sensitized driven equilibrium methods (iMSDE and FC-DSDE, respectively), with specific gradient design and orientation. OC-MDSDE was desensitized against eddy currents using appropriately designed gradient prepulses. The motion sensitivity and vessel signal suppression capability of OC-MDSDE and its components were assessed in vivo in the knee using 3D turbo spin echo (TSE). Nerve-to-vessel signal ratios were measured for iMSDE and OC-MDSDE in 7 subjects.

Results

iMSDE was shown to be highly sensitive to motion with increasing flow sensitization. FC-DSDE showed robustness against motion, but resulted in strong nerve signal loss with diffusion gradients oriented parallel to the nerve. OC-MDSDE showed superior vessel suppression compared to iMSDE and FC-DSDE and maintained high nerve signal. Mean nerve-to-vessel signal ratios in 7 subjects were 0.40 ± 0.17 for iMSDE and 0.63 ± 0.37 for OC-MDSDE.

Conclusion

OC-MDSDE combined with 3D TSE in the extremities allows high-near-isotropic-resolution imaging of peripheral nerves with reduced vessel contamination and high nerve signal.

Author Contributions

(i) The first author alone: designed the experiment; programmed the magnetic resonance pulse sequence (propriety hardware and software from Philips Medical Systems (Best, The Netherlands)); implemented the library of tools used to perform all numerical simulations (MATLAB and Statistics Toolbox Release 2016b, The MathWorks, Inc., Natick, Massachusetts, United States); performed all numerical simulations; performed all experiments (in vivo magnetic resonance measurements); and performed the quantitative data analysis. (ii) With the help and consultation of the coauthors, the first author: performed the statistical data analysis; and wrote the manuscript.

Orthogonally Combined Motion- and Diffusion-Sensitized Driven Equilibrium (OC-MDSDE) Preparation for Vessel Signal Suppression in 3D Turbo Spin Echo Imaging of Peripheral Nerves in the Extremities

Barbara Cervantes,[1]* Jan S. Kirschke,[2] Elizabeth Klupp,[2] Hendrik Kooijman,[3] Peter Börnert,[4] Axel Haase,[5] Ernst J. Rummeny,[1] and Dimitrios C. Karampinos[1]

Purpose: To design a preparation module for vessel signal suppression in MR neurography of the extremities, which causes minimal attenuation of nerve signal and is highly insensitive to eddy currents and motion.

Methods: The orthogonally combined motion- and diffusion-sensitized driven equilibrium (OC-MDSDE) preparation was proposed, based on the improved motion- and diffusion-sensitized driven equilibrium methods (iMSDE and FC-DSDE, respectively), with specific gradient design and orientation. OC-MDSDE was desensitized against eddy currents using appropriately designed gradient prepulses. The motion sensitivity and vessel signal suppression capability of OC-MDSDE and its components were assessed in vivo in the knee using 3D turbo spin echo (TSE). Nerve-to-vessel signal ratios were measured for iMSDE and OC-MDSDE in 7 subjects.

Results: iMSDE was shown to be highly sensitive to motion with increasing flow sensitization. FC-DSDE showed robustness against motion, but resulted in strong nerve signal loss with diffusion gradients oriented parallel to the nerve. OC-MDSDE showed superior vessel suppression compared to iMSDE and FC-DSDE and maintained high nerve signal. Mean nerve-to-vessel signal ratios in 7 subjects were 0.40 ± 0.17 for iMSDE and 0.63 ± 0.37 for OC-MDSDE.

Conclusion: OC-MDSDE combined with 3D TSE in the extremities allows high-near-isotropic-resolution imaging of peripheral nerves with reduced vessel contamination and high nerve signal. **Magn Reson Med 79:407–415, 2018. © 2017 Wiley Periodicals, Inc.**

Key words: magnetic resonance neurography; peripheral nerves MRI; motion-sensitized diffusion preparation (MSDE); black blood imaging; 3D turbo spin echo (TSE)

INTRODUCTION

Thin-section, high-resolution sequences are gaining interest in imaging of the peripheral nerves that are dedicated to optimally increase the conspicuity of nerve tissue signal (1–8). Although neurographical sequences have made substantial progress through time and many technical aspects contributing to image quality have been addressed (9–15), a major challenge that persists is the difficulty to address unwanted small-vessel signal without disrupting the signal of nerves (2), attributed to similar T_1 relaxation times between blood and nerves and the long T_2 relaxation times of the two tissues. Previous techniques have used a flow-sensitized preparation in spin echo imaging (16–18) or low b-value diffusion weighting in gradient echo imaging (19) to suppress such vessel signal and thus improve the visualization of the peripheral nerves.

Flow-sensitized preparations, such as the motion-sensitized driven equilibrium (MSDE) preparation, have been shown to help reduce the signal of fast flowing blood in imaging the vessel wall of large vessels (20,21) and in angiography (22,23). However, in order to reduce the signal of slowly flowing blood in small vessels, the first gradient moment (m_1) of MSDE needs to be significantly increased, which unavoidably increases the sensitivity to motion and can result in artifacts. In contrast, flow-compensated diffusion preparation is less sensitive to motion-induced phase errors. In nerve imaging, such a flow-compensated diffusion preparation is also suitable for attenuating vessel signal, given the significantly higher diffusion coefficient of blood compared to nerve when the diffusion gradients are applied perpendicular to the nerve axis. By considering the tendency of peripheral nerves and surrounding vessels in the extremities to have a common preferential orientation, as well as the high dependence of motion sensitivity on the choice of gradient direction relative to the anatomy, it is possible to combine flow and diffusion sensitization in orthogonal axes to benefit from both dephasing mechanisms to improve nerve conspicuity.

The extremities have been shown to be a region where vessel signal interferes with the visualization of the nerves (19,24). Given that large veins and arteries with fast flow in this region tend to run in the same direction as the nerves and smaller vessels with slow flow are more tortuous and run in many directions, the extremities appear as a region where the orthogonal application of motion (flow) and diffusion sensitization can be

[1]Department of Diagnostic and Interventional Radiology, Technische Universität München, Munich, Germany.
[2]Department of Neuroradiology, Technische Universität München, Munich, Germany.
[3]Philips Healthcare, Hamburg, Germany.
[4]Philips Research Laboratory, Hamburg, Germany.
[5]Institute of Medical Engineering, Technische Universität München, Garching, Germany

Grant sponsor: Philips Healthcare.

*Correspondence to: Barbara Cervantes, MS, Department of Diagnostic and Interventional Radiology, Klinikum rechts der Isar, Technische Universität München, Ismaninger Straße 22, 81675 Munich, Germany.
E-mail: b.cervantes@tum.de

Received 16 September 2016; revised 6 February 2017; accepted 7 February 2017
DOI 10.1002/mrm.26660
Published online 5 March 2017 in Wiley Online Library (wileyonlinelibrary.com).

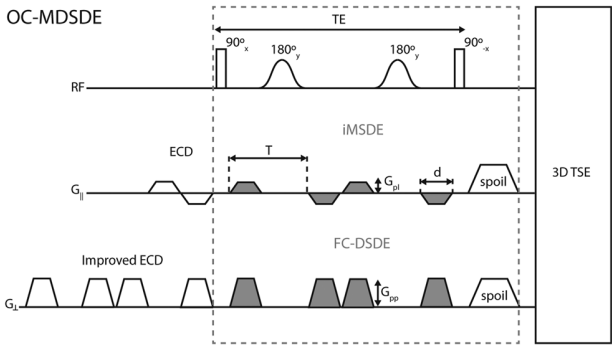

FIG. 1. OC-MDSDE preparation sequence showing the combination of the iMSDE and FC-DSDE components. For the RF component, a DRHS design is used to improve robustness against B_0 and B_1 inhomogeneities. The iMSDE component in OC-MDSDE uses low flow-sensitizing gradient strengths $\mathbf{G_{pl}}$ in the direction parallel to the nerve and the FC-DSDE component uses high diffusion-sensitizing gradient strengths $\mathbf{G_{pp}}$ perpendicular to the nerve. Gradient duration **d** and separation **T** are the same for both iMSDE and FC-DSDE components. Double-bipolar and quadruple-monopolar gradient pulses are used in iMSDE and FC-DSDE, respectively, before excitation for ECD.

highly advantageous for vessel suppression. Moreover, given that sagittal and coronal views of long segments of peripheral nerves in the extremities can be useful in the identification of regions with pathology, it is advantageous to combine signal preparation with a 3D readout utlizing isotropic resolution.

The purpose of the present work is to develop an orthogonally combined motion- and diffusion-sensitized driven equilibrium (OC-MDSDE) preparation sequence that yields improved vessel-signal suppression and high nerve signal for imaging of peripheral nerves in the extremities. The proposed preparation scheme is combined with a 3D turbo spin echo (TSE) acquisition and its vessel suppression capability is demonstrated in vivo in the knee region.

METHODS

Pulse Sequence Design

The proposed OC-MDSDE preparation module was implemented based on the improved motion-sensitized driven equilibrium (iMSDE) module (25) and on the flow-compensated diffusion-sensitized driven equilibrium (FC-DSDE) module. This merge is schematically shown in Figure 1. The backbone of this preparation sequence is the radiofrequency (RF) pulse train, for which a dual refocused hyperbolic secant (DRHS) design was chosen, because of its reduced sensitivity to main field and transmit B_1 field inhomogeneities (25). The flow- and diffusion-sensitizing gradients (shown in gray in Fig. 1) were designed to compensate the gradient zeroth moment ($m_0 = 0$) in iMSDE and both the zeroth and first moments ($m_0 = m_1 = 0$) in FC-DSDE, respectively. The composed OC-MDSDE preparation was followed by a 3D TSE readout after spoiling of residual transverse magnetization.

Flow-sensitizing gradients in the iMSDE component were oriented parallel to the nerve and diffusion-sensitizing gradients in the FC-DSDE component were oriented perpendicular to the nerve, with the aim of minimizing both motion-induced artifacts and diffusion-induced attenuation of the nerve signal. In imaging of the lower extremities, flow-sensitizing gradients ($G_{\parallel}$ in Fig. 1) were applied in the feet-head direction, corresponding to the frequency-encoding axis; diffusion-sensitizing gradients ($G_{\perp}$ in Fig. 1) were applied in the anterior-posterior direction, corresponding to the first phase encoding axis of the 3D acquisition. Moderate flow-sensitizing gradient strengths $\mathbf{G_{pl}}$ were used in the iMSDE component to generate a sufficiently large m_1 to reduce vessel signal, while simultaneously generating a small b value (<50 s/mm^2) to minimize diffusion attenuation of the nerve signal. In the FC-DSDE component, diffusion-sensitizing gradient strengths $\mathbf{G_{pp}}$ were roughly 4 times higher than $\mathbf{G_{pl}}$ to reduce vessel signal by means of diffusion and of second and higher gradient moment mechanisms.

Residual eddy currents induced by the flow- or diffusion-sensitizing gradients can induce a significant signal loss after the preparation module (26). A bipolar gradient prepulse was therefore included in the iMSDE implementation and used in all measurements for eddy current desensitization (ECD) (27). In the FC-DSDE part, a monopolar gradient prepulse consisting of four lobes was implemented for the same purpose. The four-lobe ECD design, from here onward denoted as improved ECD, was chosen based on the previous finding that a train of gradient prepulses identical to the sensitizing gradient pulses in the sequence are effective in reducing residual eddy currents (28).

Simulations of Eddy Current Effects

The effects of eddy currents on the prepared signal were simulated for the FC-DSDE part of the module (c.f. Fig. 1), in which large gradient strengths were used. The spatially linear eddy current gradient field $\boldsymbol{g}_{\mathbf{rise}}$ generated during the rising ramp (with a duration $\boldsymbol{r}$) of an applied trapezoidal gradient of the amplitude $\boldsymbol{G_0}$, was modeled by a single time constant τ and weighting $\boldsymbol{w}$ as:

$$g_{\text{rise}}(t) = \begin{cases} -G_0 \ \frac{\tau}{r} w \ \left[1 - \exp\left(-\frac{t}{\tau}\right)\right], 0 \le t < r \\ -G_0 \ \frac{\tau}{r} w \ \left[1 - \exp\left(-\frac{r}{\tau}\right)\right] \exp\left(-\frac{t-r}{\tau}\right), t \ge r. \end{cases}$$

The linear eddy current field generated during the falling ramp of the trapezoid, $\boldsymbol{g}_{\mathbf{fall}}$, was modeled following the same principle (29), but with opposite polarity. The net linear eddy current field generated by the whole trapezoidal gradient was then determined from the superposition of $\boldsymbol{g}_{\mathbf{rise}}$ and $\boldsymbol{g}_{\mathbf{fall}}$. These eddy current fields were simulated for the complete diffusion gradient waveform in FC-DSDE for time constants in the range of 0.1 to 200 ms and with a constant eddy current weighting of 0.13 (25). Distortions to the applied gradient lobes induced by eddy currents were then simulated for all diffusion gradients, and the residual gradient zeroth moment m_0 at the end of the preparation was computed. This procedure was performed for the FC-DSDE preparation utilizing no ECD gradients and for FC-DSDE using the above-

described ECD gradient prepulse designed to maximize robustness to eddy currents. Similar to previous work that investigated eddy currents in similar sequences (30), signal attenuation of static spins was determined from the mean phase accumulation at the end of the preparation, just before the final RF pulse that flips the transverse magnetization into the longitudinal axis, at distances from the magnet isocenter ranging from 0 to 20 cm.

In Vivo Measurements

Seven healthy volunteers (mean age, 31 ± 8 years; 4 males, 3 females) participated in the study. The study was approved by the local institutional review board and conducted in accord with the committee for human research. All subjects gave written informed consent before their participation in the study. All acquisitions were performed with a 3 Tesla whole-body Philips scanner (Philips Ingenia, Best, The Netherlands) with a 16-channel transmit-receive knee coil. Subjects were positioned supine and the coil was centered at the kneecap to cover the tibial and peroneal nerves above and below the knee. Low-resolution surveys in sagittal and coronal planes and a 2D T_2-weighted TSE scan were acquired axially to aid alignment of the desired imaging volume to the curved path of the nerves. All 3D acquisitions were performed sagittally with a 3D TSE readout utilizing three different preparation modules: iMSDE, FC-DSDE, and OC-MDSDE, using the following 3D TSE sequence parameters for all acquisitions: field of view $= 270 \times 165 \times 100\,mm^3$; acquisition voxel $= 1.25 \times 1.25 \times 1.4\,mm^3$; reconstruction voxel $= 0.63 \times 0.63 \times 0.7\,mm^3$; repetition time/echo time (TE) = 2,000/273 ms; echo train length = 150; fat suppression using spectral adiabatic inversion recovery; number of signal averages = 2 using phase cycling for removal of free induction decay artifacts; parallel imaging using sensitivity encoding (SENSE) with reduction factor R = 2.5 (anterior-to-posterior phase encoding direction); and total scan duration = 2 minutes 18 seconds. The 3D TSE imaging readout used a variable flip angle train optimized to delineate thin nerves embedded in muscle considering the nerve geometry and the blurring mechanisms characteristic for nerve and muscle in 3D TSE (31).

In Vivo Validation of ECD

For in vivo validation of the ECD, three measurements were made for 1 subject using different preparation modules. The preparation module in the first measurement introduced only a T_2 weighting ($TE_{prep} = 57$ ms) and no vessel suppression (G = 0 mT/m). In the second measurement, OC-MDSDE without ECD was applied ($TE_{prep} = 65$ ms; $G_{pl,pp} = (6, 44)$ mT/m). In the third measurement, OC-MDSDE using the same sequence parameters was applied, but utilizing ECD.

In Vivo Assessment of Motion Sensitivity

The sensitivity to motion of FC-DSDE (in the 2 cases of diffusion-sensitizing gradients parallel and perpendicular to the nerve) compared to iMSDE (motion-sensitizing gradients parallel to the nerve) was assessed for 1 subject by means of increasing strength of the sensitizing gradients in each sequence while keeping a constant $TE_{prep} = 50$ ms. Sagittal 3D TSE images were acquired with iMSDE parallel to the nerve (three acquisitions with increasing gradient strengths $G_{pl} = 4$, 6, and 43 mT/m), FC-DSDE parallel to the nerve (three acquisitions with $G_{pp} = 4$, 6, and 45 mT/m), and with FC-DSDE perpendicular to the nerve ($G_{pp} = 4$, 6, and 45 mT/m). Gradient strengths were chosen for iMSDE and FC-DSDE to generate similar b-values and thus comparable sensitivity to motion in directions transverse to the nerve.

In Vivo Evaluation of Vessel Signal Suppression

The effectiveness of vessel signal suppression of the iMSDE, FC-DSDE, and OC-MDSDE preparation schemes was evaluated for 1 subject. Sagittal 3D TSE images were first acquired with the preparation module without active gradients resulting in no vessel suppression, to be used as a reference. Images with iMSDE were acquired using a high m_1 of 6,780 mT ms^2/m to maximize vessel suppression. Images with FC-DSDE perpendicular to the nerve were acquired with a moderate b-value of 300 s/mm^2 ($m_1 = 0$), and images with OC-MDSDE were acquired with b = 325 s/mm^2 and $m_1 = 3{,}914$ mT ms^2/m. TE_{prep} was 57 ms in all 3 cases.

Vessel suppression and nerve signal attenuation were compared for iMSDE and the proposed OC-MDSDE in 7 subjects. Sagittal 3D TSE images were acquired with iMSDE ($TE_{prep} = 58$ ms; b = 40 s/mm^2; $m_1 = 5{,}870$ mT ms^2/m) and with OC-MDSDE ($TE_{prep} = 58$ ms; b = 450 s/mm^2; $m_1 = 5870$ mT ms^2/m). Nerve-to-vessel signal ratios were measured for the 7 subjects for iMSDE and the proposed OC-MDSDE. Ratios were obtained from the average signal within regions of interest in the tibial nerve and in the popliteal vein, drawn on an axial plane above the knee. The popliteal vein runs immediately next to the tibial nerve in the knee region and can obscure the visualization of the nerve in some regions. Although there are multiple vessel segments that can affect the nerve delineation, the popliteal vein was selected as a region of interest (ROI) in order to standardize the nerve-to-vessel signal ratio determination across subjects.

Signal-to-noise ratio (SNR) in the tibial nerve and in the gastrocnemius muscle was measured in 2 subjects from ROIs drawn on images acquired with iMSDE and with OC-MDSDE with the sequence parameters described above. SNR was measured from the mean tissue signal intensity within an ROI and from the standard deviation of pure noise in the corresponding region (32). Pure noise images were acquired separately, with all RF pulses and gradients turned off. Experimentally measured SNR values for OC-MDSDE were compared to expected SNR values for this method. Expected SNR for OC-MDSDE was derived from the diffusion-induced signal loss relative to iMSDE resulting from the additional diffusion weighting (applied perpendicularly to the nerve axis) in OC-MDSDE relative to iMSDE. For the computation of the expected SNR for OC-MDSDE, the diffusion constants used were 0.001 and $0.00135\,mm^2/s$ (33–35) for nerve and muscle, respectively.

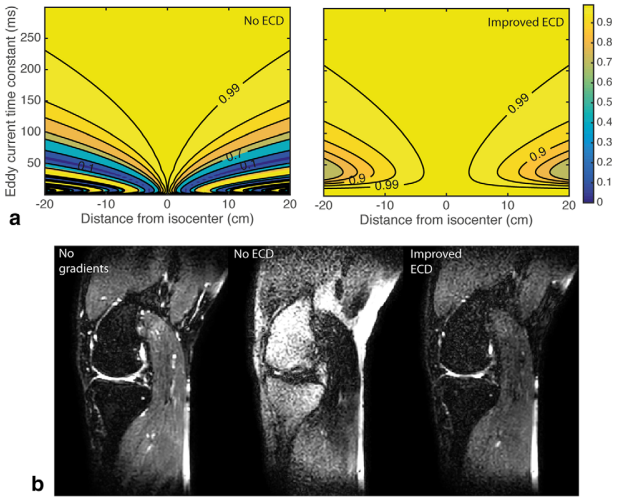

FIG. 2. Eddy current effects and desensitization (ECD) in OC-MDSDE. (**a**) Simulated water signal as a function of eddy current time constant and distance from the isocenter shown using no ECD (left) and using improved ECD (right). (**b**) In vivo images of a healthy subject's knee showing the proposed method with no active gradients (left), with $G_{pp} = 44$ mT/m and no ECD (center), and with $G_{pp} = 44$ mT/m and improved ECD (right). Artifacts result when no ECD is used, but are avoided with improved ECD.

Qualitative Evaluation and Statistical Testing of In Vivo Results

Image quality was evaluated by means of a 5-point visual grading of the source images acquired with iMSDE and with the proposed OC-MDSDE by two board-certified radiologists with 15 (J.S.K) and 1.5 (E.K.) years of experience. Evaluations from each reader were performed blindly and independently from one another in order to assess interobserver reproducibility. The evaluated criteria consisted of: 1) vessel signal appearing in nerve regions; 2) nerve signal homogeneity; 3) visibility of small nerve branches within gastrocnemius muscle; 4) contrast of nerve to surrounding muscle; and 5) overall artifacts. In the 5-point grading scale, a grade of 1 was the most favorable and a grade of 5 was the least favorable. The scores used in the 5-point grading varied among criteria and are specified in Supporting Table S1.

The average grades corresponding to iMSDE and OC-MDSDE were statistically compared for each criterion using a paired *t* test with a significance level of 5%. Interobserver agreement was determined by measuring the intraclass correlation coefficients (ICCs) for the two methods for each criterion. The ICC model was based on a two-way random comparison of absolute agreement type and the coefficients were computed with a significance level of 5%.

RESULTS

Simulations and In Vivo Assessment of Eddy Current Effects

Figure 2a shows simulations of eddy-current–induced signal loss, underlining the importance of ECD in the FC-DSDE component of OC-MDSDE preparation. In the case when no ECD is included in the simulations, phase accumulation from small eddy current time constants, that exceeds 2π (phase wrapping), leads to sharp nonmonotonic signal fluctuations with increasing distance from the isocenter. With increasing eddy current time constants, the variation of signal remains pronounced, but takes on a monotonic behavior. When the improved ECD is included in the simulations, a milder monotonic signal variation results with increasing distance from the isocenter. Thus, the simulation results demonstrate the benefit of the improved ECD presented in this work. The corresponding in vivo results in Figure 2b show that OC-MDSDE without ECD leads to large artifacts (center image), and that such artifacts are removed when ECD is used (right-most image).

In Vivo Assessment of Motion Sensitivity

Figure 3 shows the need of flow compensation when using iMSDE with b-values in the order of 200 s/mm^2. iMSDE applied parallel to the direction of the nerve (iMSDE$_{\parallel}$) with $m_1 = 11{,}740$ mT ms^2/m and $b = 215$ s/mm^2 results in motion-induced signal loss and image degradation, most notably close to the pulsating artery. The flow-compensated version of iMSDE$_{\parallel}$, FC-DSDE$_{\parallel}$, is shown to yield no motion-induced artifacts when similar sensitivity to motion (in transverse directions) is achieved. FC-DSDE applied perpendicular to the nerve (FC-DSDE$\perp$) is also shown to generate no artifacts as well as to yield higher nerve signal than FC-DSDE$_{\parallel}$.

In Vivo Evaluation of Vessel Signal Suppression

A comparison of the vessel signal suppression capability of the iMSDE, FC-DSDE, and OC-MDSDE sequences is shown in Figure 4. iMSDE with m_1- and b-values at the upper limit of the range commonly used for vessel suppression applications results in leftover vessel signal. FC-DSDE applied perpendicular to the nerve with a moderate b-value reduces vessel signal, but, compared to iMSDE, shows returning vessel signal with flow in the direction of the nerve. OC-MDSDE with moderate m_1- and b-values reduces more vessel signal than iMSDE and FC-DSDE.

Figure 5 provides a qualitative comparison of the relative attenuation of vessel and nerve signal obtained with iMSDE and OC-MDSDE in 5 subjects (remaining 2 subjects not shown). In both sagittal and coronal views, a superior reduction of vessel signal is observed with OC-MDSDE compared to iMSDE. Moreover, for all subjects, the nerve-to-vessel signal ratios measured in the tibial nerve and in the popliteal vein were higher for OC-MDSDE compared to iMSDE. The mean nerve-to-vessel signal ratio of the 7 subjects was 0.40 ± 0.17 for iMSDE and 0.63 ± 0.37 for OC-MDSDE. Measured nerve-to-vessel signal ratios for all subjects are listed in Supporting Table S2.

The mean SNR measured in 2 subjects was 30 ± 2 in nerve and 16 ± 4 in muscle for iMSDE. For OC-MDSDE, the mean measured SNR was 22 ± 2 in nerve and 10 ± 1 in muscle. Measured SNR for OC-MDSDE translates to an observed SNR loss of 27% in nerve and of 38% in muscle compared to iMSDE. The mean expected SNR for OC-MDSDE, computed as the mean SNR measured for iMSDE multiplied by an exponential comprising the b-

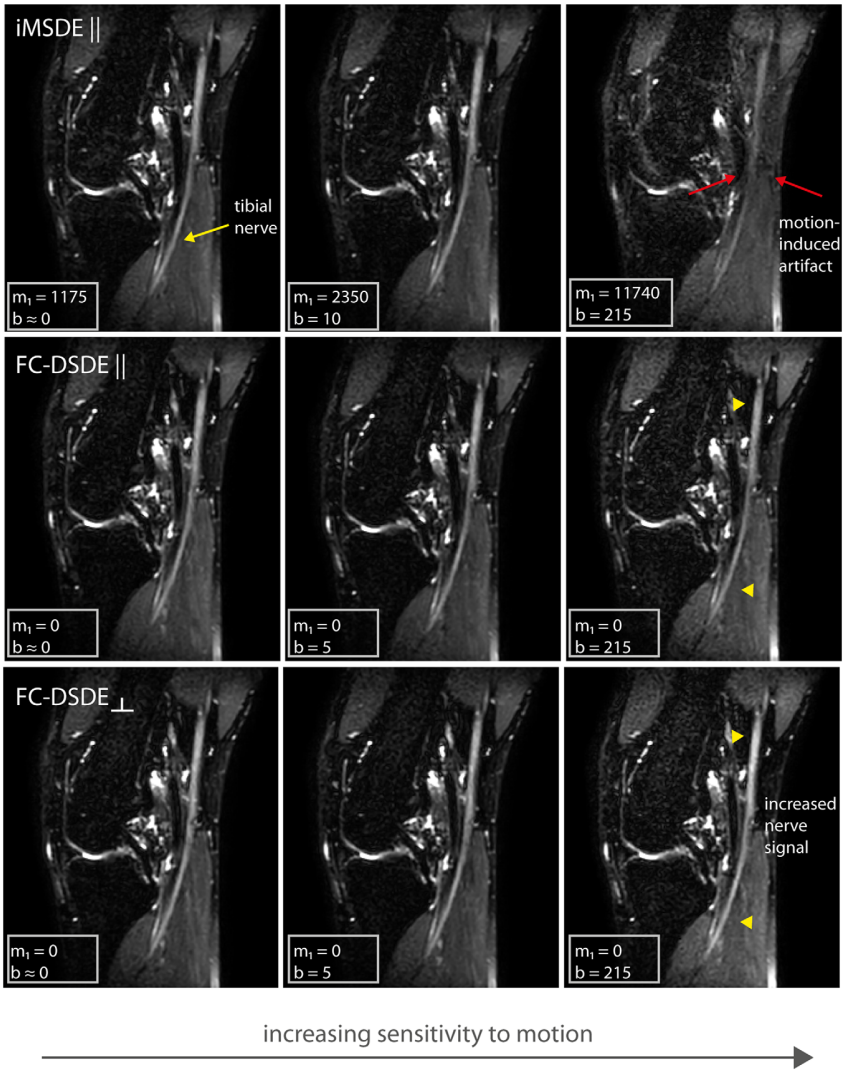

FIG. 3. Comparison of the motion sensitivity of iMSDE and FC-DSDE preparation-based imaging. Columns show images of the tibial nerve in the knee acquired sagittally with increasing gradient strength and constant preparation duration. Top row: iMSDE parallel to the direction of the nerve (iMSDE$_{\parallel}$) at increasing m_1- and b-values. Middle row: FC-DSDE parallel to the direction of the nerve (FC-DSDE$_{\parallel}$) at $m_1 = 0$ and increasing b-values. Bottom row: FC-DSDE perpendicular to the direction of the nerve (FC-DSDE$\perp$) at $m_1 = 0$ and increasing b-values. Motion-induced signal loss is observed when reaching sufficiently large m_1 with iMSDE, most severely near the pulsating artery (red arrows in top row). Using flow compensation prevents the appearance of motion-induced artifacts at increasing motion sensitivity (middle and bottom rows) and maximizes nerve signal when the diffusion gradients are oriented perpendicular to the nerve (yellow pointers in middle and bottom rows). m_1 is given in units of mT ms^2/m and b in s/mm^2.

value difference between the two methods and the diffusion constant for a given tissue, was found to be 20 ± 2 in nerve and 9 ± 3 in muscle, yielding an expected diffusion-induced SNR loss of 33% in nerve and 44% in muscle with OC-MDSDE method compared to iMSDE.

Qualitative Evaluation and Statistical Testing of In Vivo Results

Visual grading of image quality observed with iMSDE and OC-MDSDE resulted in statistically significant reduction of vessel signal appearing in nerve regions when using OC-MDSDE ($P < 0.001$). Homogeneity of nerve signal and the visibility of small nerve branches within the gastrocnemius muscle were not significantly affected by the choice of vessel suppression method ($P = 0.83$ and $P = 0.69$, respectively). Furthermore, nerve contrast was observed to be significantly higher with OC-MDSDE compared to iMSDE ($P = 0.015$), and no significant difference in overall artifacts was found between the two methods ($P = 1$). The average ICC for interobserver agreement was 0.91 for iMSDE and 0.95 for OC-MDSDE. Assigned grades and the corresponding ICC measures are listed in Supporting Table S3.

DISCUSSION

The current work presents a combined motion- (flow) and diffusion-sensitized preparation for suppressing vessel signal that is not effectively suppressed by conventional flow sensitization methods and that is particularly advantageous for imaging anatomical structures with specific diffusion properties and geometrical orientations. The proposed orthogonally combined motion- and diffusion-sensitized driven equilibrium (OC-MDSDE) is demonstrated here for high near isotropic resolution imaging of peripheral nerves in the lower extremities using a 3D TSE readout.

Vessel signal compromising nerve visualization is often encountered in peripheral nerve imaging (24). Similar signal intensities of nerves and adjacent vessels can lead to the reduction of nerve contrast and thus to obstruction of nerve delineation. In order to overcome this problem, vessel signal intensity can be manipulated

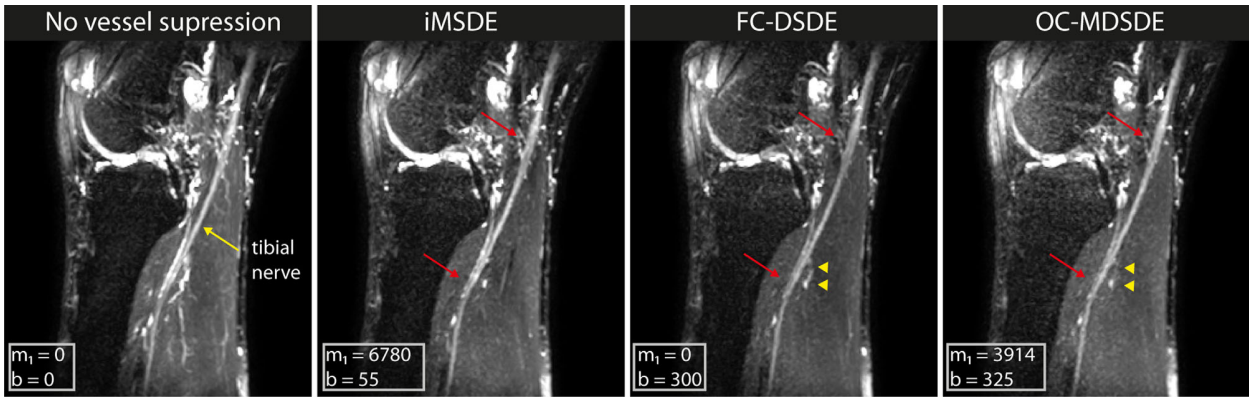

FIG. 4. Comparison of vessel signal suppression capabilities. Sagittal images of the tibial nerve in the knee acquired with three preparation modules utilizing different attenuation mechanisms show the suppression of vessel signal that can be achieved with each method. Images acquired with no sensitizing gradients show vessel contamination. Images obtained with flow-sensitive iMSDE using high m_1 show an effective reduction in vessel signal, but incomplete suppression of slow flow (red arrows). FC-DSDE perpendicular to the direction of the nerve using a moderate b-value results in better suppression of slow flow (red arrows), but shows some vessel signal recovery parallel to the nerve (yellow pointers). OC-MDSDE with moderate m_1- and b-values shows signal reduction both of vessels orthogonal and parallel to the nerve (red arrows, yellow pointers). m_1 is given in units of mT ms^2/m and b in s/mm^2.

to appear higher or lower than that of nerve signal. Whereas both the increase and the reduction of vessel signal can help recover nerve contrast (36), suppression of vessel signal can lead to better nerve visualization. Flow-sensitized–driven equilibrium, such as iMSDE, is frequently used with 3D TSE in peripheral nerve imaging for vessel signal suppression (16–18). The moderate m_1-values normally used in iMSDE for vessel suppression often result in incomplete suppression of slow flow, but using large m_1-values in iMSDE can result in motion-induced artifacts and image degradation (25). FC-DSDE has been used in diffusion applications to overcome motion-induced signal loss and has been shown to give artifact-free images using moderate b-values (37,38). In peripheral nerve imaging, FC-DSDE has the additional advantage that, attributed to the high microstructural anisotropy of nerves, diffusion weighting can be used to attenuate vessel signal without a considerable attenuation of nerve signal. Moreover, second and higher gradient moments can contribute to the vessel suppression capability of FC-DSDE. Given the persistent problem of residual vessel signal in peripheral nerve imaging, it is desirable to use all vessel-attenuating mechanisms available in a driven equilibrium preparation to maximize vessel signal suppression. The proposed OC-MDSDE preparation utilizes flow and diffusion sensitization and exploits the vessel-nerve geometry of peripheral nerves in the extremities to achieve this goal.

As can be expected for the FC-DSDE component of the preparation, which has a weak inherent robustness to eddy currents attributed to the monopolar nature of its sensitizing gradients (39), simulation and experimental results show that ECD needs to be incorporated into this component when using the high gradient strengths required to attenuate vessel signal (for a fixed preparation duration). Moreover, the four-lobe ECD gradient prepulse approach used in this work showed to be highly robust to eddy-current–induced signal loss for a wide range of eddy current time constants and at considerable displacements from the magnet isocenter. The inadequacy of the application of iMSDE with the high gradient strengths (25) necessary for moderate b-values is apparent from in vivo results showing motion-induced artifacts. The need for flow compensation in this situation is therefore obvious. The importance of choosing the right diffusion-sensitizing direction in FC-DSDE is apparent at even moderate b-values. In agreement with the much smaller radial than axial diffusivity observed in nerve tissue (34,35), in vivo results show that considerable nerve signal is preserved when diffusion-sensitizing gradients are applied perpendicular, as opposed to parallel, to the long axis of the nerve. This effect can be expected to be greater at larger b-values.

Although FC-DSDE using moderate b-values alone can significantly reduce signal of vessels with slow and fast flow, iMSDE with low m_1 still poses an advantage if applied parallel to the direction of fast flow. In the extremities, large veins and arteries with fast flow tend to follow a similar course as the nerves, whereas smaller vessels with slow flow tend to be more tortuous and run in a large variety of directions. Therefore, the intrinsic combination of $iMSDE_{\parallel}$ and $FC\text{-}DSDE_{\perp}$ in OC-MDSDE results in a powerful reduction of vessel signal from both fast and slow flow with minimal attenuation of nerve signal.

In vivo results presented in this work reproducibly demonstrate the superior vessel-suppressing capability of the proposed OC-MDSDE preparation compared to the conventional iMSDE preparation. When using b-values as high as 450 s/mm^2, the nerve-to-vessel signal ratio measured for OC-MDSDE is observed to be higher in all 7 cases, despite the inevitable SNR loss. Moreover, a significant reduction of vessel signal and a significant increase of nerve contrast are observed with the proposed method. It is important to note that vessel signal suppression with either of the presented methods is not complete. Depending on the imaged anatomical region and on the subject, vessel flow characteristics may vary and may result in a variable amount of vessel signal

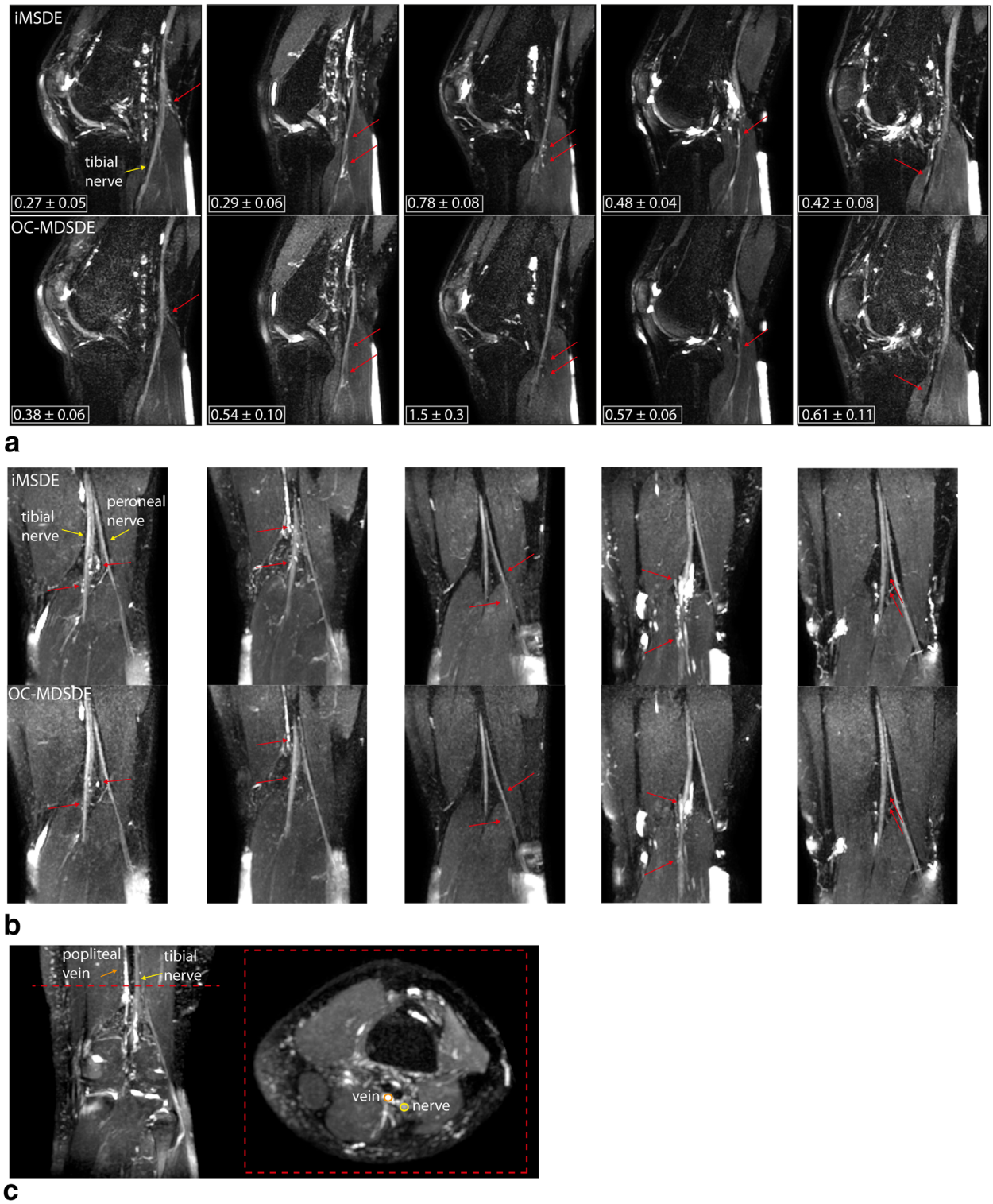

FIG. 5. Comparison of the vessel signal suppression capability and nerve-to-vessel signal ratios of iMSDE and OC-MDSDE in 5 subjects. (**a**) Sagittal images of the knee showing the tibial nerve in 5 healthy subjects shown in columns compare the effects on vessel and nerve signal resulting from utilizing iMSDE ($m_1 = 5{,}870$; $b = 40$) and OC-MDSDE ($m_1 = 5{,}870$; $b = 450$) preparations. The yellow arrow points to the tibial nerve, and the red arrows point to residual vessel signal. (**b**) Coronal reformats showing the tibial and peroneal nerves and, similarly to (**a**), further displaying the effects on vessel and nerve signal resulting from the two preparation methods. (**c**) Coronal and axial maximum intensity projection reformats illustrating the generation of ROIs, carried out on the axial plane denoted by the red dashed line. Yellow and orange circles illustrate ROIs drawn on the tibial nerve and on the popliteal vein, respectively. Measured nerve-to-vessel signal ratios for iMSDE and OC-MDSDE are given in gray boxes in the bottom-left corners of (**a**). For all 5 subjects, OC-MDSDE yields larger reduction of vessel signal as well as a higher nerve-to-vessel ratio than iMSDE. m_1 is given in units of mT ms^2/m and b in s/mm^2.

suppression. Alternatively, vessel signal suppression in subjects having vessels with faster flow may yield images showing minimal differences between the two preparation methods (iMSDE and OC-MDSDE).

Although demonstrated here for the lower extremities, high-resolution imaging of the nerves in the upper extremities (eg, in the wrist) would also benefit from the application of the proposed method. As presently shown, the high near isotropic resolution acquisition with 3D TSE allows the generation of 3D reformats on all three orthogonal planes as well as of oblique multiplanar reconstructions, where the nerve trajectory can be precisely followed.

It is important to further note that a preparation duration of roughly 60 ms was chosen for all measurements. The preparation duration impacts signal attenuation by T_2 decay, which is crucial for achieving the desired contrast between the nerves and the surrounding muscle (17,18). Moreover, in OC-MDSDE, the preparation duration also limits the diffusion weighting that can be realized using a fixed gradient strength. A preparation duration of OC-MDSDE of approximately 60 ms was therefore found here to generate the desired contrast and allow the realization of the desired b-value using maximal gradient strength.

The proposed OC-MDSDE approach has also a number of limitations. First, the inevitable overall signal loss that results from using high b-values may be undesirable in scans with low SNR. Nonetheless, moderate b-values can still be used in these situations at the cost of inferior vessel signal suppression. Second, although the choice of preparation duration and of diffusion weighting in the proposed method satisfactorily reduce muscle and vessel signals, T_2 decay and diffusion weighting in OC-MDSDE do not suppress signal of stationary fluid, which might obscure nerve visualization. Third, although the improved ECD presented here was shown to suffice, eddy current effects may still be visible when implementing the proposed method on different imaging systems with distinct eddy current properties, especially if high b-values are used. Fourth, the presently proposed method was not directly compared to the reversed fast imaging with steady state free precession (PSIF) technique, which has been previously used for vessel suppression in peripheral nerves imaging of the extremities (19,40). Fifth, the presently shown insensitivity of OC-MDSDE to motion, as introduced by the flow compensation, is limited. At sufficiently high b-values, motion-induced phase errors from higher-order motion may become significant and lead to artifacts. However, maintaining a moderate b-value, as done in this study, should reduce such effects. Last, it should be noted that with increasing b-values, the weighting of the OC-MDSDE module deviates from pure T_2 weighting and has also a diffusion-weighting component.

CONCLUSION

We have shown that the proposed OC-MDSDE preparation can provide improved vessel signal suppression and high nerve signal in imaging of peripheral nerves in the extremities. Namely, the combination of flow and diffusion sensitization in OC-MDSDE is shown to effectively reduce signal in vessels having both fast and slow flow without significantly affecting the nerve signal while being robust against eddy currents and motion. Moreover, OC-MDSDE has been shown to be readily compatible with high-resolution readouts, such as 3D TSE, and is therefore highly advantageous in high-resolution applications, such as imaging of peripheral nerves in the extremities.

ACKNOWLEDGMENT

The authors thank Jinnan Wang for helpful discussions and support.

REFERENCES

1. Ahlawat S, Carrino JA. Three-dimensional imaging of lower limb neuropathies. Semin Musculoskelet Radiol 2015;19:168–178.
2. Chhabra A, Andreisek G, Soldatos T, et al. MR neurography: past, present, and future. AJR Am J Roentgenol 2011;197:583–591.
3. Chhabra A, Rozen S, Scott K. Three-dimensional MR neurography of the lumbosacral plexus. Semin Musculoskelet Radiol 2015;19:149–159.
4. Cho Sims G, Boothe E, Joodi R, Chhabra A. 3D MR neurography of the lumbosacral plexus: obtaining optimal images for selective longitudinal nerve depiction. Am J Neuroradiol 2016;37:2158–2162.
5. Cox B, Zuniga JR, Panchal N, Cheng J, Chhabra A. Magnetic resonance neurography in the management of peripheral trigeminal neuropathy: experience in a tertiary care centre. Eur Radiol 2016;26:3392–3400.
6. Freund W, Brinkmann A, Wagner F, et al. MR neurography with multiplanar reconstruction of 3D MRI datasets: an anatomical study and clinical applications. Neuroradiology 2007;49:335–341.
7. Viallon M, Vargas MI, Jlassi H, Lövblad KO, Delavelle J. High-resolution and functional magnetic resonance imaging of the brachial plexus using an isotropic 3D T2 STIR (Short Term Inversion Recovery) SPACE sequence and diffusion tensor imaging. Eur Radiol 2008;18:1018–1023.
8. Vargas MI, Viallon M, Nguyen D, Beaulieu JY, Delavelle J, Becker M. New approaches in imaging of the brachial plexus. Eur J Radiol 2010; 74:403–410.
9. Howe FA, Filler AG, Bell BA, Griffiths JR. Magnetic resonance neurography. Magn Reson Med 1992;28:328–338.
10. Filler AG, Maravilla KR, Tsuruda JS. MR neurography and muscle MR imaging for image diagnosis of disorders affecting the peripheral nerves and musculature. Neurol Clin 2004;22:643–682.
11. Andreisek G, Burg D, Studer A, Weishaupt D. Upper extremity peripheral neuropathies: role and impact of MR imaging on patient management. Eur Radiol 2008;18:1953–1961.
12. Takahara T, Hendrikse J, Yamashita T, et al. Diffusion-weighted MR neurography of the brachial plexus: feasibility study. Radiology 2008; 249:653–660.
13. Zhang Z, Song L, Meng Q, et al. Morphological analysis in patients with sciatica: a magnetic resonance imaging study using three-dimensional high-resolution diffusion-weighted magnetic resonance neurography techniques. Spine 2009;34:E245–E250.
14. Kuntz C, Blake L, Britz G, et al. Magnetic resonance neurography of peripheral nerve lesions in the lower extremity. Neurosurgery 1996; 39:750–756; discussion, 756–757.
15. Filler AG, Tsurda JS, Richards TL, Howe FA, inventors. University Of Washington, assignee. Image neurography and diffusion anisotropy imaging. US Patent 08/028,795. October 1, 1996.
16. Kasper JM, Wadhwa V, Scott KM, Rozen S, Xi Y, Chhabra A. SHINKEI—a novel 3D isotropic MR neurography technique: technical advantages over 3DIRTSE-based imaging. Eur Radiol 2015;25:1672–1677.
17. Yoneyama M, Nakamura M, Okuaki T, et al. High-Resolution 3D Volumetric Nerve-Sheath Weighted RARE Imaging (3D SHINKEI). In Proceedings of the 19th Annual Meeting of ISMRM, Montreal, Canada, 2011. p. 2721.
18. Yoneyama M, Takahara T, Kwee TC, Nakamura M, Tabuchi T. Rapid high resolution MR neurography with a diffusion-weighted pre-pulse. Magn Reson Med Sci 2013;12:111–119.
19. Chhabra A, Soldatos T, Subhawong TK, et al. The application of three-dimensional diffusion-weighted PSIF technique in peripheral nerve imaging of the distal extremities. J Magn Reson Imaging 2011; 34:962–967.

20. Wang J, Yarnykh VL, Hatsukami T, Chu B, Balu N, Yuan C. Improved suppression of plaque-mimicking artifacts in black-blood carotid atherosclerosis imaging using a multislice motion-sensitized driven-equilibrium (MSDE) turbo spin-echo (TSE) sequence. Magn Reson Med 2007;58:973–981.
21. Zhu C, Graves MJ, Yuan J, Sadat U, Gillard JH, Patterson AJ. Optimization of improved motion-sensitized driven-equilibrium (iMSDE) blood suppression for carotid artery wall imaging. J Cardiovasc Magn Reson 2014;16:61.
22. Fan Z, Sheehan J, Bi X, Liu X, Carr J, Li D. 3D noncontrast MR angiography of the distal lower extremities using flow-sensitive dephasing (FSD)-prepared balanced SSFP. Magn Reson Med 2009;62:1523–1532.
23. Sheehan JJ, Fan Z, Davarpanah AH, et al. Nonenhanced MR angiography of the hand with flow-sensitive dephasing-prepared balanced SSFP sequence: initial experience with systemic sclerosis. Radiology 2011;259:248–256.
24. Chhabra A, Zhao L, Carrino JA, et al. MR neurography: advances. Radiol Res Pract 2013;2013:809568.
25. Wang J, Yarnykh VL, Yuan C. Enhanced image quality in black-blood MRI using the improved motion-sensitized driven-equilibrium (iMSDE) sequence. J Magn Reson Imaging 2010;31:1256–1263.
26. Absil J, Denolin V, Metens T. Diffusion-weighted balanced-FFE imaging using eddy-current compensation. In Proceedings of the 15th Annual Meeting of ISMRM, Berlin, Germany, 2007. p. 12.
27. Obara M, Kuroda K, Wang J, et al. Comparison between two types of improved motion-sensitized driven-equilibrium (iMSDE) for intracranial black-blood imaging at 3.0 tesla. J Magn Reson Imaging 2014;40: 824–831.
28. Gibbs SJ, Johnson CS, Jr. A PFG NMR experiment for accurate diffusion and flow studies in the presence of eddy currents. J Magn Reson 1991;93:395–402.
29. Bernstein MA, King KF, Zhou XJ. Handbook of MRI Pulse Sequences. London: Elsevier; 2004.
30. Guo J, Meakin JA, Jezzard P, Wong EC. An optimized design to reduce eddy current sensitivity in velocity-selective arterial spin labeling using symmetric BIR-8 pulses. Magn Reson Med 2015;73: 1085–1094.
31. Cervantes B, Bauer JS, Zibold F, et al. Imaging of the lumbar plexus: Optimized refocusing flip angle train design for 3D TSE. J Magn Reson Imaging 2016;43:789–799.
32. Dietrich O, Raya JG, Reeder SB, Reiser MF, Schoenberg SO. Measurement of signal-to-noise ratios in MR images: influence of multichannel coils, parallel imaging, and reconstruction filters. J Magn Reson Imaging 2007;26:375–385.
33. Simon NG, Lagopoulos J, Gallagher T, Kliot M, Kiernan MC. Peripheral nerve diffusion tensor imaging is reliable and reproducible. J Magn Reson Imaging 2016;43:962–969.
34. Sinha S, Sinha U, Edgerton VR. In vivo diffusion tensor imaging of the human calf muscle. J Magn Reson Imaging 2006;24:182–190.
35. Hooijmans MT, Damon BM, Froeling M, et al. Evaluation of skeletal muscle DTI in patients with duchenne muscular dystrophy. NMR Biomed 2015;28:1589–1597.
36. Zhang Z, Meng Q, Li Z, Pan B, Regatte RR, Schweitzer ME. Simultaneous visualization of nerves and vessels of the lower extremities using magnetization-prepared susceptibility weighted magnetic resonance imaging at 3.0 T. Neurosurgery 2012;70:1–7.
37. Liu H, Zhou Z, Wang J, Chen S, Niranjan B, Yuan C. Time-efficient diffusion-weighted black blood imaging based on iMSDE. In Proceedings of the 22nd Annual Meeting of ISMRM, Milan, Italy, 2014. p. 2532.
38. Schakel T, Hoogduin H, Philippens M. In vivo high resolution, undistorted diffusion weighted imaging using DSDE-TFE. In Proceedings of the 22nd Annual Meeting of ISMRM, Milan, Italy, 2014. p. 668.
39. Reese TG, Heid O, Weisskoff RM, Wedeen VJ. Reduction of eddy-current-induced distortion in diffusion MRI using a twice-refocused spin echo. Magn Reson Med 2002;49:177–182.
40. Lee PP, Chalian M, Bizzell C, et al. Magnetic resonance neurography of common peroneal (fibular) neuropathy. J Comput Assist Tomogr 2012;36:455–461.

SUPPORTING INFORMATION

Additional supporting information can be found in the online version of this article.

Table S1. Description of criterion-specific scores used in 5-point visual grading of iMSDE and OC-MDSDE methods
Table S2. Nerve-to-vessel signal ratios measured for 7 subjects in the tibial nerve and in the popliteal vein
Table S3. Interobserver visual grading and ICCs of in vivo results obtained with iMSDE and OC-MDSDE in 7 healthy subjects

5.3 Journal Publication III: Isotropic Resolution Diffusion Tensor Imaging of Lumbosacral and Sciatic Nerves Using a Phase-Corrected Diffusion-Prepared 3D Turbo Spin Echo

The publication entitled *Isotropic Resolution Diffusion Tensor Imaging of Lumbosacral and Sciatic Nerves Using a Phase-Corrected Diffusion-Prepared 3D Turbo Spin Echo* was published in Magnetic Resonance in Medicine (ISSN: 1522-2594). The manuscript was authored by Barbara Cervantes, Anh T. Van, Dominik Weidlich, Hendrik Kooijman, Andreas Hock, Ernst J. Rummeny, Alexandra Gersing, Jan S. Kirschke, and Dimitrios C. Karampinos.

Abstract

Purpose

To perform in vivo isotropic-resolution diffusion tensor imaging (DTI) of lumbosacral and sciatic nerves with a phase-navigated diffusion-prepared (DP) 3D turbo spin echo (TSE) acquisition and modified reconstruction incorporating intershot phase-error correction and to investigate the improvement on image quality and diffusion quantification with the proposed phase correction.

Methods

Phase-navigated DP 3D TSE included magnitude stabilizers to minimize motion and eddy-current effects on the signal magnitude. Phase navigation of motion-induced phase errors was introduced before readout in 3D TSE. DTI of lower back nerves was performed in vivo using 3D TSE and single-shot echo planar imaging (ss-EPI) in 13 subjects. Diffusion data were phase-corrected per k_z plane with respect to T_2-weighted data. The effects of motion-induced phase errors on DTI quantification was assessed for 3D TSE and compared with ss-EPI.

Results

Non–phase-corrected 3D TSE resulted in artifacts in diffusion-weighted images and overestimated DTI parameters in the sciatic nerve (mean diffusivity [MD] = 2.06 ± 0.45). Phase correction of 3D TSE DTI data resulted in reductions in all DTI parameters (MD = 1.73 ± 0.26) of statistical significance ($P \leq 0.001$) and in closer agreement with ss-EPI DTI parameters (MD = 1.62 ± 0.21).

Conclusion

DP 3D TSE with phase correction allows distortion-free isotropic diffusion imaging of lower back nerves with robustness to motion-induced artifacts and DTI quantification errors.

Author Contributions

(i) The first author alone: programmed the magnetic resonance pulse sequence (propriety hardware and software from Philips Medical Systems (Best, The Netherlands)); implemented the fitting routine used for data analysis (MATLAB and Statistics Toolbox Release 2016b, The MathWorks, Inc., Natick, Massachusetts, United States); implemented the post-processing routine used for data analysis (Diffusion Imaging in Python (Dipy) [69]); performed all experiments (in vivo magnetic resonance measurements); performed the data post-processing; and performed the data analysis. (ii) With the help and consultation of the coauthors, the first author: designed the experiment; implemented the image reconstruction using MATLAB and Statistics Toolbox; performed the statistical data analysis; and wrote the manuscript.

FULL PAPER

Magnetic Resonance in Medicine 00:00–00 (2018)

Isotropic Resolution Diffusion Tensor Imaging of Lumbosacral and Sciatic Nerves Using a Phase-Corrected Diffusion-Prepared 3D Turbo Spin Echo

Barbara Cervantes,[1]* Anh T. Van,[2] Dominik Weidlich,[1] Hendrick Kooijman,[3] Andreas Hock,[3] Ernst J. Rummeny,[1] Alexandra Gersing,[1] Jan S. Kirschke,[4] and Dimitrios C. Karampinos[1]

Purpose: To perform in vivo isotropic-resolution diffusion tensor imaging (DTI) of lumbosacral and sciatic nerves with a phase-navigated diffusion-prepared (DP) 3D turbo spin echo (TSE) acquisition and modified reconstruction incorporating intershot phase-error correction and to investigate the improvement on image quality and diffusion quantification with the proposed phase correction.

Methods: Phase-navigated DP 3D TSE included magnitude stabilizers to minimize motion and eddy-current effects on the signal magnitude. Phase navigation of motion-induced phase errors was introduced before readout in 3D TSE. DTI of lower back nerves was performed in vivo using 3D TSE and single-shot echo planar imaging (ss-EPI) in 13 subjects. Diffusion data were phase-corrected per k_z plane with respect to T_2-weighted data. The effects of motion-induced phase errors on DTI quantification was assessed for 3D TSE and compared with ss-EPI.

Results: Non–phase-corrected 3D TSE resulted in artifacts in diffusion-weighted images and overestimated DTI parameters in the sciatic nerve (mean diffusivity [MD] $= 2.06 \pm 0.45$). Phase correction of 3D TSE DTI data resulted in reductions in all DTI parameters (MD $= 1.73 \pm 0.26$) of statistical significance ($P \leq 0.001$) and in closer agreement with ss-EPI DTI parameters (MD $= 1.62 \pm 0.21$).

Conclusion: DP 3D TSE with phase correction allows distortion-free isotropic diffusion imaging of lower back nerves with robustness to motion-induced artifacts and DTI quantification errors. **Magn Reson Med 000:000–000, 2018. © 2018 The Authors Magnetic Resonance in Medicine published by Wiley Periodicals, Inc. on behalf of International Society for Magnetic Resonance in Medicine. This is an open access article under the terms of the Creative Commons Attribution NonCommercial License, which permits use, distribution and reproduction in any medium, provided the original work is properly cited and is not used for commercial purposes.**

Key words: magnetic resonance neurography; peripheral nerves MRI; diffusion prepared turbo spin echo; motion-induced phase errors; body diffusion; lumbar plexus

INTRODUCTION

MR imaging of proximal and peripheral nerves, denoted MR neurography (MRN), has been emerging as a more accurate and noninvasive alternative to nerve conduction evaluation in the diagnosis of nerve disorders (1,2). Moreover, it has been shown that morphological MRN alone can be insufficient in identifying nerve injury and that quantitative MRN can be helpful for a more precise diagnosis (3–5). Diffusion tensor imaging (DTI) has been leading as a prominent technique to assess disease in human proximal and peripheral nerves (6–9) due to its capability to provide functional microstructural information of nerve fibers (10,11) and thus lead to a more accurate diagnosis of nerve lesion compared with conventional T_2-weighted morphological imaging (12,13).

In a regime where high resolution is necessary to image small nerves with complex geometries, diffusion-weighted-imaging (DWI) methods are in general challenged in their ability to provide sufficient SNR and to circumvent geometric distortions and chemical shift artifacts of the conventionally used 2D single-shot echo planar imaging (ss-EPI). While reliable in DWI and DTI of anatomies with less strict resolution requirements, conventional 2D ss-EPI becomes, in isotropic resolution diffusion imaging of proximal and peripheral nerves, highly susceptible to distortion artifacts resulting from eddy currents and off-resonance effects (7). Furthermore, in DTI, resolution limitations characteristic of ss-EPI also impose restrictions on the ability to accurately provide quantitative information of nerves having small diameters. Available alternatives to ss-EPI for DWI and DTI for reduced geometric distortion and chemical shift artifacts include multishot EPI, readout-segmented EPI and single-shot turbo spin echo techniques (14–17), which have been in part applied in imaging of nerves in the

[1]Department of Diagnostic and Interventional Radiology, Klinikum rechts der Isar, Technical University of Munich, Munich, Germany.

[2]Institute of Medical Engineering (IMETUM), Technical University of Munich, Garching, Germany.

[3]Philips Healthcare, Hamburg, Germany.

[4]Department of Diagnostic and Interventional Neuroradiology, Klinikum rechts der Isar, Technical University of Munich, Munich, Germany.

Grant sponsor: Philips Healthcare; Grant sponsor: the European Research Council (ERC) under the European Union's Horizon 2020 research and innovation programme; Grant number: 637164 — iBack — ERC-2014-STG.

*Correspondence to: Barbara Cervantes, M.S., Department of Diagnostic and Interventional Radiology, Klinikum rechts der Isar, Technical University of Munich, Ismaninger Str. 22, 81675 Munich, Germany.
E-mail: b.cervantes@tum.de

Received 24 August 2017; revised 7 December 2017; accepted 14 December 2017

DOI 10.1002/mrm.27072
Published online 00 Month 2018 in Wiley Online Library (wileyonlinelibrary.com).

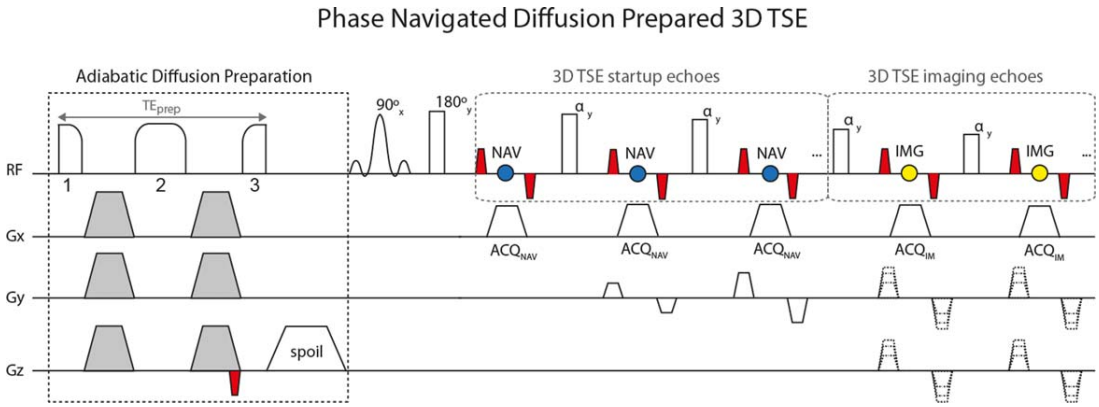

FIG. 1. Pulse sequence diagram of phase-navigated DP 3D TSE. The adiabatic diffusion preparation uses a modified BIR-4 pulse configuration for minimizing transmit B_1 effects, where 1 indicates excitation, 2 refocusing, and 3 restoration of signal. Diffusion gradients (gray) are placed symmetrically around the refocusing segment of the pulse and a gradient is placed after the restoration segment for spoiling residual transverse magnetization. A magnitude-stabilizing gradient (red) is placed before signal restoration and later balanced in the 3D TSE readout. In the 3D TSE readout, startup echoes are acquired as navigator echoes (blue) using k_y phase encoding only. Imaging echoes (yellow) are acquired with k_y and k_z phase encoding.

body (18–22). Specifically, turbo spin echo (TSE) or fast spin echo (FSE) techniques have been shown to yield high resolution diffusion imaging totally free of distortion and chemical shift artifacts in a broad range of body applications (16,23–26).

Among TSE methods used for DWI and DTI, diffusion-prepared (DP) multishot TSE can be combined with a 3D readout to achieve isotropic resolution, which is necessary in diffusion imaging of proximal and peripheral nerves for its feasibility of curved and multiplanar reconstructions and volume reformatting (27,28). Multishot TSE in DWI and DTI is, however, highly susceptible to intershot phase inconsistencies induced by motion and eddy currents (29–31), which have been shown to affect both the magnitude and the phase of the diffusion-weighted TSE signal (32). It has been demonstrated that for DP single-shot TSE the use of dephasing and rephasing gradients, here referred to as magnitude stabilizers, can minimize effects induced by motion and eddy currents on the signal magnitude, without the need to address effects on the signal phase (16).

In DP multishot TSE, however, motion-induced phase variations between shots lead to artifacts and diffusion quantification errors, requiring careful considerations on the signal phase. In recent work, DP 3D TSE with magnitude stabilizers has been applied in vivo using velocity compensation (23,33,34), effectively reducing motion-induced phase errors and resulting in reasonable image quality and diffusion quantification. More recent work has also shown, however, that the residual motion-induced phase in DP 3D TSE not accounted for by magnitude stabilizers can still lead to artifacts and considerable quantification errors, and that these can be eliminated by measuring and correcting the motion-induced intershot phase variations (30).

The purpose of the present work is to perform in vivo isotropic resolution imaging of lumbosacral and sciatic nerves by developing a phase-navigated DP 3D TSE acquisition and a modified reconstruction incorporating intershot phase error correction. Using the developed acquisition and reconstruction, the current work intends to investigate the improvement on image quality and on diffusion quantification accuracy resulting from the proposed phase correction.

METHODS

Sequence Development

The proposed phase-navigated DP 3D TSE sequence (Fig. 1) consists of an adiabatic diffusion preparation followed by a phase-navigated 3D TSE readout. The adiabatic diffusion preparation has for an RF component a modified four-segment B_1-insensitive rotation (BIR-4) pulse, previously shown to increase robustness against B_0 and transmit B_1 effects when applied for T_2 preparation (35–38). The modified RF configuration consists of a BIR-4 pulse with gaps between the three RF components added to fit diffusion-sensitizing gradients, where the total duration of the BIR-4 RF pulse without gaps is 10 ms. The frequency sweep of the RF pulse has an amplitude of 3700 Hz. Diffusion-sensitizing gradients (shown in gray in Fig. 1) use the traditional Stejskal-Tanner design to minimize the preparation duration TE_{prep}. A magnitude-stabilizing gradient (shown in red in Fig. 1) is placed after diffusion sensitization and before the signal tip-up and is later balanced in the 3D TSE readout (16,32).

The developed phase-navigated 3D TSE readout consists of the acquisition of navigator echoes followed by the acquisition of imaging echoes. The acquisition of navigator echoes takes place during the pseudo steady state (PSS) stage of 3D TSE, in which the initial echoes (referred to as startup echoes) are not acquired for imaging purposes to avoid signal oscillations from echo to echo (39–41). Navigator echoes are only phase-encoded along the k_y direction. Therefore, the y-direction resolution of the resulting navigator image depends on the number of startup echoes of the echo train. To increase the y-direction resolution of the navigator image and hence the capability to capture more complex motion-

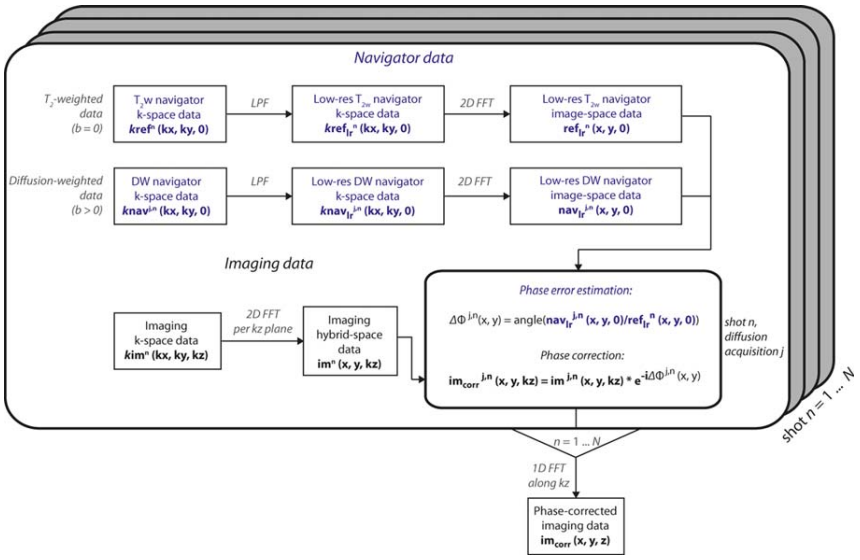

FIG. 2. Phase correction and reconstruction in phase-corrected DP 3D TSE. The phase error map $\Delta\phi$ j,n (x, y) for each individual diffusion acquisition *j* and shot *n* is estimated from the low-resolution navigator data in image space, where the T_2-weighted (b = 0) data are used as a reference. Phase correction per shot and per diffusion acquisition of the imaging data with the estimated phase error is done voxel-wise in the hybrid space (x, y, k_z). Corrected imaging data are then reconstructed along k_z to obtain the final image. LPF, low-pass filter; FFT, fast Fourier transform.

induced phase errors, sensitivity encoding (SENSE) can be used. The imaging sequence acquires one full k_z plane in each echo train (also referred to as shot).

Phase Correction and Image Reconstruction

A schematic representation of the implemented phase correction and reconstruction routine is shown in Figure 2. For each shot *n*, acquired T_2-weighted (T_{2w}) navigator k-space data $k\text{ref}^n$ (kx, ky, 0) and diffusion-weighted (DW) navigator k-space data $k\text{nav}^{j,n}$ (kx, ky, 0), where *j* denotes the diffusion acquisition, are first low-pass filtered using a 2D triangular window, because only the low spatial frequencies of the signal phase are expected to be affected by motion. After 2D reconstruction of low-resolution T_{2w} k-space data $k\text{ref}_{lr}^n$ (kx, ky, 0) and DW navigator k-space data $k\text{nav}_{lr}^{j,n}$ (kx, ky, 0), the phase of the low-resolution DW navigator image-space data per diffusion acquisition *j*, $\text{nav}_{lr}^{j,n}$ (x, y, 0), is compared, per shot *n*, to the phase of the low-resolution T_{2w} navigator image-space data ref_{lr}^n (x, y, 0), which are used as a reference. The estimated phase difference map $\Delta\phi^{j,n}$ (x, y) is then used on the 2D-reconstructed imaging hybrid-space data $\text{im}^{j,n}$ (x, y, kz) to correct for diffusion-acquisition- and shot-dependent phase by means of complex multiplication. The 1D reconstruction along k_z, equivalently across all shots, results in the final phase-corrected imaging data im_{corr} (x, y, z).

In Vivo Measurements

Thirteen healthy volunteers (mean age, 29 ± 5 years; 8 males, 5 females) participated in the study. The study was approved by the local institutional review board and conducted in accord with the committee for human research. All subjects gave written informed consent before their participation in the study. All acquisitions were performed on a 3T whole-body Philips scanner (Philips Ingenia, Best, The Netherlands) with maximum gradient amplitude of 45 mT/m and maximum slew rate of 200 T/m/s, in conjunction with a 16-channel torso coil and the built-in-table 12-channel posterior coil. The subjects were positioned supine and the coil was centered at the pelvic bone to cover the sacral plexus and the sciatic nerves. Survey scans were acquired in all coronal, sagittal, and axial planes. A coronal T_2-weighted 3D TSE scan was included to have a visual reference of the nerves in further planning (42). The imaging volumes of all following scans were aligned to the spinal cord and positioned to cover the lumbar 5 (L5) nerve as well as the sciatic nerve after the junction of the L5 and sacral S1, S2, and S3 nerve branches.

DTI with DP 3D TSE was performed coronally in all subjects with the following readout sequence parameters: field of view (FOV) = 400 × 400 × 50 mm^3; acquisition voxel = 2.5 × 2.5 × 2.5 mm^3; reconstruction voxel = 0.78 × 0.78 × 1.25 mm^3; repetition time/echo time (TR/TE) = 1500/35 ms; echo train length = 53; duration of diffusion preparation TE_{prep} = 32 ms; effective echo time including diffusion preparation (43) TE_{eff} = 53 ms; fat suppression using spectral adiabatic inversion recovery; number of signal averages = 2 using phase cycling for removal of free induction decay artifacts; parallel imaging using SENSE with reduction factor R = 3 (in the right–left phase encoding direction); b-values = 0,400 s/mm^2; number of diffusion directions = 6; and total scan duration = 11 min 58 s. Phase encoding for navigator echoes was carried out for k_y symmetrically around $k_y = 0$, with $k_{y\ max} = \pm 6$ (SENSE factor of 3), and without k_z phase encoding.

DTI with diffusion-weighted ss-EPI (DW ss-EPI) was performed to serve as a reference and to better allow the assessment of motion-induced effects on DTI data acquired with DP 3D TSE. DW ss-EPI was performed axially in all subjects and coronally in one subject. Due to severe distortions (see below), coronal DW ss-EPI data were acquired for qualitative and visualization purposes only. Axial and coronal DW ss-EPI were planned to cover the same anatomy as coronal DP 3D TSE and axial DW ss-EPI was matched in FOV in the feet–head direction and in the isotropic voxel size to coronal DP 3D TSE. Axial DW ss-EPI scans used the following sequence parameters: field of view = 400 × 250 × 250 mm^3;

acquisition voxel = $2.5 \times 2.5 \times 2.5\,mm^3$; reconstruction voxel = $0.93 \times 0.93 \times 2.50\,mm^3$; slice gap = 0 mm; TR/TE = 23832/47 ms; fat suppression using spectral adiabatic inversion recovery; number of signal averages = 3; partial Fourier encoding with factor = 0.74; parallel imaging using SENSE with reduction factor R = 2 (in the right–left phase encoding direction); b-values = 0,400 s/mm^2; number of diffusion directions = 6; and total scan duration = 9 min 8 s.

Coronal DW ss-EPI scans used the following sequence parameters: field of view = $400 \times 400 \times 50\,mm^3$; acquisition voxel = $2.5 \times 2.5 \times 2.5\,mm^3$; reconstruction voxel = $0.93 \times 0.93 \times 2.50\,mm^3$; slice gap = 0 mm; TR/TE = 3346/58 ms; fat suppression using spectral adiabatic inversion recovery; number of signal averages = 3; partial Fourier encoding with factor = 0.74; parallel imaging using SENSE with reduction factor R = 2 (in the right–left phase encoding direction); b-values = 0,400 s/mm^2; number of diffusion directions = 6; and total scan duration = 1 min 17 s.

DTI scans with DP 3D TSE and axial DW ss-EPI were additionally carried out three times for five of the 13 subjects with identical sequence parameters for demonstration of repeatability.

An additional 3D two-echo gradient echo sequence using a bipolar (non–fly-back) readout was included to generate a B_0 map with the following sequence parameters: field of view = $250 \times 400 \times 250\,mm^3$; acquisition voxel = $3.2 \times 3.2 \times 3.2\,mm^3$; reconstruction voxel = $0.78 \times 0.78 \times 3.20\,mm^3$; TR/TE1/$\Delta$TE = 6.6/1.14/0.8 ms; flip angle = 3°; six acquired echoes; number of signal averages = 1; and total scan duration = 1 min 4 s. The B_0 map was generated using the vendor's algorithm for performing water-fat separation of the two-echo gradient-echo data (44).

DTI Analysis

Axial b = 400 DW ss-EPI data were registered to axial b = 0 DW ss-EPI data using an affine transformation (45,46) to minimize geometric distortions produced by eddy currents.

Diffusion tensors were estimated from DTI data acquired with DP 3D TSE and with axial DW ss-EPI using an own nonlinear fitting routine implemented in MATLAB and Statistics Toolbox Release 2016b (The MathWorks, Inc., Natick, MA). DTI parameters were computed from the derived eigenvalues and projections of the primary eigenvectors of DTI DP 3D TSE data on the coronal and sagittal planes were generated for visualization of preferential nerve direction.

For each subject, the sciatic nerve at the level of the greater sciatic foramen was identified on iso-diffusion-weighted images (iso-DWIs) generated from axial DW ss-EPI data and axially reformatted DP 3D TSE data. Sagittal views were used to locate the left and right sciatic nerves at the height of the base of the femoral head in the feet–head direction. The selected feet–head location relative to the femoral head was then confirmed using coronal views, in which the left–right locations of both nerves were then found. Given the locations noted in feet–head and left–right directions, axial views were finally used to localize both left and right sciatic nerves in all three orthogonal dimensions. Supporting Figure S1, which is available online, illustrates the localization procedure described above.

Regions of interest (ROIs) were independently drawn by two MR researchers with 3.5 (B.C.) and 3 (D.W.) years of experience in performing evaluations of quantitative MR neurographic studies. ROIs were drawn on the localized left and right sciatic nerves on axial DW ss-EPI data and on axially reformatted DP 3D TSE data using 5 mm averages in the feet–head direction using MATLAB and Statistics Toolbox Release 2016b (The MathWorks, Inc., Natick, MA). To minimize quantification errors caused by distortions in DW ss-EPI, the extraction of DTI metrics was carried out on the sciatic nerve after the junction of the L5, S1, and S2 nerves, where distortions in DW ss-EPI images were the least severe. Axial, radial, and mean diffusivity (AD, RD, and MD, respectively) maps and fractional anisotropy (FA) maps were masked independently with the ROIs obtained by the two readers and mean values were extracted.

Statistical Analysis

To assess the effect of motion-induced phase errors and their correction in DP 3D TSE, mean AD, RD, MD, and FA values measured by a single reader (B.C.) were compared across subjects for DP 3D TSE with and without phase correction using a paired t-test with a significance level of 0.05. To further assess robustness to motion and thus the DTI-quantification accuracy of phase-corrected DP 3D TSE, the DTI metrics measured with phase-corrected DP 3D TSE were compared with those measured with DW ss-EPI using a paired t-test with the same properties as specified above.

Interobserver agreement for the extracted DTI metrics was determined by measuring the intraclass correlation coefficients (ICC) for DP 3D TSE with and without phase correction and for DW ss-EPI. The ICC model was based on a two-way random comparison of absolute agreement type and the coefficients were computed with a significance level of 0.05. ICCs were first computed per DTI parameter and per method and then averaged for each method.

Repeatability measurements in five subjects were submitted to a similar extraction of mean DTI-parameter values by a single reader (B.C.). For assessing variance between measurements per DTI metric and per method across scans, root-mean-square errors (RMSE) and root-mean-square error coefficients of variation (RMSCV) (47) were computed for AD, RD, MD, and FA values measured with DP 3D TSE, phase-corrected DP 3D TSE and DW ss-EPI. Interscan agreement of the DTI metrics measured with the three methods was determined by computing ICC values with the model described above.

RESULTS

Effects of Phase Errors on Image Reconstruction and Diffusion Quantification

Estimated phase error maps from DP 3D TSE data shown in the top row of Figure 3 show motion-induced phase

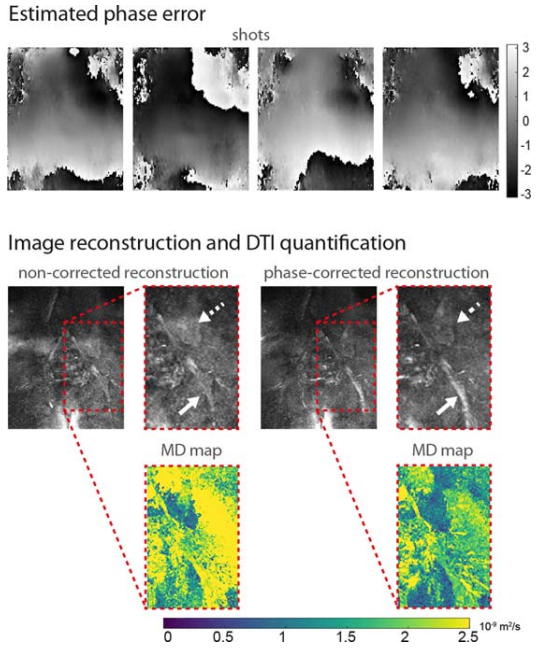

FIG. 3. Effects of motion-induced phase errors in DP 3D TSE on image reconstruction and diffusion quantification. **Top**: The estimated phase error maps (shown in radians) across four shots of a single diffusion acquisition show motion-induced phase variations in the frequency and phase encoding directions that are inconsistent across shots. **Middle**: The reconstruction of the corresponding diffusion data without correction of motion-induced phase errors results in incorrect signal buildup due to ghosting in the slice encoding direction (dotted arrows) as well as in signal loss in numerous regions, including a large loss of signal in the sciatic nerve (full arrows). The incorporation of phase error correction in the image reconstruction results in the elimination of ghosting artifacts and in the restoration of nerve signal. **Bottom**: Corresponding MD maps show the overestimation of diffusivity values in nerve and muscle caused by uncorrected motion-induced phase errors.

that varies across shots of the 3D TSE readout, highlighting the fundamental importance of phase correction in DP 3D TSE. The corresponding reconstructed DWI shown in the middle row demonstrates the effect of the resulting intershot phase inconsistencies on the signal magnitude when no phase correction is performed, which can take the form of through-slice ghosting as well as of in-plane signal loss (dotted arrow and solid arrow, respectively). The reconstructed phase-corrected image shows the reduction of ghosting and restoration of signal. Derived MD maps in the bottom row display a large overestimation of mean diffusivity values in DP 3D TSE without phase correction and a remarkable restoration of MD values of nerve and muscle to within literature-reported ranges when phase correction is performed. Supporting Figure S2 further illustrates the effects of motion-induced phase errors on image reconstruction and diffusion quantification in two additional subjects.

DTI and Statistical Analysis

DTI parameters estimated by a single reader from data acquired with DP 3D TSE and with DW ss-EPI are summarized in Table 1. Diffusion quantification of DP 3D TSE data with and without phase correction resulted in a statistically significant reduction in AD, RD, MD, and FA values in the sciatic nerve after phase correction was performed ($P \leq 0.001$ for AD, RD, and MD; $P = 0.02$ for FA). The estimation of DTI metrics from DW ss-EPI data compared with phase-corrected DP 3D TSE data resulted in significantly different AD and MD values ($P = 0.03$ and $P = 0.02$, respectively) and in nonsignificant differences in RD and FA values ($P = 0.11$ and $P = 0.27$, respectively).

Table 1
DTI Parameters of the Sciatic Nerve Measured With DP 3D TSE With and Without Phase Correction and DW ss-EPI[a]

	3D TSE				
	Uncorr[a]	Phase corr[b]	ss-EPI[c]	P^{ab}	P^{bc}
AD	3.40 ± 1.04	2.67 ± 0.36	2.47 ± 0.31	0.001[b]	0.03[b]
MD	2.06 ± 0.45	1.73 ± 0.26	1.62 ± 0.21	<0.001[b]	0.02[b]
RD	1.39 ± 0.29	1.27 ± 0.27	1.20 ± 0.22	<0.001[b]	0.11
FA	0.52 ± 0.11	0.48 ± 0.10	0.45 ± 0.09	0.02[b]	0.27

[a]Mean ± SD values within the sciatic nerve measured in 13 healthy subjects in left and right locations. Diffusivity values shown in units of 10^{-9} m^2/s. P^{ab} denotes the P value comparing DP 3D TSE with and without phase correction and P^{bc} denotes the P value comparing phase-corrected DP 3D TSE and DW ss-EPI.
[b]$P < 0.05$.

Mean values of the DTI metrics measured by the two readers for DP 3D TSE, phase-corrected DP 3D TSE, and DW ss-EPI resulted in average intraclass correlation coefficients (ICC) of 0.98, 0.97, and 0.94, respectively.

Repeatability errors and interscan agreement from data acquired in five subjects over three scans with DP 3D TSE and DW ss-EPI are summarized in Table 2. Phase error correction of repeated DTI measurements with DP 3D TSE resulted in reduced RMSE in AD, MD, and FA, and in unaltered errors in RD. Similarly, RMSCV decreased for all DTI metrics except for RD, where it increased by one percentage point. RMSE and RMSCV values for DW ss-EPI were smaller than those for DP 3D TSE. ICC values of all DTI metrics for DP 3D TSE, phase-corrected DP 3D TSE and DW ss-EPI were 0.97, 0.98 and 0.99, respectively.

Table 2
Repeatability Errors and Interscan Agreement for DTI Parameters of the Sciatic Nerve Measured With DP 3D TSE With and Without Phase Correction and DW ss-EPI

	3D TSE		
	Uncorr	Phase corr	ss-EPI
AD	0.48 [11%]	0.20 [7%]	0.15 [6%]
MD	0.19 [8%]	0.13 [7%]	0.10 [6%]
RD	0.15 [11%]	0.15 [12%]	0.12 [10%]
FA	0.07 [15%]	0.06 [14%]	0.05 [12%]
ICC	0.97	0.98	0.99

RMSE, RMSCV, and intraclass correlation coefficients (ICC) computed for DTI parameters measured in left and right locations in the sciatic nerve in five healthy subjects over three identical scans. RMSE in units of (10^{-9} m^2/s) for AD, RD, and MD and in (-) for FA. RMSCV in percentage units for all metrics.

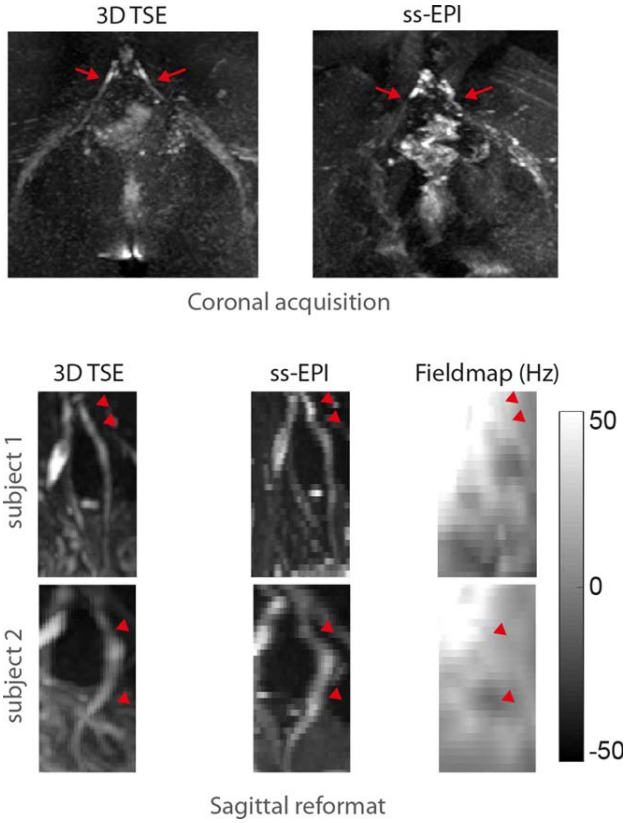

FIG. 4. Geometric distortions in ss-EPI. **Top**: Coronal ss-EPI acquisition shows severe geometric distortions of the S1 nerve in the phase encoding (left–right) direction compared with 3D TSE (red arrows). **Bottom**: The sagittal reformat of axially acquired ss-EPI shows severe distortions of the L5 nerve in the phase encoding (anterior–posterior) direction compared with sagittally reformatted 3D TSE (red pointers). A B_0 fieldmap shows that distortions in ss-EPI occur in regions with large B_0 inhomogeneity. Moreover, imperfect slice profiles in the axial ss-EPI acquisition lead to artificial increase and/or decrease of the nerve signal as compared to the 3D TSE.

Distortions in Isotropic Resolution Imaging with ss-EPI

Figure 4 shows distortion problems encountered in nerve imaging with ss-EPI. The coronal acquisition of the full field of view containing the lower spine and the sciatic nerves with ss-EPI results in large distortions of the S1 nerves and milder distortions of the sciatic nerves in the phase encoding (left–right) direction compared with 3D TSE, making coronal ss-EPI an unacceptable acquisition method for this anatomical region. Axial acquisition with ss-EPI, shown in sagittal reformats for two healthy subjects (bottom rows), considerably reduces distortions but still results in distortions of the nerve course in the anterior–posterior direction compared with 3D TSE in regions with considerable B_0 inhomogeneity.

Isotropic Resolution DWI and DTI with Phase-Corrected DP 3D TSE

Figures 5 to 7 illustrate DTI results of isotropic resolution imaging of sacral nerves with DP 3D TSE. Iso-DWIs of the sacral plexus and of the sciatic nerve in coronal,

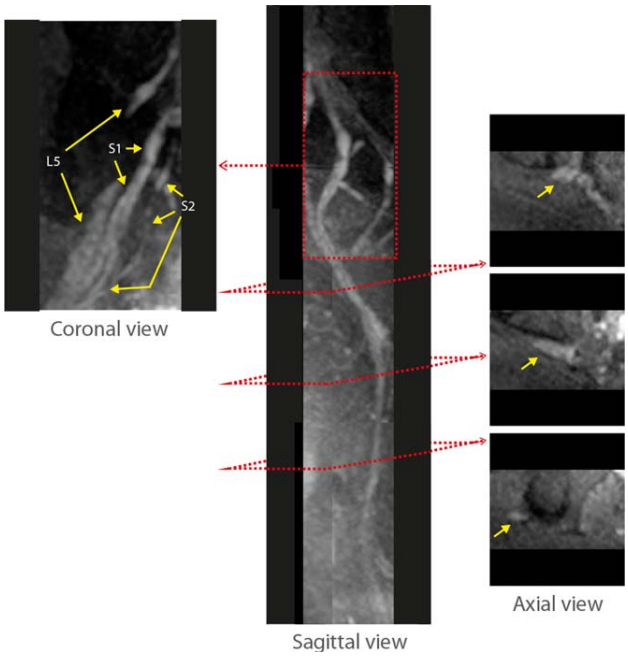

FIG. 5. Isotropic resolution multiview DWI of lumbosacral and sciatic nerves with phase-corrected DP 3D TSE. Coronal, sagittal, and axial views of the iso-DWI acquired with isotropic resolution phase-corrected DP 3D TSE show L5, S1, and S2 nerve roots and branches as well as the postjunction sciatic nerve running down in the pelvic region.

sagittal and axial views in Figure 5 clearly show the roots, ganglia and branches of the L5, S1, and S2 nerves as well as the course of the sciatic nerve. Coronal and sagittal views show the inner structure of the L5 and S1 nerve branches and axial cross sections show the fibular

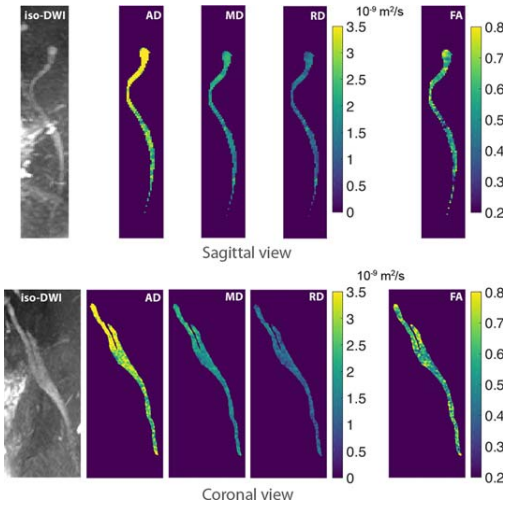

FIG. 6. Isotropic resolution DTI of the sciatic nerve with phase-corrected DP 3D TSE. Sagittal and coronal reformats of iso-DWI and corresponding DTI maps obtained with phase-corrected DP 3D TSE illustrate diffusion parameters along the sciatic nerve before and after the junction of the L5 and S1 nerves. High diffusivity values toward the ganglia of the L5 and S1 nerves are believed to be caused by the presence of CSF fluid.

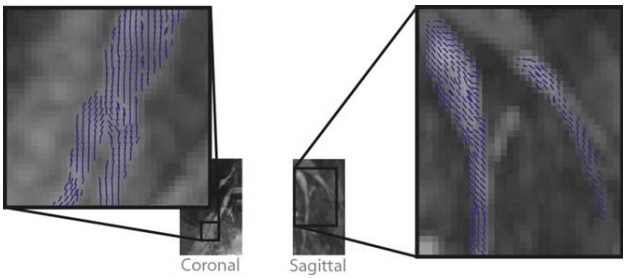

FIG. 7. Primary diffusion tensor eigenvector projections of lumbosacral nerves with phase-corrected DP 3D TSE. Primary diffusion tensor eigenvector projections on coronal and sagittal planes for two healthy subjects superimposed on their corresponding iso-DWIs generated with phase-corrected DP 3D TSE depict the course of the L5, S1, and S2 nerves before the junction into the sciatic nerve.

and tibial components of the sciatic nerve near the junction of the lumbosacral nerves. Figure 6 illustrates the advantage of multiview reformatting of isotropic 3D data for diffusion quantification. Sagittal and coronal views of the S1 and sciatic nerves acquired with phase-corrected DP 3D TSE show DTI parameter maps of the full course of the nerves. Moreover, Figure 7 shows the primary diffusion tensor eigenvector projections on the coronal and sagittal planes for sacral nerves in two healthy subjects. The shown eigenvectors clearly depict the trajectory of the nerves and highlight the internal orientation of small nerve branches.

DISCUSSION

The current work presents distortion-minimized isotropic resolution DTI results of the lower back nerves by proposing a phase-navigated DP 3D TSE acquisition. In the proposed technique, magnitude modulation induced by motion and eddy currents is minimized with magnitude stabilizers and intershot phase variations induced by motion are measured with navigator echoes before the 3D TSE readout. Because the navigator acquisition uses the existing PSS echoes, its inclusion in the 3D TSE readout does not lead to any change in sequence parameters or to a longer acquisition duration. A phase correction and reconstruction routine is also presented, in which phase measured from navigator data is used to phase-correct diffusion data during image reconstruction.

DTI can be a highly valuable tool in diagnostic MRN, but DWI of nerves in the body presents a challenging problem for a wide range of acquisition methods (30,35,48). ss-EPI meeting coverage and resolution requirements necessary for imaging of nerves in the body can be particularly vulnerable to geometric distortions and chemical shift artifacts (49), challenging its application in DTI measurements of nerves in the body. Single-shot TSE techniques circumvent the problems encountered with ss-EPI (50–52) but are still limited to 2D and nonisotropic resolution due to SAR restrictions (52–56). Given the complex geometry of the nervous system in the human body, 3D isotropic imaging is highly desirable for DTI measurements in this anatomy (57,58). DTI with TSE using a (multishot) 3D readout allows the acquisition of isotropic resolution diffusion images but requires the additional handling of intershot phase errors induced by motion, which interfere with the correct reconstruction of diffusion images when they are inconsistent across shots.

Present results showing the spatial distribution of estimated phase errors corresponding to multiple shots in DW data acquired in vivo with DP 3D TSE demonstrate that phase induced by motion varies from shot to shot. Moreover, the observation of ghosting artifacts and the loss of signal in the associated reconstructed images confirm that motion-induced phase errors lead to a notable deterioration of image quality when diffusion data are not phase-corrected. Phase correction of the diffusion data is shown to yield reconstructed images with minimal ghosting and with largely recovered signal. The corruption of DTI eigenvalues by phase errors is emphasized in the presented MD maps derived from DP 3D TSE DTI data reconstructed with and without phase correction. Uncorrected motion-induced phase errors produce largely overestimated and thus physically meaningless MD values while MD values derived from phase-corrected data agree with previously reported values (7,9).

Significant reductions in the mean values of all DTI metrics measured in the sciatic nerves in 13 subjects with phase-corrected DP 3D TSE compared with non–phase-corrected DP 3D TSE demonstrate the corruption of the measured, uncorrected diffusion signals by motion, because it is expected that the phase induced by bulk motion during diffusion encoding will lead to the artificial attenuation of diffusion signals and consequently to the overestimation of diffusivity.

Moreover, the reduced standard deviations in all DTI metrics observed in DP 3D TSE measurements with phase correction indicates that the robustness to motion provided by phase correction leads to more consistent diffusion quantification. The closer agreement of mean and standard deviation values observed in phase-corrected DP 3D TSE DTI metrics to those observed with DW ss-EPI indicates that motion robustness in the multishot method approaches that in the single-shot method. Significant differences in AD and MD metrics measured with phase-corrected DP 3D TSE compared with DW ss-EPI highlight residual small differences in the quantification performances of the two methods. In the case of phase-corrected DP 3D TSE, higher values can originate from types of motion that the proposed technique is still insensitive to, such as motion-induced phase variation in the k_z encoding direction or from microscopic contractions within single imaging voxels that lead to intravoxel dephasing. In the case of DW ss-EPI, remaining geometric distortions and/or slice profile effects can lead to the incorrect estimation of the DTI metrics in the sciatic nerves. Trends of higher diffusivity metrics measured with DW TSE-based methods compared with DW ss-EPI have already been observed (23,59,60).

DTI repeatability results further support the above arguments. Reductions in RMSE and RMSCV in all sciatic-nerve DTI metrics obtained with DP 3D TSE after phase correction show that the proposed phase correction leads to lower variance within and across subjects

and across scans. Although of similar order, smaller RMSE and RMSCV values in DW ss-EPI compared with phase-corrected DP 3D TSE indicate that the multishot method might still be in part more sensitive to motion than the single-shot method. We emphasize that the proposed phase-navigation and phase-correction technique is meant to increase robustness to motion and is not expected to achieve complete motion insensitivity as DW ss-EPI.

AD results were most vulnerable to motion effects compared with other DTI metrics. Motion-induced phase errors can affect different diffusion directions differently. For example, when the motion-induced phase error induces a signal loss in only one diffusion direction, the affected direction becomes the direction of preferential diffusion, potentially also affecting AD. In contrast, FA values were observed to be least affected by motion. This finding is in agreement with previous reports that have shown that measurements of FA in peripheral nerves vary less significantly than other diffusivity values when different methods are used to estimate the metrics as well as across nerve locations (9).

In vivo results comparing images of lower back nerves acquired with 3D TSE and with ss-EPI show that severe distortions of the nerves in ss-EPI data make this acquisition method unsuitable for performing accurate measurements of DTI-derived parameters in the lumbosacral and sciatic nerves, where B_0 inhomogeneity can be present. DP 3D TSE is shown to provide distortion-free DWIs and DTI parameter maps in which individual nerves and their internal structure can be visualized and whose course can be clearly and accurately followed. It is further shown that isotropic-resolution DWIs and DTI parameter maps obtained with phase-corrected DP 3D TSE can be reformatted in all three orthogonal planes to inspect specific morphological and functional aspects.

The present study has several limitations. First, as any 3D acquisition technique, the proposed 3D TSE technique is associated with significantly longer scan times than the 2D ss-EPI due to the efficient k-space traversal of the EPI trajectory and the interleaving capability of 2D acquisitions. Second, regarding SNR efficiency, the proposed DP 3D TSE acquisition has lower SNR efficiency than DW ss-EPI, which poses a disadvantage for the proposed method. However, as suggested by the obtained results in the current study, DW ss-EPI is only expected to be suitable for DWI of nerves in the body where isotropic resolutions are not needed and where off-resonance does not lead to unacceptable geometric distortions and chemical shift artifacts. It is in cases of isotropic resolution requirements, as well as in imaging of anatomies where field inhomogeneity and the presence of fat signal are problematic and unavoidable, that the immunity to off-resonance of the proposed DP 3D TSE technique can become of superior value despite the compromise in SNR efficiency. A detailed SNR analysis comparing DP 3D TSE and DW ss-EPI was not performed in this work and would require further investigation.

Third, to be incorporated in the PSS stage preceding each echo-train readout in 3D TSE, navigator echoes in the proposed method are acquired without phase encoding along the k_z direction. This acquisition effectively results in a 2D navigator image that is the average of the 3D imaging volume along the z direction. Therefore, the proposed technique cannot resolve linear and higher order phase errors along the non–phase-encoded direction. However, translational motion along the non–phase-encoded direction, which results in spatially constant phase errors, can still be detected and corrected. The performance of the proposed phase correction technique, hence, depends on the spatial coverage and the severity of motion along the non–phase-encoded direction. For the application at hand, we have shown significant improvement in image quality and quantitative metrics when the phase correction was used on a slab thickness of 50 mm in the A–P direction in the pelvic area. Because the proposed navigator acquisition is to be obtained for free, without affecting the imaging acquisition, it is undoubtedly beneficial to incorporate the proposed navigation in every multishot DWI TSE sequence.

CONCLUSIONS

We have shown that the proposed phase-navigated DP 3D TSE acquisition and phase correction can provide DWIs and derived DTI metrics of lumbosacral and sciatic nerves with minimized motion-induced effects. Namely, the measurement of motion-induced phase in DP 3D TSE and its subsequent correction is shown to significantly reduce the motion-induced overestimation of diffusion tensor parameters as well as to remove artifacts from DWIs. The proposed DP 3D TSE method has been shown to provide distortion-free isotropic resolution DTI of lumbosacral and sciatic nerves.

ACKNOWLEDGMENTS

The authors thank Qinwei Zhang and Aart Nederveen for helpful discussions.

REFERENCES

1. Chhabra A, Andreisek G, Soldatos T, Wang KC, Flammang AJ, Belzberg AJ, Carrino JA. MR neurography: past, present, and future. AJR Am J Roentgenol 2011;197:583–591.
2. Thawait SK, Chaudhry V, Thawait GK, Wang KC, Belzberg A, Carrino JA, Chhabra A. High-resolution MR neurography of diffuse peripheral nerve lesions. AJNR Am J Neuroradiol 2011;32:1365–1372.
3. Bendszus M, Stoll G. Technology insight: visualizing peripheral nerve injury using MRI. Nat Clin Pract Neurol 2005;1:45–53.
4. Karppinen J, Malmivaara A, Tervonen O, Paakko E, Kurunlahti M, Syrjala P, Vasari P, Vanharanta H. Severity of symptoms and signs in relation to magnetic resonance imaging findings among sciatic patients. Spine (Phila Pa 1976) 2001;26:E149–E154.
5. Aota Y, Niwa T, Yoshikawa K, Fujiwara A, Asada T, Saito T. Magnetic resonance imaging and magnetic resonance myelography in the presurgical diagnosis of lumbar foraminal stenosis. Spine (Phila Pa 1976) 2007;32:896–903.
6. Kakuda T, Fukuda H, Tanitame K, et al. Diffusion tensor imaging of peripheral nerve in patients with chronic inflammatory demyelinating polyradiculoneuropathy: a feasibility study. Neuroradiology 2011; 53:955–960.
7. Karampinos DC, Melkus G, Shepherd TM, Banerjee S, Saritas EU, Shankaranarayanan A, Hess CP, Link TM, Dillon WP, Majumdar S. Diffusion tensor imaging and T2 relaxometry of bilateral lumbar nerve roots: feasibility of in-plane imaging. NMR Biomed 2013;26: 630–637.
8. Mathys C, Aissa J, Meyer Zu Horste G, Reichelt DC, Antoch G, Turowski B, Hartung HP, Sheikh KA, Lehmann HC. Peripheral

neuropathy: assessment of proximal nerve integrity by diffusion tensor imaging. Muscle Nerve 2013;48:889–896.
9. Simon NG, Lagopoulos J, Gallagher T, Kliot M, Kiernan MC. Peripheral nerve diffusion tensor imaging is reliable and reproducible. J Magn Reson Imaging 2016;43:962–969.
10. Alexander AL, Hasan K, Kindlmann G, Parker DL, Tsuruda JS. A geometric analysis of diffusion tensor measurements of the human brain. Magn Reson Med 2000;44:283–291.
11. Mori S, Zhang J. Principles of diffusion tensor imaging and its applications to basic neuroscience research. Neuron 2006;51:527–539.
12. Chhabra A, Thakkar RS, Andreisek G, Chalian M, Belzberg AJ, Blakeley J, Hoke A, Thawait GK, Eng J, Carrino JA. Anatomic MR imaging and functional diffusion tensor imaging of peripheral nerve tumors and tumorlike conditions. AJNR Am J Neuroradiol 2013;34: 802–807.
13. Naraghi AM, Awdeh H, Wadhwa V, Andreisek G, Chhabra A. Diffusion tensor imaging of peripheral nerves. Semin Musculoskelet Radiol 2015;19:191–200.
14. Holdsworth SJ, Skare S, Newbould RD, Bammer R. Robust GRAPPA-accelerated diffusion-weighted readout-segmented (RS)-EPI. Magn Reson Med 2009;62:1629–1640.
15. Porter DA, Heidemann RM. High resolution diffusion-weighted imaging using readout-segmented echo-planar imaging, parallel imaging and a two-dimensional navigator-based reacquisition. Magn Reson Med 2009;62:468–475.
16. Alsop DC. Phase insensitive preparation of single-shot RARE: application to diffusion imaging in humans. Magn Reson Med 1997;38: 527–533.
17. Wu W, Miller KL. Image formation in diffusion MRI: a review of recent technical developments. J Magn Reson Imaging 2017;46:646–662.
18. Manoliu A, Ho M, Piccirelli M, et al. Simultaneous multislice readout-segmented echo planar imaging for accelerated diffusion tensor imaging of the mandibular nerve: a feasibility study. J Magn Reson Imaging 2017;46:663–677.
19. Markvardsen LH, Vaeggemose M, Ringgaard S, Andersen H. Diffusion tensor imaging can be used to detect lesions in peripheral nerves in patients with chronic inflammatory demyelinating polyneuropathy treated with subcutaneous immunoglobulin. Neuroradiology 2016;58: 745–752.
20. Vaeggemose M, Pham M, Ringgaard S, Tankisi H, Ejskjaer N, Heiland S, Poulsen PL, Andersen H. Diffusion tensor imaging MR neurography for the detection of polyneuropathy in type 1 diabetes. J Magn Reson Imaging 2017;45:1125–1134.
21. Yamashita R, Isoda H, Arizono S, Furuta A, Ohno T, Ono A, Murata K, Togashi K. Selective visualization of pelvic splanchnic nerve and pelvic plexus using readout-segmented echo-planar diffusion-weighted magnetic resonance neurography: a preliminary study in healthy male volunteers. Eur J Radiol 2017;86:52–57.
22. Filli L, Piccirelli M, Kenkel D, Boss A, Manoliu A, Andreisek G, Bhat H, Runge VM, Guggenberger R. Accelerated magnetic resonance diffusion tensor imaging of the median nerve using simultaneous multislice echo planar imaging with blipped CAIPIRINHA. Eur Radiol 2016;26:1921–1928.
23. Zhang Q, Coolen BF, Versluis MJ, Strijkers GJ, Nederveen A. Diffusion-prepared stimulated-echo turbo spin echo (DPsti-TSE): an eddy current-insensitive sequence for three-dimensional high-resolution and undistorted diffusion-weighted imaging. NMR Biomed 2017;30: e3719–e3712.
24. Xie Y, Yu W, Fan Z, Nguyen C, Bi X, An J, Zhang T, Zhang Z, Li D. High resolution 3D diffusion cardiovascular magnetic resonance of carotid vessel wall to detect lipid core without contrast media. J Cardiovasc Magn Reson 2014;16:67.
25. Pipe JG. Motion correction with PROPELLER MRI: application to head motion and free-breathing cardiac imaging. Magn Reson Med 1999;42:963–969.
26. Zhou XJ, Leeds NE, McKinnon GC, Kumar AJ. Characterization of benign and metastatic vertebral compression fractures with quantitative diffusion MR imaging. AJNR Am J Neuroradiol 2002;23:165–170.
27. Chhabra A, Thawait GK, Soldatos T, Thakkar RS, Del Grande F, Chalian M, Carrino JA. High-resolution 3T MR neurography of the brachial plexus and its branches, with emphasis on 3D imaging. AJNR Am J Neuroradiol 2013;34:486–497.
28. Kasper JM, Wadhwa V, Scott KM, Rozen S, Xi Y, Chhabra A. SHINKEI--a novel 3D isotropic MR neurography technique: technical advantages over 3DIRTSE-based imaging. Eur Radiol 2015;25:1672–1677.
29. Van AT, Cervantes B, Kooijman H, Karampinos DC. Compensating for eddy current effects in motion-compensated diffusion-prepared TSE sequences. In Proceedings of the 25th Annual Meeting of ISMRM, Honolulu, Hawaii, USA, 2017. Abstract 3924.
30. Cervantes B, Van AT, Kooijman H, Ven Kvd, Hock A, Rummeny EJ, Kirschke JS, Karampinos DC. One-dimensional phase navigation of diffusion-weighted 3D TSE for high resolution musculoskeletal diffusion imaging. In Proceedings of the 25th Annual Meeting of ISMRM, Honolulu, Hawaii, USA, 2017. Abstract 3935.
31. Cho Sims G, Boothe E, Joodi R, Chhabra A. 3D MR neurography of the lumbosacral plexus: obtaining optimal images for selective longitudinal nerve depiction. AJNR Am J Neuroradiol 2016;37:2158–2162.
32. Van AT, Cervantes B, Kooijman H, Karampinos DC. Analysis of phase error effects in multishot diffusion-prepared turbo spin echo imaging. Quant Imaging Med Surg 2017;7:238–250.
33. Zhang Q, Cervantes B, Karampinos DC, Coolen BF, Nederveen AJ, Strijkers GJ. High resolution 3D diffusion imaging of carotid vessel wall using stimulated echo based diffusion prepared turbo spin echo sequence. In Proceedings of the 24th Annual Meeting of ISMRM, Singapore, Singapore, 2016. Abstract 959.
34. Cervantes B, Zhang Q, Ven Kvd, Kooijman H, Rummeny EJ, Haase A, Strijkers GJ, Kirschke JS, Nederveen AJ, Karampinos DC. High-resolution DTI of distal peripheral nerves using flow-compensated diffusion-prepared 3D TSE. In Proceedings of the 24th Annual Meeting of ISMRM, Singapore, Singapore, 2016. Abstract 4530.
35. Cervantes B, Weidlich D, Kooijman H, Rummeny EJ, Haase A, Kirschke JS, Karampinos DC. High-resolution DWI of the lumbar plexus using B1-insensitive velocity-compensated diffusion-prepared 3D TSE. In Proceedings of the 24th Annual Meeting of ISMRM, Singapore, Singapore, 2016. Abstract 4474.
36. Jenista ER, Rehwald WG, Chen EL, Kim HW, Klem I, Parker MA, Kim RJ. Motion and flow insensitive adiabatic T2 -preparation module for cardiac MR imaging at 3 Tesla. Magn Reson Med 2013;70:1360–1368.
37. Nezafat R, Ouwerkerk R, Derbyshire AJ, Stuber M, McVeigh ER. Spectrally selective B1-insensitive T2 magnetization preparation sequence. Magn Reson Med 2009;61:1326–1335.
38. Weidlich D, Schlaeger S, Kooijman H, Bornert P, Kirschke JS, Rummeny EJ, Haase A, Karampinos DC. T2 mapping with magnetization-prepared 3D TSE based on a modified BIR-4 T2 preparation. NMR Biomed 2017;30. doi: 10.1002/nbm.3773.
39. Hennig J, Weigel M, Scheffler K. Multiecho sequences with variable refocusing flip angles: optimization of signal behavior using smooth transitions between pseudo steady states (TRAPS). Magn Reson Med 2003;49:527-535.
40. Hennig J, Scheffler K. Hyperechoes. Magn Reson Med 2001;46:6–12.
41. Mugler JP III, Epstein FH, Brookeman JR. Shaping the signal response during the approach to steady state in three-dimensional magnetization-prepared rapid gradient-echo imaging using variable flip angles. Magn Reson Med 1992;28:165–185.
42. Cervantes B, Bauer JS, Zibold F, Kooijman H, Settles M, Haase A, Rummeny EJ, Wortler K, Karampinos DC. Imaging of the lumbar plexus: optimized refocusing flip angle train design for 3D TSE. J Magn Reson Imaging 2016;43:789–799.
43. Wang G, El-Sharkawy AM, Edelstein WA, Schär M, Bottomley PA. Measuring T2 and T1, and imaging T2 without spin echoes. J Magn Reson 2012;214:273–280.
44. Eggers H, Brendel B, Duijndam A, Herigault G. Dual-echo Dixon imaging with flexible choice of echo times. Magn Reson Med 2011; 65:96–107.
45. Garyfallidis E, Brett M, Amirbekian B, Rokem A, van der Walt S, Descoteaux M, Nimmo-Smith I, Dipy C. Dipy, a library for the analysis of diffusion MRI data. Front Neuroinform 2014;8:8.
46. Mattes D, Haynor DR, Vesselle H, Lewellen TK, Eubank W. PET-CT image registration in the chest using free-form deformations. IEEE Trans Med Imaging 2003;22:120–128.
47. Gluer CC, Blake G, Lu Y, Blunt BA, Jergas M, Genant HK. Accurate assessment of precision errors: how to measure the reproducibility of bone densitometry techniques. Osteoporos Int 1995;5:262–270.
48. Manoliu A, Ho M, Nanz D, Piccirelli M, Dappa E, Klarhofer M, Del Grande F, Kuhn FP. Diffusion tensor imaging of lumbar nerve roots: comparison between fast readout-segmented and selective-excitation acquisitions. Invest Radiol 2016;51:499–504.

49. Le Bihan D, Poupon C, Amadon A, Lethimonnier F. Artifacts and pitfalls in diffusion MRI. J Magn Reson Imaging 2006;24:478–488.
50. Beaulieu CF, Zhou X, Cofer GP, Johnson GA. Diffusion-weighted MR microscopy with fast spin-echo. Magn Reson Med 1993;30:201–206.
51. Brockstedt S, Thomsen C, Wirestam R, Holtas S, Stahlberg F. Quantitative diffusion coefficient maps using fast spin-echo MRI. Magn Reson Imaging 1998;16:877–886.
52. Schick F. SPLICE: sub-second diffusion-sensitive MR imaging using a modified fast spin-echo acquisition mode. Magn Reson Med 1997;38: 638–644.
53. Le Roux P. Non-CPMG fast spin echo with full signal. J Magn Reson 2002;155:278–292.
54. Norris DG, Bornert P, Reese T, Leibfritz D. On the application of ultra-fast RARE experiments. Magn Reson Med 1992;27:142–164.
55. Pipe JG, Farthing VG, Forbes KP. Multishot diffusion-weighted FSE using PROPELLER MRI. Magn Reson Med 2002;47:42–52.
56. Poon CS, Henkelman RM. Practical T2 quantitation for clinical applications. J Magn Reson Imaging 1992;2:541–553.
57. Eppenberger P, Andreisek G, Chhabra A. Magnetic resonance neurography: diffusion tensor imaging and future directions. Neuroimaging Clin N Am 2014;24:245–256.
58. Chhabra A, Madhuranthakam AJ, Andreisek G. Magnetic resonance neurography: current perspectives and literature review. Eur Radiol 2018;28:698–707. doi: 10.1007/s00330-017-4976-8.
59. Gibbons EK, Le Roux P, Vasanawala SS, Pauly JM, Kerr AB. Body diffusion weighted imaging using non-CPMG fast spin echo. IEEE Trans Med Imaging 2017;36:549–559.
60. Gibbons EK, Vasanawala SS, Pauly JM, Kerr AB. Body diffusion-weighted imaging using magnetization prepared single-shot fast spin echo and extended parallel imaging signal averaging. Magn Reson Med 2017. doi: 10.1002/mrm.26971.

SUPPORTING INFORMATION

Additional Supporting Information may be found in the online version of this article.

Fig. S1. Illustrated procedure for localizing the sciatic nerves for DTI analysis. Sagittal, coronal and axial reformats of iso-diffusion-weighted images (isoDWIs) from coronal data acquired with DP 3D TSE and from axial data acquired with DW ss-EPI were created. The femoral head was localized in the sagittal view and the leftright (LR), anterior-posterior (AP) and feet-head (FH) positions of its base were marked. The marked position of the femoral-head base was found and referenced in the coronal view. The sciatic nerve at the marked FH position of the femoral-head base was localized in the coronal view and its LR and AP positions were marked. The marked FH, LR and AP positions of the sciatic nerve were used to localize the nerve in the axial view. The localization procedure was carried out individually for left and right sciatic nerves for each subject.

Fig. S2. Effect of motion-induced phase errors in diffusion quantification with DP 3D TSE. Iso-diffusion-weighted images (iso-DWIs) of two healthy subjects obtained with DP 3D TSE show losses of signal in the sciatic nerve and surrounding muscle when the correction of motion-induced phase errors is not performed. Corresponding mean diffusivity (MD) maps show the overestimation of diffusivity values in nerve and muscle caused by motion-induced phase errors. Unusually high MD values in some regions result from the incompletely suppressed signal of vessels and CSF fluid.

Discussion

The present doctoral thesis is composed of the technical developments demonstrated in the journal publications *Journal Publication I*, *Journal Publication II* and *Journal Publication III*, found in Sections 5.1, 5.2 and 5.3, respectively. The work in *Journal Publication I* and in *Journal Publication II* focused on solving two major problems in morphological MRN specific to T_2-weighted 3D TSE imaging, while the work in *Journal Publication III* tackled the difficult problem of performing diffusion tensor imaging on nerves in the body using a 3D TSE readout.

Specifically, the work in *Journal Publication I* carefully investigated the principles governing the k-space signal generated by a TSE sequence using refocusing angle modulation of two interfacing tissues. The work further used this knowledge to numerically reproduce the response of the imaging signal from nerve tissue with a given geometry embedded in another tissue and to ultimately propose a refocusing angle scheme that yields optimal signal characteristics for such nerve structures. The work in *Journal Publication II* studied in detail a particular technique for vessel-signal suppression and the dephasing mechanisms associated with it. A new method was then proposed which elegantly combines distinct dephasing designs in order to eliminate the signal of lingering blood vessels that obscure nerve visualization. Lastly, the work in *Journal Publication III* investigated the generation of motion-induced phase errors in a proposed diffusion-prepared 3D TSE sequence and their effects on the generated signals. Phase navigation was introduced in the diffusion-prepared 3D TSE sequence and the understanding of motion-induced phase errors was used to incorporate phase correction into the corresponding image reconstruction. The work resulted in a novel technique for performing high- isotropic-resolution 3D imaging of nerves in body regions largely affected by motion.

In the following sections, the work comprising the present doctoral thesis is put into context with existing MRN-specific literature and discussed in its current state as well as in future perspectives.

6.1 Review of Existing Literature

3D TSE imaging is regularly used in MRN for achieving isotropic- and high-resolution T_2-weighted morphological imaging of nerves outside the brain with complex geometries [44, 45]. As for all RARE sequences, the image quality in 3D TSE is governed by the loss of signal intensity and by blurring caused by relaxation effects on k-space data. It has been shown that TSE sequences rely on the design of a refocusing flip angle train that balances relaxation-induced signal loss and blurring for a specific tissue [23, 24, 70, 71]. For this reason, refocusing angle modulation is often used to customize the signal response in TSE sequences with long refocusing trains in a broad range of applications [72–75]. Specifically in the field of MRN, the effect of tissue-specific refocusing angle modulation on 3D TSE

signal and blurring of nerves has been studied and is commonly employed [44, 45, 76, 77]. Tissue-specific refocusing angle modulation in 3D TSE is traditionally based on relaxation considerations of a single reference tissue without taking into account the local geometry or the signal contributions from surrounding tissues. It has been shown that the effect of blurring in imaging of small embedded objects, additionally to the expected loss of edge sharpness, is a loss of signal intensity that can jeopardize the ability to detect such small structures [59]. Previous work has investigated the dependence of the observed TSE signal response of small embedded objects to the employed modulated refocusing angle train and to its spatial (geometric) setting in 2D TSE imaging of the human brain [60]. Until the present day, no experimental assessment of tissue-specific refocusing angle modulation including geometry considerations in nerve imaging is known.

Moreover in morphological T_2-weighted nerve imaging, it is frequently encountered that the presence of signal from nearby vessels compromises the visualization of nerves [78]. In the particular field of vessel signal suppression in MRN, a major challenge that exists in developing a methodology that suppresses unwanted vessel signal is to address slow-flowing vessel signal without disrupting the signal of nerves [10]. In 3D TSE nerve imaging, motion-sensitized driven-equilibrium (MSDE) preparation is often used to suppress vessel signal [76, 77, 79]. In MSDE, the values of the gradient first moment (m_1) typically used for vessel suppression often lead to the incomplete suppression of vessels with slow flow but increasing m_1 can result in motion-induced artifacts and image degradation [36]. The use of velocity compensation in MSDE, effectively resulting in a diffusion-sensitized preparation, for overcoming motion-induced signal loss has been used in diffusion applications using modearte b-values [80, 81]. Velocity compensation has also been incorporated into various preparation techniques in nerve imaging for purposes of vessel signal suppression with minimal motion-induced artifacts [76, 77, 79, 82].

Diffusion tensor imaging is prominently used in MRN for lesion and disease assessment [16–19] due to its ability to probe functional information from the microstructure of nerve fibers [14, 15]. DTI applied in MRN has been shown to lead to a more accurate diagnosis of nerve lesion compared with conventional T_2-weighted morphological imaging [83, 84]. Diffusion imaging of nerves in the body, however, has been shown to present a challenging problem for a broad range of acquisition methods [85, 86]. While conventionally used for diffusion imaging in the brain, single-shot EPI meeting coverage and resolution specifications in MRN has been shown to be highly vulnerable to distortion artifacts arising from eddy currents as well as from off-resonance and chemical shift effects [17, 87]. Alternative methods such as multishot EPI, readout-segmented EPI and single-shot TSE have been shown to reduce geometric distortion and chemical shift artifacts characteristic of single-shot EPI diffusion imaging [68, 88–90] and have been applied in diffusion imaging of nerves in the body [91–95]. Single-shot TSE was shown to overcome the problems encountered with single-shot EPI [96–98] but remained limited to 2D and non-isotropic resolution due to SAR constraints [98–102]. TSE techniques have been used in high-resolution diffusion imaging in a wide range of body applications to avoid distortion and chemical shift artifacts [68, 103–106]. Diffusion-prepared multishot TSE can be combined with a 3D readout to achieve isotropic resolution, shown to be necessary in many MRN applications [45, 76, 107, 108]. Diffusion-prepared multishot TSE, however, has been shown to be highly vulnerable to intershot phase inconsistencies induced by eddy currents and motion [109–111] that have been shown to corrupt both the magnitude as well as the phase of the diffusion-prepared TSE signal [67]. Various methods have been developed for adapting single-shot TSE to diffusion imaging [68, 98, 100, 105, 112]. A particular

method employing dephasing and rephasing gradients in diffusion-prepared single-shot TSE has been shown to minimize the effects induced by eddy currents and motion on the signal magnitude without the need to address effects on the signal phase [68]. Recent work proposed a diffusion-prepared multishot TSE sequence employing dephasing and rephasing gradients as well as velocity compensation for reducing motion-induced phase errors [103, 113, 114]. Residual motion-induced phase variations not accounted for by dephasing and rephasing gradients in the proposed diffusion-prepared multishot TSE method were demonstrated in later work to cause imaging artifacts as well as diffusion quantification errors [110]. The same work also showed that motion-induced artifacts and quantification errors can be eliminated by measuring and correcting the motion-induced intershot phase variations.

6.2 Present Work

6.2.1 Novelty

Previous work in refocusing angle optimization for sequences with long refocusing trains has gone as far as to note the dependence of the signal response of an embedded tissue to refocusing angle modulation and local geometry. The work in *Journal Publication I* (see Section 5.1) introduces a complete methodology for embedded nerves describing the individual contributions of 3D TSE refocusing angle modulation effects on the embedded and surrounding tissues while taking into account the specific geometry of the tissues. Further, this work presents a quantitative evaluation of signal loss and blurring effects in 3D TSE imaging of small embedded objects and verifies it with in vivo results investigating this behaviour. In the context of optimization strategies in 3D TSE imaging, this work demonstrates a geometry-specific refocusing angle modulation scheme for small embedded nerves with in vivo experimental verification.

Vessel signal suppression in MRN has been addressed using either motion or diffusion sensitization. The work in *Journal Publication II* (see Section 5.2) presents a preparation module that combines motion and diffusion sensitization applied in strategically selected gradient axes that maximize vessel signal suppression of both fast and slow blood flow and simultaneously minimize nerve signal attenuation. The proposed methodology takes into account the substructural anisotropy of nerves leading to a predictable signal behaviour in the presence of diffusion sensitization. The presented method additionally considers the relative orientation of nerves with respect to vessels in selected anatomies to carefully choose the orientations of motion- and diffusion-sensitizing gradients. Further, m_1 and b-values in the developed motion- and diffusion-sensitized preparation, as well as the employed RF-pulse specifications, were specifically devised for nerve imaging in the body. Lastly, an eddy current desensitization gradient prepulse was specifically designed for the diffusion-sensitization component of the implemented method, which is shown to considerably diminish image artifacts induced by eddy currents.

The field of diffusion tensor imaging using TSE acquisitions is, until the present day, mostly composed of 2D acquisition methods. Although major advancements have been made for adapting TSE sequences to high in-plane resolution diffusion tensor imaging, few efforts have been made in the development of robust 3D TSE sequences that can be used in high isotropic resolution diffusion tensor imaging. The work in *Journal Publication III* (see Section 5.3) presents a phase-navigated diffusion-prepared 3D TSE acquisition that ad-

dresses effects induced by motion and eddy currents on the signal magnitude (common to single- and multishot diffusion-prepared TSE sequences) as well as intershot phase variations induced by motion (required for multishot only). Effects on the signal magnitude are treated using an existing method developed for diffusion-prepared single-shot TSE but adapted to the developed diffusion preparation, which was specifically designed to be robust to field inhomogeneities encountered in body applications and readily compatible with any type of imaging sequence. Intershot phase variations induced by motion are measured with navigator echoes before the readout of 3D TSE imaging echoes. The navigator acquisition uses the existing pseudo steady state echoes arising from the employed tissue-specific refocusing angle modulation, which are normally not used for imaging to avoid artifacts. Therefore, the inclusion of phase navigation into the 3D TSE sequence does not cause any change in sequence parameters or a longer acquisition duration. A phase correction and reconstruction procedure is also presented, in which phase measured from navigator data is used to phase-correct diffusion data during image reconstruction. The developed work is to our knowledge, the first and currently the only diffusion-prepared phase-corrected 3D TSE method that can be readily applied with Cartesian sampling and without the need of iterative reconstruction.

6.2.2 Impact

Given the regular use of 3D TSE in morphological MRN as well as the need for isotropic, high-resolution 3D imaging in regions where nerves have complex geometries and reduced sizes, it is valuable to improve the performance of the imaging sequence concerning image quality. The methodology provided in *Journal Publication I* provides an optimization tool with which the refocusing angles of the train of pulses in a 3D TSE sequence are customized to generate small-nerve signal with highest intensity for the minimum achievable blurring. Such an optimization tool can be easily incorporated into the scanning interface in order to generate the optimized refocusing angle scheme corresponding to the sequence parameters selected by the user during the preparation of the scanning protocol. The developed refocusing angle optimization tool prevents the loss of small nerve structures due to blurring of the surrounding tissue as well as improved nerve delineation at the tissue interface and of inner fascicles. The presented work therefore provides a formalism that generates superior visualization of small nerves in isotropic high-resolution 3D TSE imaging. Moreover, the presented methodological framework would also be relevant in other applications using 3D TSE for imaging small objects.

Previous work mentioned in Section 6.2.1 has shown that addressing the signal of vessels with slow blood flow in NMR represents a large methodological challenge. Traditional methods designed for vessel suppression using motion sensitization suffer degradation of image quality when the strength of the motion-sensitizing gradients is increased to the sufficiently high values needed to attenuate the signal from slow-flowing blood. Image degradation in motion-sensitized vessel suppression in MRN has been alleviated by replacing motion-sensitizing gradients with a diffusion-sensitized configuration. The work presented in *Journal Publication II* shows that pure diffusion sensitization, while preventing the undesired signal loss encountered in large-m_1 motion sensitization, is not sufficient in suppressing the vessel signal necessary for clear nerve visualization. A vessel-suppression preparation method is proposed in this work, which uses a specific gradient configuration designed for nerve imaging in the body where various vessel-attenuation mechanisms are carefully combined to suppress the signal of vessels with slow and fast flow without dis-

rupting the signal of the imaged nerves. Given the compatibility of the developed preparation method with high-resolution readouts, such as 3D TSE, the presented work provides a powerful tool for vessel suppression in isotropic, high-resolution 3D TSE imaging of nerves in the body.

As described in Section 6.2.1, many efforts have been made in MRN and body applications to develop methods that can be used in high-, isotropic-resolution diffusion tensor imaging. Conventional EPI-based acquisition methods face severe distortion and chemical shift artifacts when approaching isotropic resolutions and are difficult to employ in the body where main-field inhomogeneity is commonly present. TSE-based methods don't suffer from distortion and chemical shift problems but require careful sequence design when preceded by a diffusion preparation. 3D isotropic imaging, shown to be advantageous in diffusion tensor imaging of nerves in the body, requires a multishot acquisition, which then additionaly requires careful handling of the diffusion-prepared data prior to shot combination in the image reconstruction due to motion-induced intershot phase inconsistencies. The work in *Journal Publication III* presents distortion-free isotropic resolution diffusion tensor imaging of nerves in the body in the presence of field inhomogeneity and motion. In the presented analysis where measured diffusion tensor metrics are compared for the proposed 3D TSE method with and without phase correction, it was shown that uncorrected 3D TSE metrics are corrupted by quantification errors and that these are significantly removed by phase correction. A further comparison of the phase-corrected 3D TSE data with single-shot EPI data showed that diffusion tensor metrics obtained with the two methods are significantly similar, supporting similar robustness to motion between the two methods. Given the absence of other TSE-based sequences adapted for motion-robust high isotropic resolution 3D diffusion tensor imaging, the presented method uniquely advances the field of TSE-based diffusion tensor imaging in MRN and body applications. Although the presented novel phase-corrected diffusion-prepared 3D TSE sequence was demonstrated for MRN, the method is anatomy-independent and can be adapted to any application requiring isotropic resolution 3D TSE diffusion imaging.

6.2.3 Limitations

The present work has some limitations. The refocusing angle optimization strategy presented in *Journal Publication I* is limited to a selected parameter space and therefore specific to a subselection of 3D TSE sequences. The presented theoretical framework should however also hold for other selections of sequence parameters. Moreover, unknown spatial variations in relaxation times in a given tissue might result in a deviation of the observed signal response from that which is expected, given that only a single pair of T_1 and T_2 relaxation times can be used for a given tissue-specific refocusing angle optimization. Similarly, spatial variations in the geometry of a given tissue can lead to variations in the observed signal response. Further, the balancing of signal loss and blurring aimed at by the refocusing angle optimization unavoidably leads to a certain degree of signal loss, which is undesired in low-SNR scans.

The vessel-suppression preparation method presented in *Journal Publication II* also has a number of limitations. The overall unavoidable signal loss induced by diffusion-sensitized gradients may be undesirable in low-SNR scans. In such situations, lower b-values can still be used at the expense of inferior vessel signal suppression. Moreover, although the sequence design of the proposed vessel-suppression preparation effectively reduces vessel signal, the attenuation mechanisms employed by this method do not sup-

press the signal of stationary fluid, which might obstruct nerve visualization. Further, although the proposed eddy current desensitization technique was shown to yield images free of eddy-current artifacts, eddy currents may appear when implementing the presented method on different imaging systems with different eddy current properties, particularly if high b-values are used. It is also important to note that the insensitivity to motion introduced by velocity compensation in the proposed method is limited. At sufficiently high b-values, motion-induced phase from higher-order motion may become significant and lead to artifacts. The use of moderate b-values, as done in the present work, should reduce such effects. Further, since the proposed vessel-suppression preparation utilizes diffusion sensitization, depending on the b-value used, the prepared signal will have a diffusion weighting in addition to the desired T_2 weighting. Lastly, the presented method has until now only been demonstrated in the lower extremities and might require minor modifications for its application in other anatomies.

The phase-corrected diffusion-prepared 3D TSE technique presented in *Journal Publication III* has several limitations. As any 3D acquisition, the proposed method is associated with considerably longer scan times than 2D single-shot EPI due to the efficient k-space traversal of the EPI trajectory and the interleaving capability of 2D acquisitions. Moreover, the proposed diffusion-prepared 3D TSE sequence has lower SNR efficiency than diffusion-weighted single-shot EPI. However, diffusion-weighted single-shot EPI is only expected to be suitable for diffusion MRN applications where isotropic resolutions are not needed and where off-resonance does not cause unacceptable geometric distortions and chemical shift artifacts. In the cases of isotropic resolution requirements and in imaging of anatomies where field inhomogeneity and the presence of fat signal are problematic and inevitable, the proposed technique can become of superior value in spite of the compromise in SNR efficiency. Further, for the incorporation of phase navigation during the pseudo steady state stage preceding each echo-train in the 3D TSE readout, navigator echoes in the developed method are acquired without phase encoding in the k_z direction. This results in the acquisition of a 2D navigator image that is the average of the 3D imaging volume along the z direction. The developed method therefore cannot resolve linear and higher order phase errors along the k_z direction. Translational motion along this direction resulting in spatially constant phase errors, however, can still be detected and corrected by the proposed method. The performance of the presented phase correction technique is therefore limited by the spatial coverage and the severeness of motion along the non-phase-encoded direction.

6.3 Perspectives

The work enclosed in the present doctoral thesis concerning morphological 3D TSE imaging can be readily incorporated into routine clinical examinations and research studies where nerves need to be visualized in multiple views. The refocusing angle strategy proposed in *Journal Publication I* for 3D TSE can be included in a clinical protocol for a detailed visualization of small nerves and their branches, as well as whenever the nerve fascicles need to be resolved. Even in cases where nerves need to be visualized with high in-plane resolution, the proposed technique can be used to locate regions of interest as well as to inspect the entire anatomy of interest in a single glance using large fields of view. Since its development, the proposed method has been employed in multiple research protocols for the visualization of fine nerve features with satisfactory results, proving its usefulness and

value.

The vessel-suppression preparation presented in *Journal Publication II* can be used in all types of nerve imaging protocols where small vessels with slow flow obscure nerve visualization. This technique is, however, specific to certain relative vessel-to-nerve geometries and requires careful planning for best results. The developed vessel-suppression preparation can be coupled with any imaging sequence, making it highly versatile in its application. Coupled with a high isotropic resolution 3D TSE readout, as shown in the present work, the proposed preparation can be used to visualize nerves along their long axes as well as in transverse views for careful inspection for lesions or anomalies.

The phase-corrected diffusion-prepared 3D TSE in *Journal Publication III* is suitable for clinical or research studies requiring functional nerve information. Given the sensitivity of quantitative diffusion imaging to microstructural changes, the developed method could provide valuable information in longitudinal studies as well as in evaluations that take place before and after an invasive intervention. Further, the proposed method can be used in conjunction with diffusion tensor imaging for the generation of fiber tracks. Most valuable, the method can be used to perform the above-mentioned assessments in a high isotropic resolution regime using large fields of view.

Acknowledgements

I would like to thank the people whose efforts guided and supported the work that has formed this PhD degree. My greatest gratitude goes to Dimitrios Karampinos, who has been much more than our group leader. Thank you Dimitris for all of what you have taught me and for the extremely valuable tools that you have given me. Thank you for pushing me forward, for giving me vision and for always keeping me inspired. Thank you for making this experience so rewarding and for giving me the opportunity to work with such an exceptional team. It has been a privilege to be part of your group and to work with you in the last four years. I would also like to thank Ernst Rummeny and Axel Haase for their vast support and invaluable insight. I am very grateful to have had counted with your expertise during this project. I greatly thank Jan Kirschke for all of his help and substantial contributions to my work during my entire PhD project. Thank you Jan for involving me in your research and for always lending me a hand in mine, I have learned a lot from you and it has been a pleasure working with you. On a similar note I would like to thank Thomas Baum for his collaboration and support. Thank you Thomas all the insight you have provided me, it has been crucial in raising the quality of my work. It has also been a pleasure working with you. I would like to thank Alex Gersing and Klaus Wörtler for their insight and collaboration. Thank you both very much for helping my research grow. I deeply thank Anh Van for all of her help and for our collaboration. Thank you Anh, I feel very fortunate to have had the chance to work with you. Not only was it really fun, but your contribution really shaped the end result of my research. I also deeply thank Harry Hu for his immense support and contribution to my work. Harry I feel very fortunate to have worked with you, thank you for all the time and effort you have dedicated to my work. Many thanks to Lilly Klupp and Nico Sollmann for their collaboration. It has been really fun working with you! I would like to greatly thank Dick Kooijman and Andi Hock for all of their backing for my work. Thank you both for all the great ideas and input your provided me that always pushed me in the right directions. I would also like to thank Marcus Settles and Carl Ganter for their support and valuable discussions. I feel very fortunate to have had input from you during my PhD project. Very importantly I would like to thank my colleagues and friends in the group. Thank you guys for making this so much fun! You are all outstanding people and it was been a privilege working with you. Thank you Stefan, Michael, Christian, Dominik, Max, Sarah, Jan, Sophia and Christoph for the last four years full of exciting work and fun times, I will never forget them!

List of Figures

List of Tables

Bibliography

[1] Thawait, S K, Chaudhry, V, Thawait, G K, Wang, K C, Belzberg, A, Carrino, J A, and Chhabra, A, "High-Resolution MR Neurography of Diffuse Peripheral Nerve Lesions", *American Journal of Neuroradiology*, vol. 32, no. 8, pp. 1365–1372, Sep. 2011.

[2] G. Andreisek, D. W. Crook, D. Burg, B. Marincek, and D. Weishaupt, "Peripheral neuropathies of the median, radial, and ulnar nerves: Mr imaging features", *Radiographics*, vol. 26, no. 5, pp. 1267–1287, 2006.

[3] M. Bendszus, M. Koltzenburg, C. Wessig, and L. Solymosi, "Sequential mr imaging of denervated muscle: Experimental study", *American journal of neuroradiology*, vol. 23, no. 8, pp. 1427–1431, 2002.

[4] M. Bendszus, C. Wessig, K. Reiners, A. J. Bartsch, L. Solymosi, and M. Koltzenberg, "Mr imaging in the differential diagnosis of neurogenic foot drop", *American journal of neuroradiology*, vol. 24, no. 7, pp. 1283–1289, 2003.

[5] A. Chhabra, E. Williams, K. Wang, A. Dellon, and J. Carrino, "Mr neurography of neuromas related to nerve injury and entrapment with surgical correlation", *American Journal of Neuroradiology*, vol. 31, no. 8, pp. 1363–1368, 2010.

[6] A. G. Filler, M. Kliot, F. A. Howe, C. E. Hayes, D. E. Saunders, R. Goodkin, B. A. Bell, H. R. Winn, J. R. Griffiths, and J. S. Tsuruda, "Application of magnetic resonance neurography in the evaluation of patients with peripheral nerve pathology", *Journal of neurosurgery*, vol. 85, no. 2, pp. 299–309, 1996.

[7] A. G. Filler, J. Haynes, S. E. Jordan, J. Prager, J. P. Villablanca, K. Farahani, D. Q. Mcbride, J. S. Tsuruda, B. Morisoli, U. Batzdorf, *et al.*, "Sciatica of nondisc origin and piriformis syndrome: Diagnosis by magnetic resonance neurography and interventional magnetic resonance imaging with outcome study of resulting treatment", *Journal of Neurosurgery: Spine*, vol. 2, no. 2, pp. 99–115, 2005.

[8] F. Howe, A. Filler, B. Bell, and J. Griffiths, "Magnetic resonance neurography", *Magnetic resonance in medicine*, vol. 28, no. 2, pp. 328–338, 1992.

[9] A. Chhabra, P. P. Lee, C. Bizzell, and T. Soldatos, "3 tesla mr neurography—technique, interpretation, and pitfalls", *Skeletal radiology*, vol. 40, no. 10, p. 1249, 2011.

[10] A. Chhabra, G. Andreisek, T. Soldatos, K. C. Wang, A. J. Flammang, A. J. Belzberg, and J. A. Carrino, "Mr neurography: Past, present, and future", *American Journal of Roentgenology*, vol. 197, no. 3, pp. 583–591, 2011.

[11] M. Bendszus and G. Stoll, "Technology insight: Visualizing peripheral nerve injury using mri", *Nature clinical practice Neurology*, vol. 1, no. 1, pp. 45–53, 2005.

[12] J. Karppinen, A. Malmivaara, O. Tervonen, E. Pääkkö, M. Kurunlahti, P. Syrjälä, P. Vasari, and H. Vanharanta, "Severity of symptoms and signs in relation to magnetic resonance imaging findings among sciatic patients", *Spine*, vol. 26, no. 7, E149–E154, 2001.

[13] Y. Aota, T. Niwa, K. Yoshikawa, A. Fujiwara, T. Asada, and T. Saito, “Magnetic resonance imaging and magnetic resonance myelography in the presurgical diagnosis of lumbar foraminal stenosis”, *Spine*, vol. 32, no. 8, pp. 896–903, 2007.

[14] A. L. Alexander, K. Hasan, G. Kindlmann, D. L. Parker, and J. S. Tsuruda, “A geometric analysis of diffusion tensor measurements of the human brain”, *Magnetic Resonance in Medicine*, vol. 44, no. 2, pp. 283–291, 2000.

[15] S. Mori and J. Zhang, “Principles of diffusion tensor imaging and its applications to basic neuroscience research”, *Neuron*, vol. 51, no. 5, pp. 527–539, 2006.

[16] T. Kakuda, H. Fukuda, K. Tanitame, M. Takasu, S. Date, K. Ochi, T. Ohshita, T. Kohriyama, K. Ito, M. Matsumoto, *et al.*, “Diffusion tensor imaging of peripheral nerve in patients with chronic inflammatory demyelinating polyradiculoneuropathy: A feasibility study”, *Neuroradiology*, vol. 53, no. 12, pp. 955–960, 2011.

[17] D. C. Karampinos, G. Melkus, T. M. Shepherd, S. Banerjee, E. U. Saritas, A. Shankaranarayanan, C. P. Hess, T. M. Link, W. P. Dillon, and S. Majumdar, “Diffusion tensor imaging and t2 relaxometry of bilateral lumbar nerve roots: Feasibility of in-plane imaging”, *NMR in biomedicine*, vol. 26, no. 6, pp. 630–637, 2013.

[18] C. Mathys, J. Aissa, Z. Hörste, G. Meyer, D. C. Reichelt, G. Antoch, B. Turowski, H.-P. Hartung, K. A. Sheikh, and H. C. Lehmann, “Peripheral neuropathy: Assessment of proximal nerve integrity by diffusion tensor imaging”, *Muscle & nerve*, vol. 48, no. 6, pp. 889–896, 2013.

[19] N. G. Simon, J. Lagopoulos, T. Gallagher, M. Kliot, and M. C. Kiernan, “Peripheral nerve diffusion tensor imaging is reliable and reproducible”, *Journal of Magnetic Resonance Imaging*, vol. 43, no. 4, pp. 962–969, 2016.

[20] J. Hennig, A. Nauerth, and H. Friedburg, “Rare imaging: A fast imaging method for clinical mr”, *Magnetic resonance in medicine*, vol. 3, no. 6, pp. 823–833, 1986.

[21] J. Hennig, “Multiecho imaging sequences with low refocusing flip angles”, *Journal of Magnetic Resonance (1969)*, vol. 78, no. 3, pp. 397–407, 1988.

[22] S. Meiboom and D. Gill, “Modified spin-echo method for measuring nuclear relaxation times”, *Review of scientific instruments*, vol. 29, no. 8, pp. 688–691, 1958.

[23] R. F. Busse, H. Hariharan, A. Vu, and J. H. Brittain, “Fast spin echo sequences with very long echo trains: Design of variable refocusing flip angle schedules and generation of clinical t2 contrast”, *Magnetic resonance in medicine*, vol. 55, no. 5, pp. 1030–1037, 2006.

[24] J. P. Mugler, “Optimized three-dimensional fast-spin-echo mri”, *Journal of Magnetic Resonance Imaging*, vol. 39, no. 4, pp. 745–767, 2014.

[25] R. F. Busse, A. Brau, A. Vu, C. R. Michelich, E. Bayram, R. Kijowski, S. B. Reeder, and H. A. Rowley, “Effects of refocusing flip angle modulation and view ordering in 3d fast spin echo”, *Magnetic resonance in medicine*, vol. 60, no. 3, pp. 640–649, 2008.

[26] R. R. Edelman, D. Chien, and D. Kim, “Fast selective black blood mr imaging.”, *Radiology*, vol. 181, no. 3, pp. 655–660, 1991.

[27] O. P. Simonetti, J. P. Finn, R. D. White, G. Laub, and D. A. Henry, “" black blood" t2-weighted inversion-recovery mr imaging of the heart.”, *Radiology*, vol. 199, no. 1, pp. 49–57, 1996.

[28] D. A. Steinman and B. K. Rutt, "On the nature and reduction of plaque-mimicking flow artifacts in black blood mri of the carotid bifurcation", *Magnetic resonance in medicine*, vol. 39, no. 4, pp. 635–641, 1998.

[29] J. P. Felmlee and R. L. Ehman, "Spatial presaturation: A method for suppressing flow artifacts and improving depiction of vascular anatomy in mr imaging.", *Radiology*, vol. 164, no. 2, pp. 559–564, 1987.

[30] I. Koktzoglou and D. Li, "Diffusion-prepared segmented steady-state free precession: Application to 3d black-blood cardiovascular magnetic resonance of the thoracic aorta and carotid artery walls", *Journal of Cardiovascular Magnetic Resonance*, vol. 9, no. 1, pp. 33–42, 2007.

[31] J. Wang, V. L. Yarnykh, T. Hatsukami, B. Chu, N. Balu, and C. Yuan, "Improved suppression of plaque-mimicking artifacts in black-blood carotid atherosclerosis imaging using a multislice motion-sensitized driven-equilibrium (msde) turbo spin-echo (tse) sequence", *Magnetic resonance in medicine*, vol. 58, no. 5, pp. 973–981, 2007.

[32] H. Lee and R. R. Price, "Diffusion imaging with the mp-rage sequence", *Journal of Magnetic Resonance Imaging*, vol. 4, no. 6, pp. 837–842, 1994.

[33] D. L. Thomas, G. S. Pell, M. F. Lythgoe, D. G. Gadian, and R. J. Ordidge, "A quantitative method for fast diffusion imaging using magnetization-prepared turboflash", *Magnetic resonance in medicine*, vol. 39, no. 6, pp. 950–960, 1998.

[34] E.-K. Jeong, S.-E. Kim, and D. L. Parker, "High-resolution diffusion-weighted 3d mri, using diffusion-weighted driven-equilibrium (dw-de) and multishot segmented 3d-ssfp without navigator echoes", *Magnetic resonance in medicine*, vol. 50, no. 4, pp. 821–829, 2003.

[35] T. Numano, K. Homma, and T. Hirose, "Diffusion-weighted three-dimensional mp-rage mr imaging", *Magnetic resonance imaging*, vol. 23, no. 3, pp. 463–468, 2005.

[36] J. Wang, V. L. Yarnykh, and C. Yuan, "Enhanced image quality in black-blood mri using the improved motion-sensitized driven-equilibrium (imsde) sequence", *Journal of Magnetic Resonance Imaging*, vol. 31, no. 5, pp. 1256–1263, 2010.

[37] M. H. Levitt, R. Freeman, and T. Frenkiel, "Broadband heteronuclear decoupling", *Journal of Magnetic Resonance (1969)*, vol. 47, no. 2, pp. 328–330, 1982.

[38] A. Einstein, *Investigations on the Theory of the Brownian Movement*. Courier Corporation, 1956.

[39] E. O. Stejskal and J. E. Tanner, "Spin diffusion measurements: Spin echoes in the presence of a time-dependent field gradient", *The journal of chemical physics*, vol. 42, no. 1, pp. 288–292, 1965.

[40] J. E. Tanner, "Use of the stimulated echo in nmr diffusion studies", *The Journal of Chemical Physics*, vol. 52, no. 5, pp. 2523–2526, 1970.

[41] D. Le Bihan and E. Breton, "In vivo magnetic resonance imaging of diffusion", *Comptes Rendus des Seances de l'Academie des Sciences. Serie 2*, vol. 301, no. 15, pp. 1109–1112, 1985.

[42] D. Le Bihan, E. Breton, D. Lallemand, P. Grenier, E. Cabanis, and M. Laval-Jeantet, "Mr imaging of intravoxel incoherent motions: Application to diffusion and perfusion in neurologic disorders.", *Radiology*, vol. 161, no. 2, pp. 401–407, 1986.

[43] A. W. Anderson and J. C. Gore, “Analysis and correction of motion artifacts in diffusion weighted imaging”, *Magnetic resonance in medicine*, vol. 32, no. 3, pp. 379–387, 1994.

[44] T. Soldatos, G. Andreisek, G. K. Thawait, R. Guggenberger, E. H. Williams, J. A. Carrino, and A. Chhabra, “High-resolution 3-t mr neurography of the lumbosacral plexus”, *Radiographics*, vol. 33, no. 4, pp. 967–987, 2013.

[45] A. Chhabra, G. Thawait, T. Soldatos, R. Thakkar, F. Del Grande, M. Chalian, and J. Carrino, “High-resolution 3t mr neurography of the brachial plexus and its branches, with emphasis on 3d imaging”, *American Journal of Neuroradiology*, vol. 34, no. 3, pp. 486–497, 2013.

[46] E. Jaynes, “Matrix treatment of nuclear induction”, *Physical Review*, vol. 98, no. 4, p. 1099, 1955.

[47] D. E. Woessner, “Effects of diffusion in nuclear magnetic resonance spin-echo experiments”, *The Journal of Chemical Physics*, vol. 34, no. 6, pp. 2057–2061, 1961.

[48] R. Kaiser, E. Bartholdi, and R. Ernst, “Diffusion and field-gradient effects in nmr fourier spectroscopy”, *The Journal of Chemical Physics*, vol. 60, no. 8, pp. 2966–2979, 1974.

[49] J. Hennig, “Echoes—how to generate, recognize, use or avoid them in mr-imaging sequences. part i: Fundamental and not so fundamental properties of spin echoes”, *Concepts in Magnetic Resonance Part A*, vol. 3, no. 3, pp. 125–143, 1991.

[50] W. T. Sobol and D. M. Gauntt, “On the stationary states in gradient echo imaging”, *Journal of Magnetic Resonance Imaging*, vol. 6, no. 2, pp. 384–398, 1996.

[51] A. Sodickson and D. G. Cory, “A generalized k-space formalism for treating the spatial aspects of a variety of nmr experiments”, *Progress in nuclear magnetic resonance spectroscopy*, vol. 33, no. 2, pp. 77–108, 1998.

[52] K. Scheffler, “A pictorial description of steady-states in rapid magnetic resonance imaging”, *Concepts in Magnetic Resonance*, vol. 11, no. 5, pp. 291–304, 1999.

[53] M. T. Vlaardingerbroek and J. A. Boer, *Magnetic resonance imaging: theory and practice*. Springer Science & Business Media, 2013.

[54] Y. Zur, “An algorithm to calculate the nmr signal of a multi spin-echo sequence with relaxation and spin-diffusion”, *Journal of Magnetic Resonance*, vol. 171, no. 1, pp. 97–106, 2004.

[55] M. Weigel, S. Schwenk, V. Kiselev, K. Scheffler, and J. Hennig, “Extended phase graphs with anisotropic diffusion”, *Journal of magnetic resonance*, vol. 205, no. 2, pp. 276–285, 2010.

[56] J. Hennig and K. Scheffler, “Hyperechoes”, *Magnetic resonance in medicine*, vol. 46, no. 1, pp. 6–12, 2001.

[57] J. Hennig, M. Weigel, and K. Scheffler, “Multiecho sequences with variable refocusing flip angles: Optimization of signal behavior using smooth transitions between pseudo steady states (traps)”, *Magnetic resonance in medicine*, vol. 49, no. 3, pp. 527–535, 2003.

[58] J. P. Mugler, F. H. Epstein, and J. R. Brookeman, "Shaping the signal response during the approach to steady state in three-dimensional magnetization-prepared rapid gradient-echo imaging using variable flip angles", *Magnetic resonance in medicine*, vol. 28, no. 2, pp. 165–185, 1992.

[59] R. T. Constable and J. C. Gore, "The loss of small objects in variable te imaging: Implications for fse, rare, and epi", *Magnetic resonance in medicine*, vol. 28, no. 1, pp. 9–24, 1992.

[60] R. Deichmann, C. Good, O. Josephs, J. Ashburner, and R. Turner, "Optimization of 3-d mp-rage sequences for structural brain imaging", *Neuroimage*, vol. 12, no. 1, pp. 112–127, 2000.

[61] C. Zhu, M. J. Graves, J. Yuan, U. Sadat, J. H. Gillard, and A. J. Patterson, "Optimization of improved motion-sensitized driven-equilibrium (imsde) blood suppression for carotid artery wall imaging", *Journal of Cardiovascular Magnetic Resonance*, vol. 16, no. 1, p. 61, 2014.

[62] Z. Fan, J. Sheehan, X. Bi, X. Liu, J. Carr, and D. Li, "3d noncontrast mr angiography of the distal lower extremities using flow-sensitive dephasing (fsd)-prepared balanced ssfp", *Magnetic resonance in medicine*, vol. 62, no. 6, pp. 1523–1532, 2009.

[63] J. J. Sheehan, Z. Fan, A. H. Davarpanah, P. A. Hodnett, J. Varga, J. C. Carr, and D. Li, "Nonenhanced mr angiography of the hand with flow-sensitive dephasing–prepared balanced ssfp sequence: Initial experience with systemic sclerosis", *Radiology*, vol. 259, no. 1, pp. 248–256, 2011.

[64] E. R. Jenista, W. G. Rehwald, E.-L. Chen, H. W. Kim, I. Klem, M. A. Parker, and R. J. Kim, "Motion and flow insensitive adiabatic t2-preparation module for cardiac mr imaging at 3 tesla", *Magnetic resonance in medicine*, vol. 70, no. 5, pp. 1360–1368, 2013.

[65] R. Nezafat, R. Ouwerkerk, A. J. Derbyshire, M. Stuber, and E. R. McVeigh, "Spectrally selective b1-insensitive t2 magnetization preparation sequence", *Magnetic resonance in medicine*, vol. 61, no. 6, pp. 1326–1335, 2009.

[66] D. Weidlich, S. Schlaeger, H. Kooijman, P. Börnert, J. S. Kirschke, E. J. Rummeny, A. Haase, and D. C. Karampinos, "T2 mapping with magnetization-prepared 3d tse based on a modified bir-4 t2 preparation", *NMR in Biomedicine*, vol. 30, no. 11, 2017.

[67] A. T. Van, B. Cervantes, H. Kooijman, and D. C. Karampinos, "Analysis of phase error effects in multishot diffusion-prepared turbo spin echo imaging", *Quantitative imaging in medicine and surgery*, vol. 7, no. 2, p. 238, 2017.

[68] D. C. Alsop, "Phase insensitive preparation of single-shot rare: Application to diffusion imaging in humans", *Magnetic resonance in medicine*, vol. 38, no. 4, pp. 527–533, 1997.

[69] E. Garyfallidis, M. Brett, B. Amirbekian, A. Rokem, S. Van Der Walt, M. Descoteaux, and I. Nimmo-Smith, "Dipy, a library for the analysis of diffusion mri data", *Frontiers in Neuroinformatics*, vol. 8, p. 8, 2014, ISSN: 1662-5196. DOI: 10.3389/fninf.2014.00008. [Online]. Available: https://www.frontiersin.org/article/10.3389/fninf.2014.00008.

[70] J. Mugler, H. Meyer, and B. Kiefer, "Practical implementation of optimized tissue-specific prescribed signal evolutions for improved turbo-spin-echo imaging", in *Proceedings of the 11th Meeting of ISMRM. Berkeley, California*, vol. 203, 2003.

[71] J. P. Mugler, B. Kiefer, and J. R. Brookeman, "Three-dimensional t2-weighted imaging of the brain using very long spin-echo trains", in *Proceedings of the 8th Annual Meeting of ISMRM*, 2000, p. 687.

[72] W. Chen, K. Granlund, D. Huo, and G. G. E, "A systematic approach to design flip angle modulation in pseudo-steady-state 3d fast spin echo acquisition", in *Proceedings of the 21st Annual Meeting of ISMRM*, 2013, p. 3716.

[73] H. Lee, E.-Y. Kim, K.-S. Yang, and J. Park, "Susceptibility-resistant variable-flip-angle turbo spin echo imaging for reliable estimation of cortical thickness: A feasibility study", *Neuroimage*, vol. 59, no. 1, pp. 377–388, 2012.

[74] J. Mugler III, "Iii; wald, ll.; brookeman, jr. t2-weighted 3d spin-echo train imaging of the brain at 3 tesla: Reduced power deposition using low flip-angle refocusing rf pulses", in *Proceedings of the 9th Annual Meeting of ISMRM*, 2001, p. 438.

[75] J. Park, J. P. Mugler, W. Horger, and B. Kiefer, "Optimized t1-weighted contrast for single-slab 3d turbo spin-echo imaging with long echo trains: Application to whole-brain imaging", *Magnetic resonance in medicine*, vol. 58, no. 5, pp. 982–992, 2007.

[76] J. M. Kasper, V. Wadhwa, K. M. Scott, S. Rozen, Y. Xi, and A. Chhabra, "Shinkei—a novel 3d isotropic mr neurography technique: Technical advantages over 3dirtse-based imaging", *European radiology*, vol. 25, no. 6, pp. 1672–1677, 2015.

[77] M. Yoneyama, M. Nakamura, T. Okuaki, T. Tabuchi, A. Takemura, M. Obara, and J. Ogura, "High-resolution 3d volumetric nerve-sheath weighted rare imaging (3d shinkei)", in *Proceedings of the 19th Annual Meeting of ISMRM*, 2011, p. 2721.

[78] A. Chhabra, L. Zhao, J. A. Carrino, E. Trueblood, S. Koceski, F. Shteriev, L. Lenkinski, C. D. Sinclair, and G. Andreisek, "Mr neurography: Advances", *Radiology research and practice*, vol. 2013, 2013.

[79] M. Yoneyama, T. Takahara, T. C. Kwee, M. Nakamura, and T. Tabuchi, "Rapid high resolution mr neurography with a diffusion-weighted pre-pulse", *Magnetic Resonance in Medical Sciences*, vol. 12, no. 2, pp. 111–119, 2013.

[80] H. Liu, Z. Zhou, J. Wang, S. Chen, B. Niranjan, and C. Yuan, "Time-efficient diffusion-weighted black blood imaging based on imsde", in *Proceedings of the 22nd Annual Meeting of ISMRM*, 2014, p. 2532.

[81] T. Schakel, H. Hoogduin, and M. Philippens, "In vivo high resolution, undistorted diffusion weighted imaging using dsde-tfe", in *Proceedings of the 22nd Annual Meeting of ISMRM*, 2014, p. 668.

[82] A. Chhabra, T. Soldatos, T. K. Subhawong, A. J. Machado, S. K. Thawait, K. C. Wang, A. Padua, A. J. Flammang, E. H. Williams, and J. A. Carrino, "The application of three-dimensional diffusion-weighted psif technique in peripheral nerve imaging of the distal extremities", *Journal of Magnetic Resonance Imaging*, vol. 34, no. 4, pp. 962–967, 2011.

[83] A. Chhabra, R. Thakkar, G. Andreisek, M. Chalian, A. Belzberg, J. Blakeley, A. Hoke, G. Thawait, J. Eng, and J. Carrino, "Anatomic mr imaging and functional diffusion tensor imaging of peripheral nerve tumors and tumorlike conditions", *American Journal of Neuroradiology*, vol. 34, no. 4, pp. 802–807, 2013.

[84] A. M. Naraghi, H. Awdeh, V. Wadhwa, G. Andreisek, and A. Chhabra, "Diffusion tensor imaging of peripheral nerves", in *Seminars in musculoskeletal radiology*, Thieme Medical Publishers, vol. 19, 2015, pp. 191–200.

[85] B. Cervantes, D. Weidlich, H. Kooijman, E. J. Rummeny, A. Haase, J. S. Kirschke, and D. C. Karampinos, "High-resolution dwi of the lumbar plexus using b1-insensitive velocity-compensated diffusion-prepared 3d tse", in *Proc. of 24th Scientific Meeting of ISMRM*, Singapore, Singapore, 2016, p. 4474.

[86] A. Manoliu, M. Ho, D. Nanz, M. Piccirelli, E. Dappa, M. Klarhöfer, F. Del Grande, and F. P. Kuhn, "Diffusion tensor imaging of lumbar nerve roots: Comparison between fast readout-segmented and selective-excitation acquisitions", *Investigative radiology*, vol. 51, no. 8, pp. 499–504, 2016.

[87] D. Le Bihan, C. Poupon, A. Amadon, and F. Lethimonnier, "Artifacts and pitfalls in diffusion mri", *Journal of magnetic resonance imaging*, vol. 24, no. 3, pp. 478–488, 2006.

[88] S. J. Holdsworth, S. Skare, R. D. Newbould, and R. Bammer, "Robust grappa-accelerated diffusion-weighted readout-segmented (rs)-epi", *Magnetic resonance in medicine*, vol. 62, no. 6, pp. 1629–1640, 2009.

[89] D. A. Porter and R. M. Heidemann, "High resolution diffusion-weighted imaging using readout-segmented echo-planar imaging, parallel imaging and a two-dimensional navigator-based reacquisition", *Magnetic resonance in medicine*, vol. 62, no. 2, pp. 468–475, 2009.

[90] W. Wu and K. L. Miller, "Image formation in diffusion mri: A review of recent technical developments", *Journal of Magnetic Resonance Imaging*, 2017.

[91] A. Manoliu, M. Ho, M. Piccirelli, D. Nanz, L. Filli, E. Dappa, W. Liu, D. A. Ettlin, A. Boss, G. Andreisek, *et al.*, "Simultaneous multislice readout-segmented echo planar imaging for accelerated diffusion tensor imaging of the mandibular nerve: A feasibility study", *Journal of Magnetic Resonance Imaging*, vol. 46, no. 3, pp. 663–677, 2017.

[92] L. H. Markvardsen, M. Vaeggemose, S. Ringgaard, and H. Andersen, "Diffusion tensor imaging can be used to detect lesions in peripheral nerves in patients with chronic inflammatory demyelinating polyneuropathy treated with subcutaneous immunoglobulin", *Neuroradiology*, vol. 58, no. 8, pp. 745–752, 2016.

[93] M. Vaeggemose, M. Pham, S. Ringgaard, H. Tankisi, N. Ejskjaer, S. Heiland, P. L. Poulsen, and H. Andersen, "Diffusion tensor imaging mr neurography for the detection of polyneuropathy in type 1 diabetes", *Journal of Magnetic Resonance Imaging*, vol. 45, no. 4, pp. 1125–1134, 2017.

[94] R. Yamashita, H. Isoda, S. Arizono, A. Furuta, T. Ohno, A. Ono, K. Murata, and K. Togashi, "Selective visualization of pelvic splanchnic nerve and pelvic plexus using readout-segmented echo-planar diffusion-weighted magnetic resonance neurography: A preliminary study in healthy male volunteers", *European journal of radiology*, vol. 86, pp. 52–57, 2017.

[95] L. Filli, M. Piccirelli, D. Kenkel, A. Boss, A. Manoliu, G. Andreisek, H. Bhat, V. M. Runge, and R. Guggenberger, "Accelerated magnetic resonance diffusion tensor imaging of the median nerve using simultaneous multi-slice echo planar imaging with blipped caipirinha", *European radiology*, vol. 26, no. 6, pp. 1921–1928, 2016.

[96] C. F. Beaulieu, X. Zhou, G. P. Cofer, and G. A. Johnson, "Diffusion-weighted mr microscopy with fast spin-echo", *Magnetic resonance in medicine*, vol. 30, no. 2, pp. 201–206, 1993.

[97] S. Brockstedt, C. Thomsen, R. Wirestam, S. Holtås, and F. Ståhlberg, "Quantitative diffusion coefficient maps using fast spin-echo mri", *Magnetic resonance imaging*, vol. 16, no. 8, pp. 877–886, 1998.

[98] F. Schick, "Splice: Sub-second diffusion-sensitive mr imaging using a modified fast spin-echo acquisition mode", *Magnetic resonance in medicine*, vol. 38, no. 4, pp. 638–644, 1997.

[99] P. Le Roux, "Non-cpmg fast spin echo with full signal", *Journal of Magnetic Resonance*, vol. 155, no. 2, pp. 278–292, 2002.

[100] D. G. Norris, P. Börnert, T. Reese, and D. Leibfritz, "On the application of ultra-fast rare experiments", *Magnetic resonance in medicine*, vol. 27, no. 1, pp. 142–164, 1992.

[101] J. G. Pipe, V. G. Farthing, and K. P. Forbes, "Multishot diffusion-weighted fse using propeller mri", *Magnetic resonance in medicine*, vol. 47, no. 1, pp. 42–52, 2002.

[102] C. S. Poon and R. M. Henkelman, "Practical t2 quantitation for clinical applications", *Journal of Magnetic Resonance Imaging*, vol. 2, no. 5, pp. 541–553, 1992.

[103] Q. Zhang, B. F. Coolen, M. J. Versluis, G. J. Strijkers, and A. J. Nederveen, "Diffusion-prepared stimulated-echo turbo spin echo (dpsti-tse): An eddy current-insensitive sequence for three-dimensional high-resolution and undistorted diffusion-weighted imaging", *NMR in Biomedicine*, vol. 30, no. 7, 2017.

[104] Y. Xie, W. Yu, Z. Fan, C. Nguyen, X. Bi, J. An, T. Zhang, Z. Zhang, and D. Li, "High resolution 3d diffusion cardiovascular magnetic resonance of carotid vessel wall to detect lipid core without contrast media", *Journal of Cardiovascular Magnetic Resonance*, vol. 16, no. 1, p. 67, 2014.

[105] J. G. Pipe *et al.*, "Motion correction with propeller mri: Application to head motion and free-breathing cardiac imaging", *Magnetic resonance in medicine*, vol. 42, no. 5, pp. 963–969, 1999.

[106] X. J. Zhou, N. E. Leeds, G. C. McKinnon, and A. J. Kumar, "Characterization of benign and metastatic vertebral compression fractures with quantitative diffusion mr imaging", *American journal of neuroradiology*, vol. 23, no. 1, pp. 165–170, 2002.

[107] P. Eppenberger, G. Andreisek, and A. Chhabra, "Magnetic resonance neurography: Diffusion tensor imaging and future directions", *Neuroimaging Clinics*, vol. 24, no. 1, pp. 245–256, 2014.

[108] A. Chhabra, A. J. Madhuranthakam, and G. Andreisek, "Magnetic resonance neurography: Current perspectives and literature review", *European radiology*, vol. 28, no. 2, pp. 698–707, 2018.

[109] A. T. Van, B. Cervantes, H. Kooijman, and D. C. Karampinos, "Compensating for eddy current effects in motion-compensated diffusion-prepared tse sequences", in *Proceedings of 25th Scientific Meeting of ISMRM*, 2017, p. 3924.

[110] B. Cervantes, A. T. Van, H. Kooijman, K. van de Ven, A. Hock, E. J. Rummeny, J. S. Kirschke, and D. C. Karampinos, "One-dimensional phase navigation of diffusion-weighted 3d tse for high resolution musculoskeletal diffusion imaging", in *Proceedings of 25th Scientific Meeting of ISMRM*, 2017, p. 1108.

[111] G. C. Sims, E. Boothe, R. Joodi, and A. Chhabra, "3d mr neurography of the lumbosacral plexus: Obtaining optimal images for selective longitudinal nerve depiction", *American Journal of Neuroradiology*, vol. 37, no. 11, pp. 2158–2162, 2016.

[112] E. K. Gibbons, S. S. Vasanawala, J. M. Pauly, and A. B. Kerr, "Body diffusion-weighted imaging using magnetization prepared single-shot fast spin echo and extended parallel imaging signal averaging", *Magnetic resonance in medicine*, 2017.

[113] Q. Zhang, B. Cervantes, D. C. Karampinos, B. F. Coolen, A. J. Nederveen, and G. J. Strijkers, "High resolution 3d diffusion imaging of carotid vessel wall using stimulated echo based diffusion prepared turbo spin echo sequence", in *Proceedings of 24th Scientific Meeting of ISMRM*, 2016, p. 959.

[114] B. Cervantes, Q. Zhang, K. van de Ven, H. Kooijman, E. J. Rummeny, A. Haase, G. J. Strijkers, J. S. Kirschke, A. J. Nederveen, and D. C. Karampinos, "High-resolution dti of distal peripheral nerves using flow-compensated diffusion-prepared 3d tse", in *Proceedings of 24th Scientific Meeting of ISMRM*, 2016, p. 4530.